University Mohamed Boudiaf - M'sila

TECHNOLOGY FACULTY

ELECTRICAL ENGINEERING DEPARTMENT

Serial number ………………….

Registration number …………….

Thesis

Submitted for the award of the

LMD DOCTORATE

Sector: ELECTROMECHANICS

Specialty : ELECTROMECHANICS

THEME

Eddy Current Imaging Using Sensor Arrays for the Detection and Characterization of Random Defects

Presented By

Abderrahmane ABOURA
Soutenue le : / /

Before the jury composed of:

Name & Surname	Grade	Establishment	Quality
Fouad BERRABAH	**Professor**	**Univ. of M'sila**	President
Abdelhak ABDOU	**MCA**	**Univ. of Batna 2**	Supervisor
Tarik BOUCHALA	**Professor**	**Univ. of M'sila**	Co-Supervisor
Salah BELKHIRI	**Professor**	**Univ. of M'sila**	Examiner
Abdelhalim KESSAL	**Professor**	**Univ. of Borj Bou Arréridj**	Examiner
Yahia LAMARI	**MCA**	**Univ. of Batna 2**	Examiner

Academic Year: 2025/2026

الإهداءات

بكل مشاعر الامتنان وأصدق عبارات الوفاء، أهدي هذا الإنجاز المتواضع إلى أسرتي الكريمة، **أسرة عبورة العريقة**، التي أعتز بالانتساب إليها، وكانت السند والركيزة التي اعتمدت عليها في مسيرة حياتي العلمية والعملية.

إلى أسرتي الصغيرة، التي كانت ولا تزال مصدر قوتي وصبري:

إلى والدي العزيز **سليمان** (حفظه الله)، رمز الحكمة والعطاء، لما قدّمه لي من دعم متواصل، ونصح رشيد، وحب غير مشروط، فكان دائمًا النبراس الذي ينير دربي.

وإلى الأرواح الغالية التي غادرت دنيانا، وكان لها أن تفرح بهذا الإنجاز لو كانت بيننا: والدتي الحبيبة **حفيظة لحمر**، وزوجة والدي **فوزية شلوش**. ستبقى ذكراهما حيّة في وجداني، تضيء خطواتي وتوجّه مسيرتي نحو الخير والعزيمة.

كما أهدي هذا العمل إلى إخوتي الأعزاء: **أسامة، لقمان، وعبد الحليم**، وإلى أخواتي الغاليات: **سلمى، نصيبة، وأميمة**، الذين كانت محبتهم ودعواتهم وتشجيعهم مصدر قوة وإصرار لي في كل مرحلة من رحلتي. وأخص بالذكر أختي الكبرى، **المهندسة سمية عبورة**، التي كانت وما زالت قدوة في الاجتهاد والانضباط والإلهام.

ولا يفوتني أن أخص بإهدائي جميع أصدقائي الأوفياء وأحبّتي، دون استثناء، الذين شاركوني أفراحي، وساندوني في أوقات التحديات، وكانوا دافعًا مستمرًا لي لمواصلة درب العلم والنجاح. ولا تزال لحظة نجاحي في مسابقة الدكتوراه حاضرة في ذاكرتي، بما حملته من فرحة صادقة غمرت قلوب أحبّتي، وفي مقدمتهم صديقي العزيز **الدكتور حمزة لورسي**، و**المهندس كرم بيوط**، و**الأستاذ الإمام زهير مرابط**. لذلك، أهديهم جزءًا من هذا الإنجاز، عربون وفاء وتقدير، وأجدد لهم خالص شكري وامتناني على كل ما قدموه لي من دعم وتشجيع ومؤازرة في أصعب المراحل.

وأخيرًا، أهدي ثمرة هذا الجهد إلى **كل أستاذ** أمن بي وساهم بطريقة أو بأخرى في نجاحي، منذ بداياتي التعليمية الأولى وحتى هذا المقام، وكانوا بحقّ الركيزة الأساسية في بلوغي هذه المرحلة من مسيرتي العلمية.

إن هذا الإنجاز ليس لي وحدي، بل هو حصيلة حب ودعاء وجهد ودعم كل من ذُكر، وأتشرف أن أشاركه معهم جميعًا، ليكون عربون وفاء لهم ودليل امتنان مني.

Dedications

With all feelings of gratitude and the sincerest expressions of loyalty, I dedicate this humble achievement to my honorable family. This esteemed Aboura family instilled in me noble values and has always been a constant support and foundation throughout my academic and professional journey.

To my close family, who have been and continue to be the source of my strength and perseverance:

To my dear father, **Slimane** *(may Allah protect him), the symbol of wisdom and generosity, for the continuous support, sound advice, and unconditional love he has given me. He has always been the guiding light that illuminated my path.*

To the precious souls who departed this world, yet would have rejoiced at this achievement had they been among us: my beloved mother, **Hafida Lahmar***, and my stepmother,* **Fouzia Chalouche***. Their memory remains alive in my heart, illuminating my steps and guiding my journey with determination and faith.*

*I also dedicate this work to my dear brothers—***Oussama, Loqman, and Abdelhalim***—and to my beloved sisters—***Selma, Noussiaba, and Oumayma***—whose love, prayers, and encouragement have always been a source of strength and determination at every stage of my journey. A special mention goes to my elder sister,* **Engineer Somia Aboura***, who has always been and continues to be a role model of diligence, discipline, and inspiration.*

I would also like to dedicate this work to all my loyal friends and beloved companions, without exception, who shared in my joys, stood by me in times of challenge, and served as a constant source of motivation to persist on the path of knowledge and success. I still vividly remember the genuine joy that filled their hearts on the day of my success in the doctoral entrance examination—especially my dear friend **Dr. Hamza Lourci***,* **Engineer Karam Biout***, and* **Professor-Imam Zouhair Merabat***. To them, I dedicate a part of this achievement as a token of loyalty and gratitude, and I renew my heartfelt thanks and appreciation for all the support, encouragement, and assistance they extended to me during the most difficult stages of my journey.*

Finally, I dedicate the fruit of this effort to every teacher who believed in me and contributed in one way or another to my success, from my earliest educational beginnings up to this stage, and who were truly the fundamental pillar in enabling me to reach this point in my academic journey.

This achievement is not mine alone—it is the result of the love, prayers, efforts, and support of all those mentioned. I am honored to share it with them all, as a token of loyalty and a testament of my deepest gratitude.

Thanks

First and foremost, I thank ALLAH Almighty for granting me health, strength, and faith to reach this important milestone. I am deeply grateful to my family for their constant support and encouragement, especially my father—may God protect him—for his invaluable guidance and assistance.

I sincerely thank my thesis supervisor, ***Dr. Abdelhak ABDOU****, Professor at Batna 2 University, who calmly guided, corrected, and advised me throughout this project. His rigor was crucial in achieving my thesis objectives.*

I also thank my co-supervisor, ***Dr. Tarik BOUCHAALA****, Professor at M'sila University, whose well-founded and objective critiques enabled me to progress properly in my work.*

I would also like to express my thanks to ***Dr. Fouad Berrabah****, Professor at the University of M'sila, for agreeing to sit on my jury and chair it. I sincerely thank* ***Dr. Salah BELKHIRI ,*** *Professor at the University of M'sila* ***, Dr. Abdelhalim KESSAL****, Professor at the University of Borj Bou Arréridj, and* ***Dr. Yahia LAMARI****, Professor at Batna 2 University, for the honor they bestowed upon me of judging this modest work.*

I would like to sincerely thank ***Dr. Mohamed Chebout*** *and* ***Dr. Bachir ABDELHADI****, respectively Professor at the University of Djelfa and Professor at Batna 2 University, for providing me with useful suggestions and wise advice throughout this work.*

I also wish to express my sincere appreciation to the staff of the Electrical Engineering Department at Mohamed Boudiaf University in M'sila, for their continued commitment to fostering our efforts throughout this research journey, both administratively through its dedicated staff and scientifically through its resources and academic.

Finally, I cannot end these thanks without mentioning all my friends and colleagues from the "Electromechanics" doctoral training, ***Mr Merwane Khebal , Mr Kamel BELKHIRI*** *and* ***Dr Razi MORAKCHI***

Abstracts

Abstracts

الملخص

(NDT) كأداة فعّالة ضمن تقنيات الاختبار غير الإتلافي (ECT) يتناول هذا البحث تطوير تقنية الفحص بالتيارات الدوّامية للكشف عن العيوب وتشخيصها في المواد الموصلة. ورغم مزاياها المتعددة مثل الحساسية العالية، وإمكانية الحمل، والعمل دون تلامس، إلا أن لهذه التقنية قيودًا مرتبطة بعمق الاختراق المحدود، وتعقيد الأشكال الهندسية، والتشويش في القياسات. للتغلب على هذه التحديات، تم تطوير إطار متكامل يجمع بين النمذجة التحليلية، والمحاكاة بالعناصر المحدودة، والتحقق التجريبي، وخوارزميات التعلم الآلي. وقد استُخدمت مصفوفات مجسّات متعددة لتحسين جودة التصوير، كما استُخدمت الشبكات العصبية ذات دالة الأساس الشعاعية (RBF) لتقدير أبعاد العيوب بدقة وكفاءة. أُجريت تجارب تحقق على عينات من الألمنيوم والفولاذ المقاوم للصدأ والتيتانيوم، وأثبتت النتائج دقة النماذج وقابليتها للتطبيق. تساهم هذه الأطروحة في تعزيز دقة وموثوقية تقنية التيارات الدوّامية وتوسيع استخدامها في مراقبة سلامة الهياكل وضمان الجودة الصناعية.

الكلمات المفتاحية *: الاختبار غير المدمر، تيارات،فوكو ، التصوير، شبكات RBF العصبية، أجهزة الاستشعار المتعددة.*

Abstract (English)

This thesis addresses the advancement of Eddy Current Testing (ECT) as a reliable Non-Destructive Testing (NDT) technique for defect detection and characterization in conductive materials. Despite its advantages—such as high sensitivity, portability, and non-contact operation—ECT is limited by shallow penetration depth, geometric complexity, and measurement noise. To overcome these challenges, a comprehensive framework integrating analytical modeling, finite element simulations, experimental validation, and machine learning is developed. Multiplexed sensor arrays are employed to enhance defect imaging, while Radial Basis Function neural networks provide efficient prediction of defect dimensions. The models are validated experimentally on aluminum, stainless steel, and titanium specimens, confirming accuracy and applicability. This work contributes to improving the precision, reliability, and industrial relevance of ECT in structural health monitoring and quality assurance.

Keywords: *Non-Destructive Testing, Eddy Currents, Imaging, Artificial Intelligence, RBF, Multiplexed Sensors.*

Résumé (French)

Ce travail de recherche s'intéresse au développement du contrôle par courants de Foucault (CND-CF) comme méthode performante de contrôle non destructif (CND) pour la détection et la caractérisation des défauts dans les matériaux conducteurs. Malgré ses avantages — sensibilité élevée, rapidité, portabilité et fonctionnement sans contact — le CND-CF reste limité par une faible profondeur de pénétration, la complexité géométrique et le bruit de mesure. Pour dépasser ces contraintes, un cadre méthodologique intégrant la modélisation analytique, la simulation par éléments finis, la validation expérimentale et l'intelligence artificielle a été proposé. Des réseaux de capteurs multiplexés ont été employés pour améliorer l'imagerie des défauts, tandis que les réseaux de neurones à fonction de base radiale (RBF) ont permis l'estimation précise et rapide des dimensions des défauts. Les modèles développés ont été validés expérimentalement sur des échantillons en aluminium, acier inoxydable et titane, démontrant leur fiabilité et leur applicabilité. Cette thèse contribue à renforcer la précision, la fiabilité et la pertinence industrielle de l'ECT dans l'inspection et la surveillance de l'intégrité des structures.

Mots clés: *Non-Destructive Testing, Eddy Currents, Imaging, RBF Neural Networks, Multiplexed sensors.*

Symbols and Abbreviations

Symbols and Abbreviations

Acronyms

- ***NDT***: *Non-Destructive Testing.*
- ***NDE***: *Non-Destructive Evaluation.*
- ***ECT***: *Eddy Current Testing.*
- ***NDT-ECT***: *Non-Destructive Testing by Eddy Currents.*
- ***ECS***: *Eddy Current Sensor.*
- ***MT (MPT)***: *Magnetic Particle Testing.*
- ***RT***: *Radiographic Testing – uses X-rays or gamma rays.*
- ***UT***: *Ultrasonic Testing.*
- ***EMAT***: *Electromagnetic Acoustic Transducer.*
- ***AET***: *Acoustic Emission Testing.*
- ***LT***: *Leak Testing – detects leakage in pressurized systems.*
- ***PT (LPT)***: *Liquid Penetrant Testing.*
- ***VT***: *Visual Testing.*
- ***IRT (TT)***: *Infrared/Thermographic Testing – detects thermal patterns and anomalies.*
- ***SCC***: *Stress Corrosion Cracking.*
- ***EM***: *Electromagnetic Methods.*
- ***MS***: *Magnetic Sensor*
- ***FEM***: *Finite Element Method*
- ***2D***: *Two-Dimensional*
- ***3D***: *Three-Dimensional*

Symbols

- ***A***: *Magnetic Vector Potential (T·m)*
- ***B***: *Magnetic Induction (T)*
- ***D***: *Electric Induction* (C/m^2)
- ***E***: *Electric Field (V/m)*
- ***f***: *Frequency (Hz)*
- ***H***: *Magnetic Field (A/m)*
- ***I***: *Electric Current (A)*
- ***J***: *Current Density* (A/m^2)

- ***Js**: Surface Current Density (A/m^2)*
- ***t**: Time (s)*
- ***U**: Voltage across the sensor (V)*
- ***V**: Electric Scalar Potential (V)*
- ***Φ**: Magnetic Scalar Potential (T·m)*
- ***ω**: Angular Frequency (rad/s)*
- ***σ**: Electrical Conductivity (S/m)*
- ***σp**: Electrical Conductivity of the specimen (S/m)*
- ***ρ**: Electrical Resistivity (Ω·m)*
- ***δ**: Skin Depth (m)*
- ***μ0**: Absolute Magnetic Permeability of Free Space, μ0 = 4π × 10^{-7} H/m*
- ***μr**: Relative Magnetic Permeability*
- ***ε0**: Absolute Electric Permittivity of Free Space, 1/(36π × 10^9) ≈ 8.85 × 10^{-12} F/m*
- ***εr**: Relative Electric Permittivity*
- ***R**: Electrical Resistance (Ω)*
- ***ΔR**: Variation of Resistance (Ω)*
- ***L**: Self-Inductance (H)*
- ***X**: Reactance (Ω)*
- ***Xn**: Normalized Reactance*
- ***ΔX**: Variation of Reactance (Ω)*
- ***Z**: Impedance (Ω)*
- ***ΔZ**: Variation of Impedance (Ω)*
- ***S**: Surface (m^2)*

- **V**: Electric Scalar Potential (V)
- **Φ**: Magnetic Scalar Potential (T·m)
- **ω**: Angular Frequency (rad/s)
- **σ**: Electrical Conductivity (S/m)
- **σp**: Electrical Conductivity of the specimen (S/m)
- **ρ**: Electrical Resistivity (Ω·m)
- **δ**: Skin Depth (m)
- **μ0**: Absolute Magnetic Permeability of Free Space, μ0 = 4π × 10^{-7} H/m

- **μr**: Relative Magnetic Permeability
- **ε0**: Absolute Electric Permittivity of Free Space, $1/(36\pi \times 10^9) \approx 8.85 \times 10^{-12}$ F/m
- **εr**: Relative Electric Permittivity
- **R**: Electrical Resistance (Ω)
- **ΔR**: Variation of Resistance (Ω)
- **L**: Self-Inductance (H)
- **X**: Reactance (Ω)
- **Xn**: Normalized Reactance
- **ΔX**: Variation of Reactance (Ω)
- **Z**: Impedance (Ω)
- **ΔZ**: Variation of Impedance (Ω)
- **S**: Surface (m^2)

Table of Contents

Table of figures

Chapter I

Chapter II

Chapter III

Chapter IV

Table of tables

Chapter I

Chapter III

Chapter IV

General introduction

General introduction

1 Context, topicality and interest of the subject

Non-Destructive Testing (NDT) plays a critical role in ensuring the safety, reliability, and longevity of engineering structures across industries such as aerospace [1], oil and gas [2], power generation[3], transportation[4], and manufacturing[5]. Among the various NDT techniques, Eddy Current Testing (ECT) has established itself as a preferred method for inspecting conductive materials[6]. Its unique combination of advantages—including high sensitivity to surface and near-surface defects[7], rapid inspection speed[8], non-contact operation[9], portability[10], and cost-effectiveness—makes it indispensable for routine maintenance[11], quality assurance, and failure prevention[12].

2 Problem and methodology

Despite its strengths, ECT also faces significant challenges. Its limited penetration depth restricts its ability to detect deeply buried flaws[13], while the complexity of real-world geometries and defect shapes often reduces detection accuracy[14]. Furthermore, external factors such as lift-off variations and material inhomogeneity can introduce noise and ambiguity into measurements[15], [16]. These limitations motivate the development of advanced modeling, simulation, and signal processing strategies to enhance the performance of ECT in both defect detection and characterization.

3 Methodology used

In this research, a comprehensive framework is developed that integrates analytical modeling, finite element simulations, experimental validation, and machine learning approaches to improve the accuracy and reliability of ECT. The theoretical foundation is established through Maxwell's equations and magnetodynamic formulations, followed by finite element modeling using the A–V potential formulation under harmonic excitation. Multiplexed sensor strategies are introduced to overcome the limitations of single-coil configurations, enabling high-resolution defect imaging through sequential activation of array elements.

4 Objective and organization of the thesis

The developed models are validated against experimental measurements on different conductive materials, confirming their accuracy and practical applicability. Building on this validated framework, advanced simulations and multiplexed sensing are applied to reconstruct surface and subsurface defects with high precision. To further enhance defect characterization, Radial Basis Function (RBF) neural networks are employed for predicting defect dimensions, offering a computationally efficient and robust alternative to more complex machine learning techniques.

The contributions of this thesis can be summarized as follows:

1. Mathematical and numerical modeling of ECT using harmonic excitation and multiplexed sensing strategies for defect imaging.

2. *Validation of FEM simulations through comparison with experimental measurements on aluminum, stainless steel, and titanium specimens.*

3. *Development of high-resolution imaging techniques using multiplexed arrays for reconstructing complex defect geometries in plates and tubular structures.*

4. *Integration of intelligent prediction models, particularly RBF neural networks, for real-time estimation of defect dimensions.*

This thesis is structured as follows:

- *Chapter 1 introduces Non-Destructive Testing (NDT) and presents the advantages and limitations of ECT compared with other NDT methods.*
- *Chapter 2 develops the theoretical and numerical framework for ECT, including analytical formulations, finite element modeling, and multiplexed sensing under harmonic excitation.*
- *Chapter 3 validates the proposed models through experimental comparison and applies multiplexed strategies for high-resolution defect imaging.*
- *Chapter 4 extends the framework to the detection and characterization of random defects using machine learning, with a focus on Radial Basis Function neural networks.*
- *Finally, the General Conclusion summarizes the main findings, highlights the contributions, and proposes future research directions.*

Through the integration of theory, simulation, experiment, and intelligent modeling, this thesis contributes to advancing the reliability, precision, and applicability of Eddy Current Testing in industrial inspection and structural health monitoring.

Chaptre I

Inspection of defects and corrosion using non-destructive testing (NDT)

ChapitreI: Inspection of defects and corrosion using non-destructive testing (NDT)

I.1. *Introduction*

In this chapter, a broader perspective is adopted by examining the main categories of non-destructive testing (NDT) methods together with the typical classes of material defects they are designed to detect. NDT encompasses a wide range of inspection methods, including Electromagnetic methods (EM), [17] mechanical wave-based methods,[18] optical and radiative methods, [19] and specific techniques like dye penetrant testing (PT), and eddy current testing (ECT). Each of these categories and techniques offers unique advantages and suffers from certain limitations depending on the type of material and the nature of the defect under investigation.

Material defects themselves can be broadly classified into surface flaws (cracks, scratches, and corrosion), subsurface flaws (voids, delaminations, and inclusions), volumetric flaws (porosity and shrinkage cavities), and variations in material properties such as hardness, conductivity, or microstructure. The ability of each NDT method to detect these categories of defects determines its suitability for specific applications.

Within this landscape, Eddy Current Testing (ECT) emerges as a highly effective technique for conductive materials. Based on electromagnetic induction, ECT enables the detection of surface and near-surface flaws while also providing valuable information on material properties such as conductivity, thickness, and hardness. Compared to other methods, ECT offers significant benefits: high sensitivity to small surface-breaking defects, rapid inspection speed, non-contact operation even through protective coatings, and portability for field use. Furthermore, advanced techniques such as multi-frequency excitation and sensor arrays extend its applicability to certain subsurface flaws.

Although limited in penetration depth and restricted to conductive materials, ECT's advantages make it the method of choice in many safety-critical industries. It is particularly important in aerospace for the detection of fatigue cracks in aluminum structures, in the oil and gas sector for corrosion monitoring of pipelines, and in power generation for the inspection of turbine blades and heat exchanger tubes.

For these reasons, this chapter focuses on the comparative evaluation of NDT methods and defect categories, highlighting the specific strengths of ECT and justifying its selection as the central technique in this research.

I.2. *Categories of material defect inspection methods*

Non-Destructive Testing (NDT) encompasses a wide range of inspection techniques used to evaluate the properties and integrity of materials, components, or systems without causing any damage. These methods play a crucial role in ensuring safety, reliability, and performance across various engineering fields. The chart below (Figure I.1) categorizes the main types of NDT methods based on their physical principles—**electromagnetic**, **mechanical wave-based**, and **optical or radiative** techniques—each suited for detecting specific types of material defects.

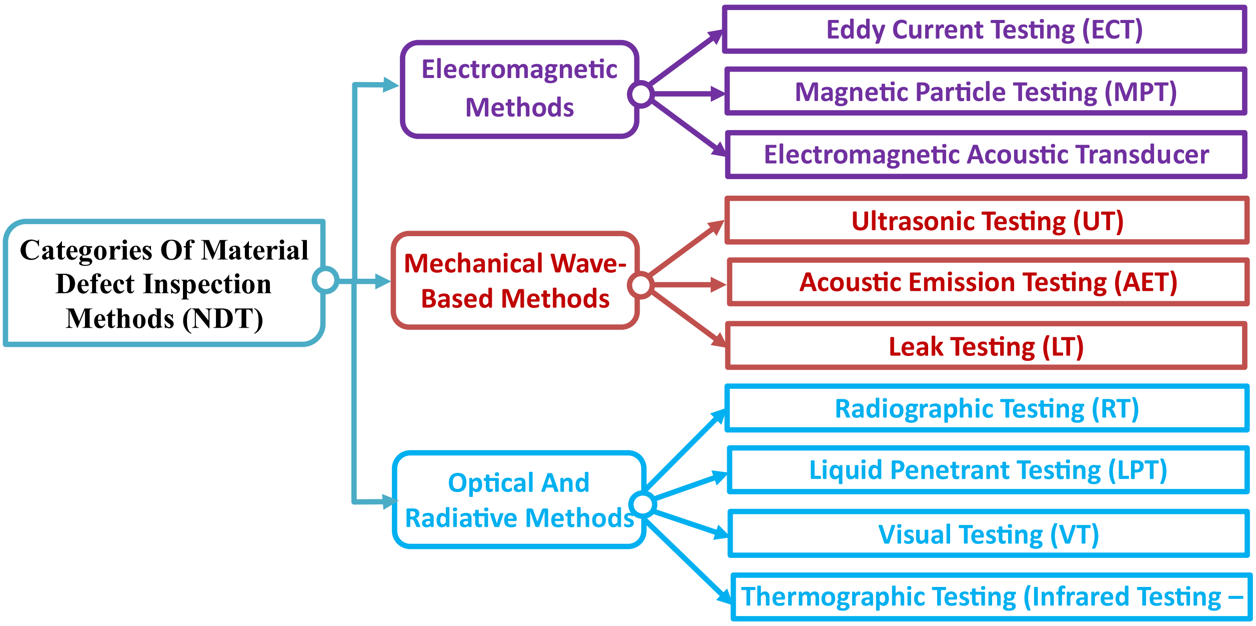

Figure I. 1. Classification of Non-Destructive Testing (NDT) Techniques Based on Physical Inspection Principles

I.2.1. *Electromagnetic methods*

I.2.1.a. Eddy current testing (ECT)

Eddy Current Testing (ECT) is a prominent NDT method that utilizes electromagnetic induction to inspect conductive materials (Figure I.2). A probe generates a time-varying magnetic field by passing an alternating current through a coil, inducing eddy currents in the adjacent material. These currents produce a secondary magnetic field that interacts with the coil, altering its impedance. Defects or material variations disrupt the eddy current flow, causing measurable impedance changes that reveal flaws.

Figure I. 2. Eddy current testing, imaging and a flaw detection device

The inspection process involves placing the probe near the material’s surface, scanning it, and analyzing the impedance changes, often visualized as Lissajous curves or as 2D C-scan images for defect identification.

ECT is widely applied across industries for its sensitivity to surface and near-surface defects. In aerospace, it ensures the integrity of aircraft components by detecting fatigue cracks in aluminum skins and turbine blades. In the oil and gas sector, ECT inspects heat ***exchanger tubes for corrosion and wall thinning, preventing potential failures. In*** manufacturing, it assesses steel plates for inclusions to ensure product quality, while in power generation, it evaluates welds in nuclear reactor components for stress corrosion cracking.

Key advantages of ECT include its ability to detect small defects, its non-contact inspection capability even through coatings, and its rapid scanning speed, particularly when using array probes, making it ideal for automated systems. ECT’s versatility also extends to measuring material properties such as conductivity and thickness, and its portability supports field inspections in remote or difficult environments.

However, ECT is limited to conductive materials, making it unsuitable for non-conductive substances. Its penetration depth is constrained by the skin effect: higher frequencies enhance surface sensitivity, while lower frequencies allow moderate subsurface inspection with reduced resolution. Noise from lift-off variations, temperature fluctuations, or material heterogeneity can affect inspection results, although advanced probe configurations and differential or reflection setups can mitigate these issues.

In an aerospace context, for example, an ECT array probe operating at 500 kHz can scan an aluminum aircraft panel, producing a C-scan image that reveals a 2 mm-long crack near a rivet hole. This enables early, targeted repairs without the need for disassembly.

I.2.1.b. Magnetic particle testing (MPT)

Magnetic Particle Testing (MPT) in Figure I.3, also known as Magnetic Particle Inspection (MPI), [20] is an NDT method that uses magnetic fields to detect surface and near-surface defects in ferromagnetic materials, such as iron, steel, or nickel alloys. The material is magnetized using a magnetic field created by a yoke, coil, or direct current, which generates magnetic flux lines within the material. Defects, such as cracks or voids, disrupt the flux, causing magnetic leakage fields at the defect sites. Magnetic particles, either dry powder or a wet suspension, are applied to the surface, and these particles are attracted to the leakage fields, forming visible indications of the defects. The process involves magnetizing the component using a yoke, coil, or current (AC for surface defects, DC for near-surface defects), applying magnetic particles, and visually inspecting the indications under UV light (for fluorescent particles) or visible light. The indications are then analyzed to identify the defect's location, size, and type.

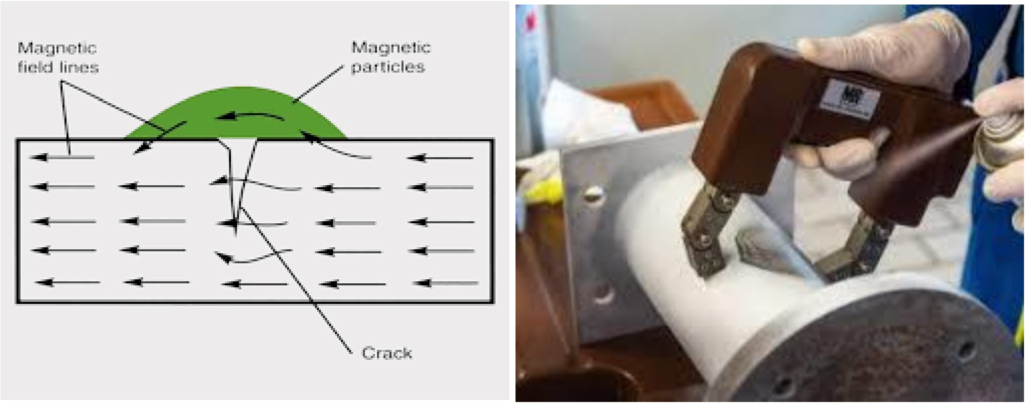

Figure I. 3. Illustration for Magnetic Particle Testing (MPT)

MPT is widely used for surface and near-surface defect detection in ferromagnetic materials across various industries. In aerospace, it inspects steel landing gear components for fatigue cracks, ensuring the safety of aircraft during take-off and landing. In the automotive industry, MPT checks engine components for surface cracks, preventing failures in critical systems. In manufacturing, it evaluates welds in steel structures for surface-breaking defects, ensuring weld quality. In power generation, MPT inspects turbine shafts for stress corrosion cracking, maintaining the reliability of power plants. The advantages of MPT include its high sensitivity to surface and near-surface defects (cracks as small as 0.1 mm deep), its simplicity and speed, making it suitable for high-volume production environments, and its cost-effectiveness, as it requires relatively low-cost equipment and materials compared to RT or UT. The defects are directly visible, requiring minimal interpretation, and the equipment, such as yokes, is portable, ideal for field inspections.

However, MPT has limitations, [21]. It is only applicable to ferromagnetic materials, making it ineffective on non-magnetic materials like aluminum, titanium, or stainless steel. It requires a clean surface free of grease, paint, or coatings, which may need to be removed, adding to preparation time. MPT is limited to surface and near-surface defects (up to 3 mm deep with DC), and it cannot detect deep internal defects. Complex geometries may require multiple magnetization directions to ensure full coverage, increasing inspection time. Additionally, MPT requires trained operators to magnetize correctly and interpret indications, [22] avoiding false positives due to surface irregularities. For example, in a manufacturing application, MPT using a yoke and fluorescent particles might be used to inspect a steel weld for surface cracks. After magnetizing the weld and applying particles, a 5 mm-long crack indication is visible under UV light, indicating a surface-breaking defect that requires repair to ensure the weld's integrity.

I.2.1.c. *Electromagnetic acoustic transducer (EMAT)*

Electromagnetic Acoustic Transducer (EMAT) testing, like illustrated in Figure I.4 it is an NDT method that uses electromagnetic fields to generate ultrasonic waves directly in a conductive material, eliminating the need for a couplant, unlike traditional Ultrasonic Testing (UT). An EMAT probe, [23] consisting of a coil and a magnet (permanent or electromagnet), induces eddy currents in the material. The magnetic field interacts with these currents to produce ultrasonic waves via the Lorentz force or magnetostriction, depending on the material. These waves travel through the material, reflecting off defects, and are detected by the same or a separate EMAT. The process involves placing the EMAT probe near the material surface, generating ultrasonic waves, and analysing the reflected waves to identify defects or measure material properties like thickness, similar to UT but without the need for a couplant.

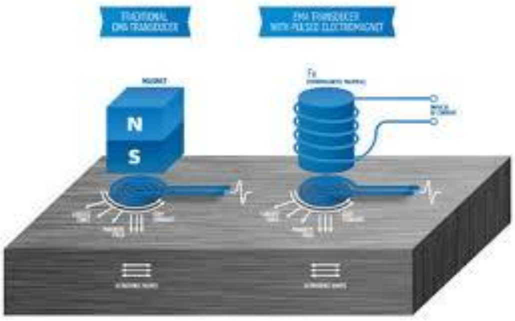

Figure I. 4. Illustration for Electromagnetic Acoustic Transducer (EMAT)

EMAT is particularly useful for inspecting conductive materials in harsh environments, [24] where traditional UT may be impractical. In the oil and gas industry, it measures pipe wall thickness at high temperatures (600°C) without contact, allowing for in-service inspections without shutting down operations. In manufacturing, EMAT inspects steel plates for internal defects during production, ensuring quality in real-time. In power generation, it evaluates boiler tubes for corrosion or cracking, maintaining the reliability of power plants. In aerospace, EMAT checks titanium components for subsurface defects, ensuring the safety of aircraft structures. The advantages of EMAT include its non-contact nature, [25] requiring no couplant, making it ideal for high-temperature, rough, or coated surfaces. It can operate in harsh environments, such as extreme temperatures (-40°C to 600°C) or corrosive conditions, and is versatile, generating various wave modes (shear, longitudinal) for different defect types. EMAT requires minimal surface preparation and is safe, involving no radiation or hazardous materials.

However, EMAT has limitations. It is only applicable to conductive or ferromagnetic materials, making it ineffective for non-conductive materials like plastics or ceramics. It has lower sensitivity than conventional UT for small defects due to lower signal strength, which can affect defect detection accuracy. EMAT systems are more complex and expensive than standard UT systems, increasing costs. The method is sensitive to lift-off, [23] where small changes in probe distance can affect signal quality, requiring careful positioning. Additionally, EMAT requires expertise to optimize wave modes and interpret signals, adding to operational complexity. For example, in an oil and gas application, an EMAT probe might be used to measure the wall thickness of a hot steel pipe (500°C) in a refinery. The probe generates shear waves, and the time-of-flight indicates a thickness of 6 mm, revealing 1 mm of corrosion loss, prompting maintenance without the need to cool the pipe, minimizing downtime.

I.2.2. *Mechanical wave-based methods*

I.2.2.a. Ultrasonic testing (UT)

Ultrasonic Testing (UT) is a versatile NDT method that uses high-frequency sound waves (typically 0.5–20 MHz – Figure I.5) to inspect materials for internal defects or to measure material properties,[26]. A transducer, often piezoelectric, generates ultrasonic waves that travel through the material, reflecting off boundaries such as defects, inclusions, or the back wall of the component, [27]. The reflected waves, or echoes, are detected by the same or a separate transducer and analyzed to identify defects or measure properties like thickness. The process begins with setting up the transducer, which is coupled to the material using a couplant (gel, water) to ensure efficient sound wave transmission. The transducer emits ultrasonic pulses, and the echoes are received and displayed on a screen as an A-scan (amplitude vs. time), B-scan (cross-sectional view), or C-scan (2D map).

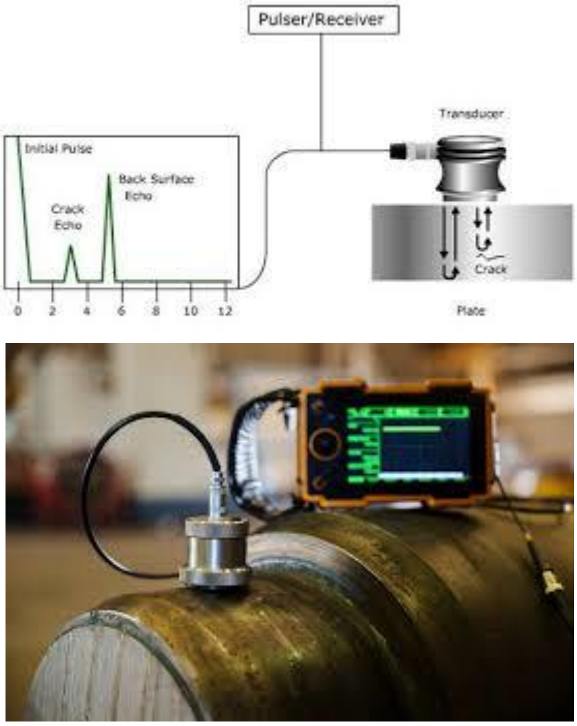

Figure I. 5 The working principle of ultrasonic technology for defect detection

The time-of-flight and amplitude of the echoes indicate the location, size, and type of defects, such as cracks, voids, or inclusions, allowing for precise characterization.

UT is widely applied across industries for its ability to detect internal defects and measure thickness, [28]. In aerospace, it is used to inspect composite materials for delaminations or titanium components for internal voids, ensuring the reliability of aircraft structures. In the oil and gas industry, UT measures pipe wall thickness to detect corrosion or erosion, preventing leaks or failures in pipelines. In manufacturing, it checks welds in steel structures for lack of fusion or porosity, ensuring weld quality. In power generation, UT evaluates turbine blades for internal cracks or inclusions, maintaining the safety of power plants. The advantages of UT include its deep penetration, capable of inspecting thick materials (up to 10 meters in steel at 1 MHz), and its high accuracy, providing precise defect sizing and depth measurement (±0.1 mm accuracy). It is versatile, detecting a wide range of defects and measuring thickness, and it is non-hazardous, posing no radiation risk to operators or the environment. Modern UT equipment is also portable, making it suitable for field inspections.

However, UT has limitations, [29]. It requires a clean, smooth surface and a couplant, which can be impractical in some environments, such as high-temperature or rough surfaces. It is less effective on coarse-grained materials (cast iron) due to the scattering of sound waves, which can obscure defect signals. UT requires highly trained operators to interpret complex signals, especially for advanced techniques like phased array UT. Complex geometries may require angled transducers or immersion testing, increasing complexity, and UT has limited sensitivity to shallow surface defects compared to methods like ECT or dye penetrant testing. For example, in an oil and gas application, a UT probe at 5 MHz might be used to measure the wall thickness of a steel pipeline, [30]. The transducer sends pulses through the pipe wall, and the time-of-flight of the echo from the back wall indicates a thickness of 8 mm, revealing 2 mm of corrosion loss compared to the original 10 mm, prompting maintenance to prevent failure.

I.2.2.b. Acoustic emission testing (AET)

Acoustic Emission Testing (AET) is an NDT method that monitors the transient elastic waves (Figure I.6), known as acoustic emissions, generated by the rapid release of energy from localized sources within a material, such as crack growth, plastic deformation, or corrosion, [31]. These emissions are detected by sensors (piezoelectric transducers) placed on the surface of the component, and the signals are analysed to identify active defects. The process involves attaching sensors to the component and calibrating the system to filter out background noise, such as mechanical vibrations or environmental sounds. The component is then subjected to stress, such as pressure or mechanical load, which induces acoustic emissions from defect growth. The sensors detect these emissions, and the signals are analysed for amplitude, frequency, and location to identify and characterize active defects, often using triangulation to pinpoint defect locations.

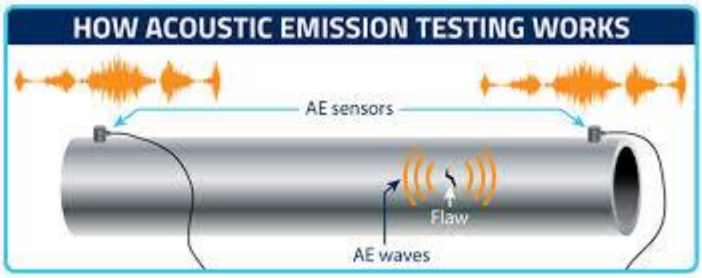

Figure I. 6 *Illustration for Acoustic Emission Testing (AET)*

AET is used for real-time monitoring of active defects under stress, making it ideal for in-service inspections. In aerospace, it monitors composite structures for delamination growth during load testing, ensuring the integrity of aircraft components, [32]. In the oil and gas industry, AET detects crack growth in pressure vessels or pipelines under operating conditions, preventing catastrophic failures. In manufacturing, it monitors welds for crack propagation during cooling, ensuring quality during production. In power generation, AET assesses reactor vessels for active defects during operation, providing early warning of potential failures. The advantages of AET include its ability to provide real-time monitoring, detecting active defects as they grow, and its large area coverage, as a few sensors can monitor large structures, reducing inspection time. It is non-invasive, requiring minimal surface preparation, and provides early warning of defect growth, enabling preventive maintenance. AET is versatile, applicable to a wide range of materials, including metals, composites, and ceramics.

However, AET has limitations, [33]. It only detects active defects under stress, meaning dormant defects may go undetected, requiring the component to be stressed during testing. Background noise, such as mechanical vibrations or environmental sounds, can mask signals, requiring careful filtering and calibration. Pinpointing the exact location of defects can be challenging, often requiring triangulation with multiple sensors, which adds complexity. AET requires expertise to interpret complex acoustic signals and distinguish defect signals from noise, [34]It is limited to detecting active defects, unable to identify pre-existing, stable defects that are not growing. For example, in an oil and gas application, [35] AET might be used to monitor a pressure vessel during a hydrostatic test. Sensors detect acoustic emissions from a growing crack in a weld, allowing the operator to stop the test and repair the defect before it leads to catastrophic failure, ensuring the vessel’s safety.

I.2.2.c. Leak testing (LT)

Leak Testing (LT) is used to detect and locate leaks in systems or components designed to hold pressure or contain fluids/gases (Figure I.7), ensuring their integrity and preventing failures, [36]. Various methods are used, including bubble testing, pressure change testing, and tracer gas testing (helium leak detection), depending on the component and required sensitivity. In bubble testing, a pressure differential is created, and a soap solution is applied to the surface, with bubbles forming at leak sites. In pressure change testing, the component is pressurized or evacuated, and pressure changes are monitored over time to detect leaks. In tracer gas testing, a tracer gas like helium is introduced, and a mass spectrometer detects leaks by identifying the tracer gas escaping through defects. The process varies by method but generally involves creating a pressure differential, applying a detection method, and analyzing the results to identify leak locations and rates.

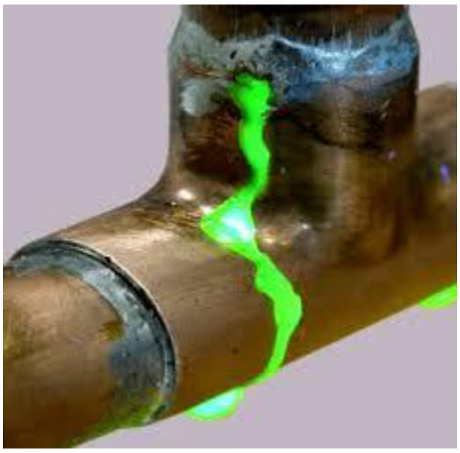

Figure I. 7.Illustration for Leak Testing (LT)

LT is widely used to ensure the integrity of sealed systems across industries. In aerospace, it checks fuel tanks for leaks in aircraft, ensuring safety during flight. In the oil and gas industry, LT tests pipelines or valves for gas leaks, preventing environmental hazards or explosions. In manufacturing, it inspects pressure vessels or heat exchangers for leaks, ensuring quality in production. In power generation, LT ensures reactor coolant systems are leak-free, maintaining the safety of nuclear facilities. The advantages of LT include its high sensitivity, with tracer gas methods like helium leak testing detecting leaks as small as 10^{-12} Pa·m³/s, and its versatility, [37]. As various methods can be tailored to the component and leak size. It ensures safety by verifying systems are leak-free, provides quantitative results (leak rates), and is non-destructive, preserving the component during testing.

However, LT has limitations. Some methods, like bubble testing, require direct access to the surface, which may be impractical for large or complex systems. Tracer gas testing can be time-consuming, especially for large components, slowing down inspections. Advanced methods like helium leak testing require expensive equipment, such as mass spectrometers, increasing costs. Environmental conditions, such as temperature, pressure, or humidity, can affect results, requiring controlled conditions, and LT requires expertise to select the appropriate method and interpret results accurately. For example, in a power generation application, helium leak testing might be used to inspect a nuclear reactor coolant pipe. Helium is introduced into the pipe, and a mass spectrometer detects a leak rate of 10^{-8} Pa·m³/s at a weld joint, indicating a small leak that requires repair to prevent coolant loss and ensure the reactor's safety.

I.2.3. *Optical and radiative methods*

I.2.3.a. Radiographic testing (RT)

Radiographic Testing (RT) based on penetrating radiation, such as X-rays or gamma rays (Figure I.8), to inspect materials for internal defects, [38]. The radiation passes through the material and is attenuated based on the material's density and thickness. A detector, such as a radiographic film or digital panel, captures the radiation on the opposite side, producing an image where defects appear as variations in intensity due to differences in attenuation. The process involves setting up a radiation source, such as an X-ray tube or a radioactive isotope like Ir-192, on one side of the component, with a detector positioned on the opposite side. Radiation passes through the material, and the detector captures the resulting image, which is then analysed for defects. Voids or inclusions, for example, appear as darker spots due to less attenuation, while denser areas appear lighter.

RT is ideal for detecting internal defects in a wide range of materials and is widely applied in various industries, [39]. In aerospace, RT inspects welds in aircraft structures for porosity or lack of fusion, ensuring the integrity of critical components. In the oil and gas industry, it evaluates pipeline welds for internal cracks or inclusions, preventing leaks or failures. In manufacturing, RT checks castings for shrinkage voids or inclusions, ensuring quality in production, [40]. In power generation, it inspects pressure vessels for weld imperfections, maintaining safety in high-pressure systems. The advantages of RT include its excellent ability to detect internal defects in thick components, its production of a permanent radiographic image (film or digital) for documentation, and its versatility, as it can be applied to a wide range of materials, including metals, composites, and ceramics. Digital radiography, in particular, offers high resolution, detecting defects as small as 0.1 mm with clarity.

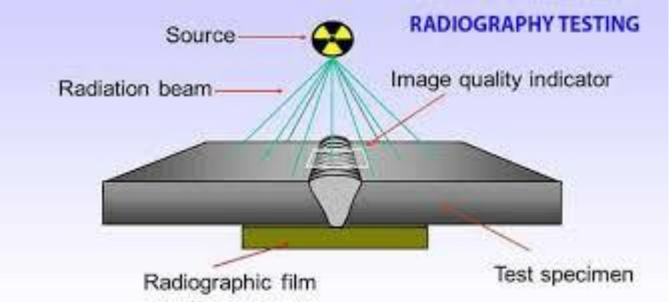

Figure I. 8 Illustration for radiography testing

However, RT has significant limitations. It poses a radiation hazard, requiring strict safety measures to protect operators, such as shielding and restricted access zones. The equipment, such as X-ray machines, and safety protocols are expensive and complex, increasing the cost of inspection. RT requires access to both sides of the component (for the source and detector), which may be impractical for large structures like bridges or pipelines. It has limited sensitivity to certain defects, such as planar defects (cracks) oriented parallel to the radiation beam, which may not be detected. Additionally, RT requires trained radiographers to interpret images and ensure safety compliance, adding to the operational complexity. For example, in an oil and gas application, [41] RT using an Ir-192 gamma source might be used to inspect a pipeline weld. The radiograph reveals a 3 mm-long inclusion in the weld, indicating a potential weak point, leading to weld repair to ensure pipeline integrity and prevent failure.

I.2.3.b. Liquid penetrant testing (LPT)

Liquid Penetrant Testing (LPT), also known as Dye Penetrant Testing (DPT), uses a liquid penetrant to detect surface-breaking defects in non-porous materials (Figure I.9), such as metals, plastics, or ceramics. The penetrant is applied to the surface, where it seeps into surface-breaking defects, such as cracks or porosity, via capillary action. After a dwell time, excess penetrant is removed, and a developer is applied to draw the penetrant out of the defects, creating a visible indication, [42]. The process begins with cleaning the surface to remove contaminants like grease or dirt, ensuring the penetrant can enter defects. The penetrant is applied (by spraying) and allowed to dwell for 5–30 minutes. Excess penetrant is then removed, and a developer (dry powder, wet suspension) is applied. The indications are visually inspected under white light (for visible dye) or UV light (for fluorescent dye) to identify defects.

LPT is widely used for detecting surface-breaking defects in a variety of materials across industries. In aerospace, it inspects aluminum aircraft components for surface cracks, ensuring the safety of critical structures, [43]. In the automotive industry, LPT checks engine blocks for casting defects, preventing failures in engine components. In manufacturing, it evaluates welds for surface-breaking porosity or cracks, ensuring weld quality. In power generation, LPT inspects stainless steel pipes for stress corrosion cracking, maintaining the integrity of piping systems. The advantages of LPT include its high sensitivity to small surface-breaking defects (cracks as small as 0.01 mm), its versatility, as it can be applied to a wide range of non-porous materials, and its simplicity and cost-effectiveness, requiring minimal equipment (penetrant, developer, UV light). The defects are directly visible, requiring minimal interpretation, and LPT works on both magnetic and non-magnetic materials, making it highly versatile.

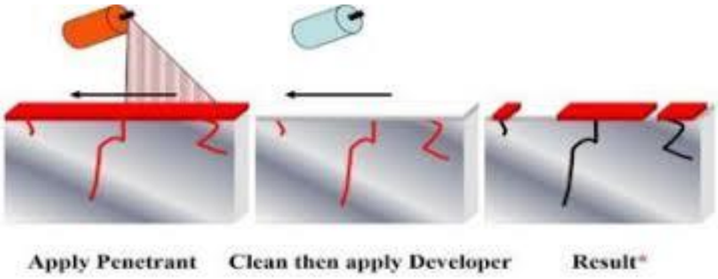

Figure I. 9 Illustration for Liquid Penetrant Testing (LPT)

However, LPT has limitations. It is limited to surface-breaking defects and cannot detect subsurface or internal defects. It requires a clean, smooth surface, which may involve removing coatings or contaminants, adding to the preparation time, [44]. LPT is not effective on porous materials (castings with open porosity), as the penetrant may seep into the material, obscuring defect indications. The process can be time-consuming due to the dwell time (5–30 minutes) and cleaning requirements, slowing down inspections. Additionally, some penetrants and developers contain chemicals that require proper disposal, raising environmental concerns. For example, in an aerospace application, LPT using fluorescent penetrant might be used to inspect a titanium turbine blade for surface cracks. After applying the penetrant, removing excess, and applying a developer, a

$2mm - long$ crack indication is visible under UV light near the blade root, prompting further evaluation or repair to prevent failure during operation.

I.2.3.c. *Visual testing (VT)*

Visual Testing (VT) is the simplest and most fundamental NDT method (Figure I.10), involving direct or indirect visual inspection of a component's surface to identify defects or irregularities, [45]. It can be performed with the naked eye or with tools such as magnifying glasses, borescopes, or cameras, depending on the accessibility and size of the defects. The process begins with ensuring proper lighting (bright white light, UV light) and access to the inspection area, such as cleaning the surface or using mirrors for hard-to-reach areas. The inspector then visually examines the surface for defects, such as cracks, corrosion, or weld imperfections, using tools as needed to enhance visibility. The findings are documented, often with photographs or videos, for further evaluation or reporting.

VT is often the first step in NDT and is applied across industries for surface inspection. In aerospace, it inspects aircraft skins for corrosion or dents, identifying visible damage that may require further investigation. In the oil and gas industry, VT checks pipelines for external corrosion or mechanical damage, ensuring the integrity of transport systems. In manufacturing, it evaluates welds for surface imperfections like undercut or spatter, ensuring weld quality. In power generation, VT inspects turbine blades for erosion or foreign object damage, maintaining the reliability of power plants. The advantages of VT include its simplicity, requiring minimal equipment (a flashlight, magnifying glass), making it accessible and cost-effective. It provides immediate results, as defects are visible in real-time, allowing for quick decision-making. VT is versatile, applicable to all materials and components, regardless of composition or geometry, and it is non-invasive, requiring no preparation or contact. It is often used as a preliminary inspection to identify areas for more detailed NDT methods.

Figure I. 10. Instrumentation for Visual Testing (VT)

However, VT has significant limitations, [45]. It is limited to surface-only detection and cannot identify subsurface or internal defects. It relies heavily on the inspector's skill, experience, and visual acuity, which may lead to missed defects, especially if they are small or subtle. VT requires a direct line-of-sight, and inaccessible areas (inside pipes) need tools like borescopes, which may not always be available. Poor lighting or surface conditions, such as dirt or paint, can obscure defects, reducing effectiveness. Additionally, VT has limited sensitivity to very small defects (micro-cracks) without magnification or enhanced techniques. For example, in a power generation application, VT using a borescope might be used to inspect the inside of a steam turbine for erosion. The inspector identifies visible pitting on the blade surface, indicating early-stage erosion, and recommends further UT inspection to assess the depth of material loss and determine if repairs are needed.

I.2.3.d. *Thermographic testing (infrared testing – IRT)*

Thermographic Testing (IRT) as presented in Figure I.11, also known as infrared testing, is an NDT method that uses infrared cameras to detect temperature variations on a material's surface, [46] which can indicate defects or material anomalies. Heat is applied to the material, often using flash lamps, hot air, or induction, and defects such as voids, delamination, or corrosion cause variations in heat flow, resulting in temperature differences. These differences are captured by an infrared camera as thermal images, where defects appear as hot or cold spots. The process involves positioning an infrared camera and heat source (a flash lamp) to monitor the component. Heat is applied, and the camera captures thermal images as the material cools or heats. The thermal images are then analysed for temperature anomalies, identifying defects based on their thermal signature.

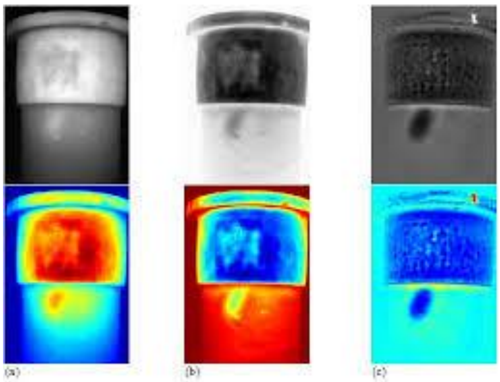

Figure I. 11 .Illustration for Thermographic Testing (Infrared Testing – IRT)

IRT is particularly useful for detecting defects that affect heat flow, often in composites or coatings, and is applied across various industries. In aerospace, it inspects composite aircraft panels for delamination or water ingress, ensuring the structural integrity of lightweight materials. In the oil and gas industry, IRT detects corrosion under insulation (CUI) in pipelines, identifying hidden degradation without removing insulation. In manufacturing, it evaluates adhesive bonds for voids or disbands, ensuring the quality of bonded components, [47]. In power generation, IRT monitors electrical components for hot spots, indicating potential failures, and preventing electrical faults. The advantages of IRT include its non-contact nature, requiring no physical contact with the component, making it ideal for delicate or hot surfaces. It offers large area coverage, allowing rapid screening of large components, and is versatile, applicable to a wide range of materials, including metals, composites, and plastics. IRT provides real-time imaging, enabling quick defect identification, and is safe, involving no radiation or hazardous materials.

However, IRT has limitations, [48]. It is primarily surface-oriented, detecting defects that affect surface heat flow, and deep internal defects may be missed, especially in thick materials. It requires controlled heat input, which can be challenging for large or complex components, and is sensitive to environmental conditions, such as ambient temperature, emissivity variations, or reflective surfaces, which can affect accuracy. IRT has limited depth penetration, typically effective for defects within 1–5 mm of the surface, depending on the material, and requires expertise to interpret thermal images and account for material properties like emissivity. For example, in an aerospace application, IRT using a flash lamp might be used to inspect a carbon fiber composite aircraft panel. The thermal image reveals a cold spot indicating a 10 mm-diameter delamination, prompting repair to prevent structural failure during flight, ensuring the aircraft's safety.

I.3. *Comparison table of material defect inspection categories*

Table I.1 provides a structured comparison of material defect inspection categories, highlighting three major groups: electromagnetic methods,

Category	**Included Methods**	**Working Principle**	**Common Applications**	**Advantages**	**Limitations**
1. Electromagnetic Methods	ECT, MPT, EMAT	Use of magnetic or electrical fields to detect surface/subsurface flaws	Metals, welds, coatings, tubes	Fast, contactless (EMAT), good for conductive materials	Limited to conductive materials, surface prep needed (MPT)
2. Mechanical Wave-Based Methods	UT, AET, LT	Use of sound or pressure waves to detect defects or leakage	Pipes, tanks, structures, pressure systems	Deep penetration (UT), detects crack growth (AET), sensitive to small leaks	Needs coupling medium (UT), signal interpretation can be complex
3. Optical/Radiative Methods	RT, IRT, VT, LPT	Use of light, radiation, or dye to visualize surface or internal discontinuities	Aerospace, castings, welds, surface inspections	Visual results (RT, VT), broad surface coverage (IRT, LPT)	Health risks (RT), limited depth (VT, LPT), requires clean surfaces

Table I. 1. Comparison of Inspection categories

Mechanical wave–based methods, and optical/radiative methods. Electromagnetic techniques such as Eddy Current Testing (ECT), Magnetic Particle Testing (MPT), and Electromagnetic Acoustic Transducers (EMAT) rely on magnetic or electrical fields to identify surface and subsurface flaws, offering fast and often contactless inspection but remaining limited to conductive materials. Mechanical wave–based methods, including Ultrasonic Testing (UT), Acoustic Emission Testing (AET), and Leak Testing (LT), operate on the propagation of sound or pressure waves, enabling deep penetration and detection of crack growth or leakage, though they often require coupling media and involve complex signal interpretation. Optical and radiative methods—such as Radiographic Testing (RT), Infrared Thermography (IRT), Visual Testing (VT), and Liquid Penetrant Testing (LPT)—use light, radiation, or dyes to reveal discontinuities, proving effective for visual assessment and surface coverage but presenting health risks (RT) or surface preparation constraints. This classification highlights the complementary nature of inspection techniques, where the choice depends on material properties, defect type, and the specific industrial application.

I.4. *Types of defects and corrosion detected by NDT*

Non-Destructive Testing (NDT) techniques are widely applied to detect and characterize different types of material defects and corrosion without impairing the component's functionality. These defects can occur on the **surface** or within the **subsurface** of materials, while **corrosion** represents a major degradation mechanism affecting the structural integrity over time. The following chart Figure I.12 categorizes the main types of defects and corrosion that can be identified using various NDT methods.

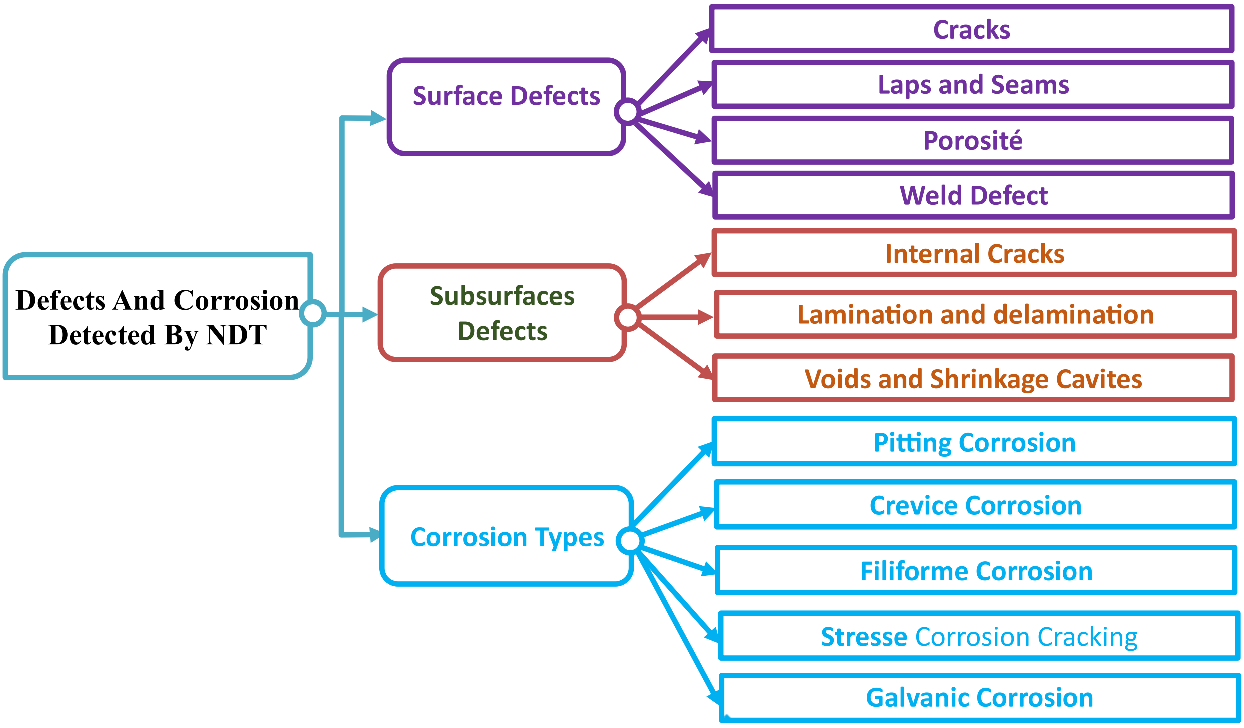

Figure I. 12 Common Types of Defects and Corrosion Detectable by Non-Destructive Testing (NDT)

I.4.1. *Surface defects*

I.4.1.a. Cracks

Cracks are fractures or splits in a material (figure I.13) that can start small and grow over time, potentially leading to catastrophic failure if undetected, [49]. They are classified into several types: fatigue cracks, caused by repeated loading and unloading cycles (pressurization in aircraft); stress corrosion cracks, resulting from a combination of tensile stress and a corrosive environment (chlorides attacking stainless steel); and thermal cracks, formed due to rapid temperature changes creating thermal stress (steel exposed to extreme weather).

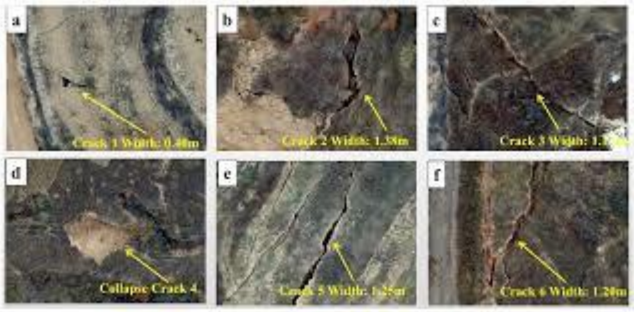

Figure I. 13. Display six levels (a to f) of surface Cracks

These defects are commonly found in aircraft fuselages, turbine blades in power plants, and bridge structures. In aerospace, fatigue cracks from cyclic loading are a major concern, while stress corrosion cracks threaten turbine longevity in power generation. For detection, Magnetic Particle Testing (MT) is ideal for ferromagnetic materials like steel; it involves applying a magnetic field and sprinkling iron particles, which cluster around cracks as they disrupt the field—perfect for surface cracks in steel turbine blades. Eddy Current Testing (ECT) suits conductive materials like aluminum; an alternating current induces eddy currents, and cracks alter these currents, detected as impedance changes, making it excellent for inspecting aircraft aluminum skins.

I.4.1.b. Laps and seams

Laps and seams are surface discontinuities formed during manufacturing when metal folds over itself without bonding (look at Figure I.14), typically in rolling or forging processes. They occur due to improper rolling techniques or forging errors, creating weak points in the material, [50]. These defects are prevalent in pipelines, where they can reduce pressure resistance, pressure vessels, and structural components like beams.

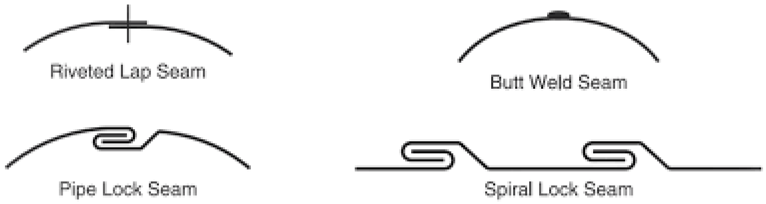

Figure I. 14. Illustration of Laps and Seams defects

In oil and gas, laps in pipeline steel can lead to leaks, while seams in forgings weaken pressure vessels. Ultrasonic Testing (UT) detects these by sending high-frequency sound waves that reflect off the discontinuity, indicating its presence just below or at the surface—effective even for near-surface laps. Visual Testing (VT) uses direct observation with the naked eye, magnifying tools, or borescopes to spot these defects on accessible surfaces, making it a simple yet effective method for initial inspections.

I.4.1.c. *Porosity*

Porosity refers to small voids or gas pockets trapped within a material during solidification, weakening its structure and reducing mechanical, [51], [52].

Strength. It's caused by gas entrapment in castings (during molten metal cooling) or improper shielding gas in welding, [53] leading to bubbles that solidify into voids. Examples include porosity in aluminum castings like engine blocks or welded joints in pipelines. In automotive manufacturing, porosity in engine components can compromise durability, while in construction, it weakens welds. Radiographic Testing (RT) detects porosity using X-rays or gamma rays; voids appear as darker spots on the image due to lower material density, providing a clear visual of their distribution. Ultrasonic Testing (UT) sends sound waves that reflect off these gas pockets, creating distinct echoes on the display, allowing precise location and sizing.

I.4.1.d. *Weld defects: lack of fusion and undercut*

Lack of fusion is a welding defect where the weld metal fails to bond with the base metal or previous weld passes, creating an unjoined interface, [52]. It is caused by insufficient heat, poor welding technique (Figure I.15), or surface contamination. Common in structural steel and pressure vessels, it weakens load-bearing components and risks failure in construction and the oil & gas industries. It can be detected by Ultrasonic Testing (UT), which reflects sound waves off unbonded areas, and Radiographic Testing (RT), where it appears as a clear gap on X-ray images.

Figure I. 15 Shape of the lack of fusion defect

Undercut is a groove melted into the base metal along the weld toe, reducing thickness and strength (Figure I.16). It results from excessive welding current, improper electrode angle, or high speed. Found in shipbuilding and pipelines, it can lead to cracks and structural failure. Detection methods include Visual Testing (VT) for surface grooves and

Dye Penetrant Testing (PT), which uses dye and developer to highlight even small surface flaws.

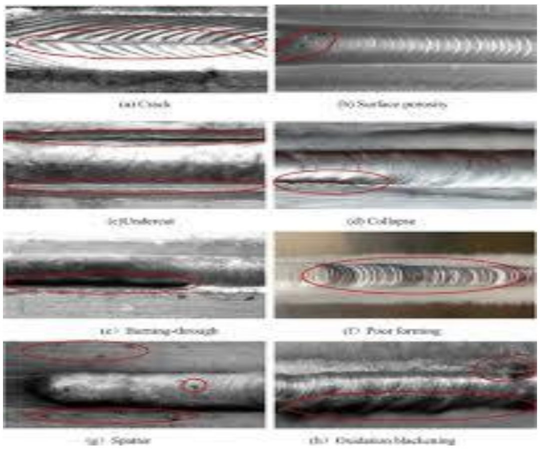

Figure I. 16 Undercut fusion defect

Both defects can significantly compromise weld quality and must be carefully inspected and avoided.

I.4.2. *Subsurface defects*

I.4.2.a. Internal cracks

Internal cracks are fractures within a material, as Figure I.17, hidden from the surface, that can grow under mechanical or thermal stress, [54] posing significant risks. They're caused by fatigue from cyclic loading, thermal stress from temperature gradients, or manufacturing flaws like shrinkage stresses.

Figure I. 17. Defect hidden from the surface

Found in turbine shafts, pressure vessels, and aerospace structures like landing gear, these cracks threaten reliability, [55]. In power generation, internal cracks in turbine shafts can lead to breakdowns, while in aerospace, they risk structural failure. Ultrasonic Testing (UT) detects them by sending sound waves that reflect off the crack surfaces, showing their depth and size on a display. Radiographic Testing (RT) uses X-rays to reveal cracks as lines or shadows within the material, providing a clear internal view.

I.4.2.b. Laminations and delamination

Laminations are layer separations within rolled metal sheets or plates, appearing as flat, parallel discontinuities (Figure I.18). They form when gas pockets or inclusions are flattened during the rolling process, creating unbonded layers. Common in pipeline steel and rolled structural plates, laminations weaken the material's through-thickness strength.

Figure I. 18. Picture of a lamination defect

Delamination is the separation of layers in composite materials or laminates, [56] creating unbonded regions that compromise strength. It's caused by poor bonding during manufacturing, impact damage, or stress exceeding interlayer adhesion. Found in aerospace (carbon fiber aircraft wings) and automotive composites, delamination risks component failure under load.

In oil and gas, they reduce pipeline durability, [57]While in manufacturing, they affect plate quality. Ultrasonic Testing (UT) is the most effective method, using sound waves that detect these separations by changes in reflection patterns; the parallel nature of laminations produces strong, distinct echoes, making UT highly reliable.

I.4.2.c. Voids and shrinkage cavities

Voids as illustrated in Figure I.19 (c), and shrinkage cavities are internal cavities formed during casting (b); voids result from gas entrapment, while shrinkage cavities occur due to material contraction as it cools and solidifies unevenly, [58]. These defects weaken cast components like engine blocks or turbine casings. In automotive manufacturing, voids in engine blocks reduce strength, while in power generation, shrinkage cavities in turbine casings risk failure.

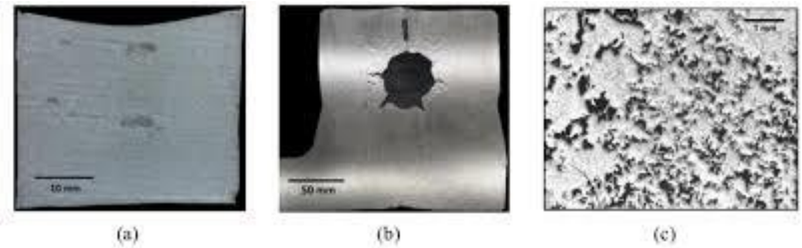

Figure I. 19. Shrinkage cavities and internal cavities formed during casting

Radiographic Testing (RT) detects them as dark spots on X-ray images due to lower material density, offering a visual map of their location. Ultrasonic Testing (UT) identifies them through echoes from the cavity walls, allowing precise sizing and depth measurement.

I.4.3. *Corrosion types*

I.4.3.a. Pitting corrosion

Pitting corrosion (Figure I.20) creates localized, [59] deep pits or holes on a surface, [60] often penetrating significantly despite minimal overall material loss. It occurs when protective oxide layers break down, typically in chloride-rich environments (seawater). Examples include pits in stainless steel pipes or marine equipment. In chemical processing, pitting compromises pipe integrity, while in marine applications, it risks hull breaches.

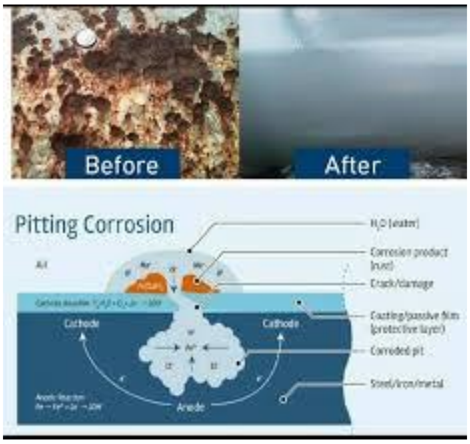

Figure I. 20 .Illustration of pitting corrosion

Eddy Current Testing (ECT) detects pits through changes in electrical conductivity caused by localized material loss. Radiographic Testing (RT) visualizes pits as dark spots on X-ray images, revealing their depth and distribution.

I.4.3.b. Crevice corrosion

Crevice corrosion occurs in narrow gaps or confined spaces where oxygen is limited (Figure I.21), leading to localized material degradation, [61]. It's caused by stagnant solutions in crevices (under bolts or gaskets), creating a differential aeration cell. Common in bolted connections on offshore platforms, it weakens joints in marine and oil and gas applications.

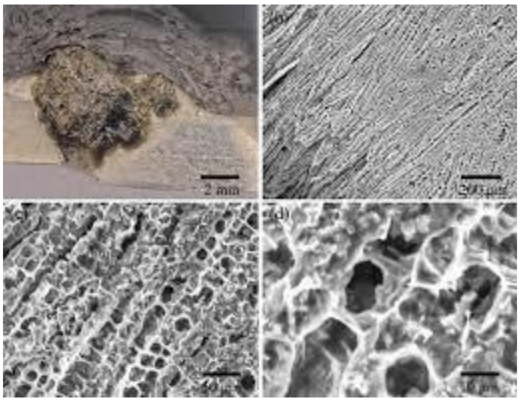

Figure I. 21 .Types of crevice corrosion

Eddy Current Testing (ECT) identifies crevice corrosion through conductivity changes in conductive materials, sensitive to localized loss. Ultrasonic Testing (UT) measures thickness changes in these confined areas, detecting material degradation effectively.

I.4.3.c. *Filiform corrosion*

Filiform corrosion appears as thread-like patterns under coatings, as shown in Figure 22, spreading beneath the surface like filaments. It's caused by moisture and oxygen penetrating coatings, [61] often in humid environments, initiating corrosion at coating defects. Found on painted aircraft surfaces, it affects aesthetics and integrity in the aerospace and automotive industries.

Figure I. 22 Defect under coatings

Eddy Current Testing (ECT) detects subsurface changes in conductivity caused by filiform corrosion. Infrared Thermography (IRT) reveals it through heat signature variations, as corroded areas alter thermal properties under the coating.

I.4.3.d. *Stress corrosion cracking (SCC)*

Stress corrosion cracking (SCC), [62], [63] as illustrated in Figure I.23, involves cracking from the combined action of tensile stress and a corrosive environment, often forming branched crack networks. It's triggered by specific conditions, like chlorides on stainless steel, and is common in nuclear reactor components. In nuclear power, SCC threatens reactor safety, while in chemical plants, it risks vessel integrity.

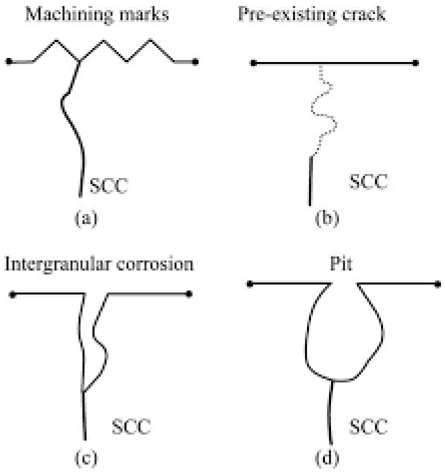

Figure I. 23 Illustration a several defective forms of SCC

Ultrasonic Testing (UT) detects SCC by reflecting sound waves off crack surfaces, revealing their extent. Acoustic Emission Testing (AET) monitors crack growth by listening for acoustic signals emitted under stress, ideal for real-time assessment.

I.4.3.e. Galvanic corrosion

Galvanic corrosion occurs when two dissimilar metals in contact corrode due to an electrochemical potential difference in an electrolyte (seawater), Figure I.24. The more anodic metal corrodes faster, as seen in aluminum-copper electrical connections. In electrical systems, it degrades joints, while in aerospace, it affects mixed-metal assemblies.

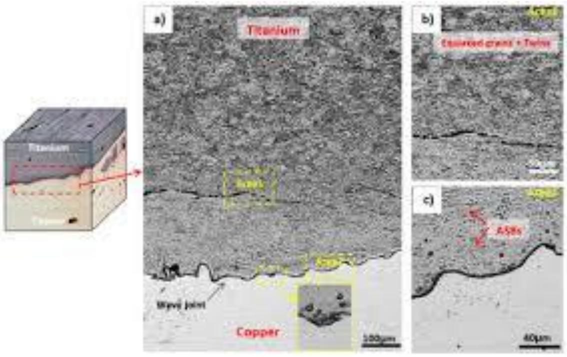

Figure I. 24. Corrosion between materials in contact (touching)

Visual Testing (VT) spots surface material loss and pitting through direct inspection. Eddy Current Testing (ECT) detects conductivity variations in conductive materials, identifying corrosion extent effectively.

I.5. Why use eddy current testing instead of other methods?

Eddy Current Testing (ECT) is a highly effective non-destructive testing (NDT) method that leverages electromagnetic principles to inspect conductive materials for defects and material properties. It is often chosen over other NDT methods like Ultrasonic Testing (UT), Radiographic Testing (RT), Magnetic Particle Testing (MT), and Dye Penetrant Testing (PT) due to its distinct advantages in specific applications. These advantages include its high sensitivity to surface and near-surface defects, rapid inspection speed, ability to work without direct contact, versatility in detecting a wide range of defects, and minimal preparation requirements. Below, we'll explore in detail why ECT is preferred in various scenarios, comparing it to other common NDT methods, and highlighting its practical applications in industries such as aerospace, oil and gas, automotive, and power generation.

a. High Sensitivity to Surface and Near-Surface Defects:

One of the primary reasons ECT is favored is its exceptional sensitivity to surface and near-surface defects in conductive materials, such as metals like aluminum, copper, and stainless steel. ECT works by inducing eddy currents in a conductive material through an alternating magnetic field generated by a coil. When these currents encounter a defect—such as a crack, pit, or inclusion—they are disrupted, causing a change in the coil's impedance, which is then detected and analyzed. This makes ECT particularly effective for detecting small surface cracks (fatigue cracks in aircraft skins) and near-surface flaws (subsurface inclusions in rolled steel).

In contrast, Ultrasonic Testing (UT) is better suited for detecting deeper internal defects, as it uses high-frequency sound waves that can penetrate through the material. However, UT may struggle with very shallow surface defects because the sound waves can reflect off the surface, creating noise that masks small flaws. Radiographic Testing (RT), which uses X-rays or gamma rays to create an image of the material's internal structure, is excellent for visualizing internal voids or inclusions but is less sensitive to small surface defects due to its focus on volumetric imaging. Magnetic Particle Testing (MT) is also highly effective for surface and near-surface defects, but it is limited to ferromagnetic materials (steel), whereas ECT can be used on any conductive material, including non-ferromagnetic ones like aluminum and titanium, making it more versatile for industries like aerospace, where such materials are common.

b. Rapid Inspection Speed:

ECT is renowned for its speed, making it ideal for high-throughput industrial applications. The method allows for real-time inspection, as the probe can be scanned quickly over a surface, and results are displayed immediately on the instrument. For example, in the aerospace industry, ECT is used to inspect aircraft fuselage panels for fatigue cracks during maintenance checks, covering large areas in a short time. The speed of ECT is enhanced by its ability to use automated systems, such as rotating probes for tube inspections in heat exchangers or array probes for large surface areas, which can inspect multiple points simultaneously.

Compare this to Radiographic Testing (RT), which requires setting up X-ray or gamma-ray equipment, exposing the material, and then developing and interpreting the radiographic film—a process that can take hours, especially for large components. Ultrasonic Testing (UT) can also be time-consuming, particularly for complex geometries, as it often requires careful calibration and coupling (using a gel or liquid to ensure sound wave transmission), and the operator must scan the material methodically to ensure complete coverage. Magnetic Particle Testing (MT) involves applying magnetic fields and particles, followed by visual inspection under UV light, which can be faster than RT but still slower than ECT due to the preparation and cleanup involved. ECT's ability to provide rapid results without extensive setup makes it a preferred choice for industries where downtime must be minimized, such as in oil and gas pipeline inspections or power plant maintenance.

c. Non-Contact Inspection Capability:

Another significant advantage of ECT is its ability to perform inspections without direct contact between the probe and the material surface. The eddy currents are induced through an electromagnetic field, meaning the probe can be held at a small distance (a "lift-off" distance) from the surface. This is particularly useful for inspecting materials with coatings, rough surfaces, or high temperatures, where direct contact might be impractical or damaging to the probe. For instance, ECT can detect defects beneath a thin paint layer on an aircraft wing without removing the coating, saving time and preserving the material's protective layer.

In contrast, Ultrasonic Testing (UT) typically requires direct contact or a couplant (water or gel) to transmit sound waves into the material, which can be problematic for rough or coated surfaces unless the coating is removed or a special technique like immersion UT is used. Magnetic Particle Testing (MT) also requires direct surface access, as the magnetic field must be applied directly, and any coatings or contaminants must be removed to ensure the particles can adhere to defects. Dye Penetrant Testing (PT) similarly requires a clean surface for the penetrant to seep into defects, involving multiple steps like cleaning, applying the penetrant, and removing excess penetrant, all of which require direct surface interaction. Radiographic Testing (RT) does not require surface contact, but it involves radiation hazards and the need for access to both sides of the material (for source and film placement), which can be logistically challenging. ECT's non-contact capability simplifies the inspection process and makes it more adaptable to challenging industrial environments.

d. Versatility in Detecting a Wide Range of Defects:

ECT is highly versatile, capable of detecting a variety of defects and material properties in conductive materials. It can identify surface cracks, near-surface inclusions, corrosion (pitting or crevice corrosion), and even material variations like conductivity or thickness changes. For example, in the oil and gas industry, ECT is used to inspect pipelines for pitting corrosion, where localized material loss alters the eddy current flow, detectable as a change in impedance. Additionally, ECT can measure the thickness of non-conductive coatings on conductive substrates (paint on metal), which is useful for quality control in manufacturing.

While Ultrasonic Testing (UT) is also versatile, detecting internal cracks, voids, and laminations, it requires different probes and settings for different defect types and depths, which can complicate the inspection process. Radiographic Testing (RT) excels at visualizing internal defects like voids and inclusions but is less effective for surface defects and cannot measure material properties like conductivity. Magnetic Particle Testing (MT) and Dye Penetrant Testing (PT) are limited to surface and near-surface defects, with MT restricted to ferromagnetic materials and PT requiring a clean surface for the penetrant to work. ECT's ability to handle a broad spectrum of defects and material properties in a single method makes it a go-to choice for applications requiring comprehensive inspections, such as in aerospace for inspecting aluminum aircraft skins or in power generation for checking turbine blades.

e. Minimal Preparation Requirements:

ECT requires minimal surface preparation compared to other NDT methods, which is a significant advantage in industrial settings where time and accessibility are critical. The method can often be applied directly to a component without extensive cleaning or surface treatment, as long as the surface is not heavily contaminated with conductive debris (metal shavings) that could interfere with the electromagnetic field. For example, in the automotive industry, ECT can be used to inspect machined parts for surface irregularities without needing to remove lubricants or minor surface residues.

In contrast, Magnetic Particle Testing (MT) and Dye Penetrant Testing (PT) require thorough surface cleaning to remove dirt, grease, or coatings that could mask defects or interfere with the magnetic particles or penetrant. Ultrasonic Testing (UT) often requires a couplant and a smooth surface to ensure proper sound wave transmission, which may necessitate surface grinding or cleaning for rough components. Radiographic Testing (RT) does not require surface preparation but involves significant setup, including radiation safety measures, shielding, and access to both sides of the component. ECT's minimal preparation requirements reduce inspection time and costs, making it ideal for in-service inspections, such as checking heat exchanger tubes in a petrochemical plant without disassembling the system.

f. Portability and Ease of Use:

ECT equipment is typically lightweight, portable, and easy to use, making it suitable for field inspections in industrial environments. Modern ECT instruments are compact, battery-powered, and often come with digital displays for real-time analysis, allowing inspectors to carry them to remote locations, such as offshore oil platforms or aircraft hangars. The simplicity of the setup—often just a handheld probe connected to a small device—enables quick deployment and operation, even in confined spaces.

Compare this to Radiographic Testing (RT), which requires heavy equipment (X-ray machines or gamma-ray sources), radiation shielding, and safety protocols, making it less practical for field use in some scenarios. Ultrasonic Testing (UT) equipment is portable but requires careful calibration and coupling, which can be cumbersome in field conditions, especially on uneven surfaces. Magnetic Particle Testing (MT) often involves portable yokes or coils, but the need for magnetic particles, UV lights, and surface preparation can complicate field applications. Dye Penetrant Testing (PT) is portable but involves multiple steps (cleaning, applying penetrant, developing, and inspecting), which can be time-consuming in the field. ECT's portability and ease of use make it a preferred method for on-site inspections, such as checking for stress corrosion cracking in nuclear reactor components or inspecting welds in shipbuilding.

g. Safety and Environmental Considerations:

ECT is a safe and environmentally friendly method, as it does not involve radiation, chemicals, or hazardous materials. Unlike Radiographic Testing (RT), which uses X-rays or gamma rays, ECT poses no radiation risk to operators, eliminating the need for shielding, evacuation of personnel, or compliance with strict radiation safety regulations. This makes ECT more practical for use in populated or sensitive areas, such as inspecting components in a functioning power plant or during aircraft maintenance in a hangar.

Dye Penetrant Testing (PT) involves chemicals (penetrants, developers, and cleaners) that can be hazardous to handle and require proper disposal to avoid environmental contamination. Magnetic Particle Testing (MT) often uses magnetic particles suspended in liquids, which can also require careful handling and disposal. Ultrasonic Testing (UT) is generally safe but may require water or gel couplants, which can be messy in some environments. ECT's lack of hazardous materials and safety risks makes it a more sustainable and operator-friendly option in industries where safety and environmental concerns are paramount.

Cost-Effectiveness:

ECT is often more cost-effective than other NDT methods due to its speed, minimal preparation, and lack of consumables. The equipment for ECT, while requiring an initial investment, is relatively inexpensive to operate, as it does not require films (like RT), chemicals (like PT), or magnetic particles (like MT). The rapid inspection speed also reduces labor costs, especially in high-volume applications, such as inspecting miles of pipeline in the oil and gas industry or checking hundreds of turbine blades in a power plant.

Radiographic Testing (RT) can be expensive due to the cost of X-ray or gamma-ray equipment, films, and the need for trained personnel to handle radiation safely. Ultrasonic Testing (UT) equipment can be costly, especially for advanced techniques like Time-of-Flight Diffraction (TOFD), and requires skilled operators for accurate interpretation. Magnetic Particle Testing (MT) and Dye Penetrant Testing (PT) involve recurring costs for consumables (particles, penetrants, developers), as well as labor for preparation and cleanup. ECT's lower operational costs and efficiency make it an economical choice for many industrial applications.

I.5.1. *Practical applications highlighting ECT's advantages*

- **Aerospace**: ECT is widely used to inspect aluminum aircraft skins for fatigue cracks and corrosion, leveraging its sensitivity to surface defects and non-contact capability to avoid damaging protective coatings.
- **Oil and Gas**: ECT is employed to detect pitting corrosion in pipelines, where its speed and ability to inspect through coatings allow for rapid assessment of large areas without downtime.
- **Power Generation**: ECT inspects turbine blades for stress corrosion cracking, using its versatility to detect both surface and near-surface flaws in conductive materials like stainless steel.
- **Automotive**: ECT checks machined parts for surface irregularities, benefiting from its minimal preparation requirements and ability to inspect through lubricants.

I.5.2. *Limitations of ECT and when other methods are preferred*

While ECT has many advantages, it is not always the best choice. Its penetration depth is limited to a few millimeters, depending on the material and frequency used, making it less effective for deep internal defects compared to Ultrasonic Testing (UT) or Radiographic Testing (RT). ECT is also restricted to conductive materials, so it cannot be used on non-conductive materials like plastics or ceramics, where UT or RT might be more appropriate. Additionally, ECT requires calibration for specific materials and defect types, and interpreting the results can be complex, requiring skilled operators, [64].

In scenarios where deep internal defects are a concern, such as voids in a thick casting, RT or UT would be preferred,[29]. For ferromagnetic materials with surface defects, MT might be chosen for its simplicity and effectiveness. For non-conductive materials or very fine surface defects, PT could be a better option. However, in applications where surface and near-surface defects in conductive materials are the primary concern, and speed, safety, and minimal preparation are priorities, ECT stands out as the method of choice.

I.6. *Conclusion*

Eddy Current Testing (ECT) stands out among nondestructive testing methods for its high sensitivity to surface and near-surface defects, rapid inspection speed, non-contact nature, versatility, minimal preparation requirements, portability, safety, and cost-effectiveness. These advantages make it particularly valuable in industries such as aerospace, oil and gas, power generation, and automotive, where conductive materials dominate and reliable inspections are critical. Although ECT has inherent limitations—most notably its restricted penetration depth and applicability to conductive materials—its unique strengths often make it the preferred choice over alternatives like UT, RT, MT, and PT in applications requiring fast, safe, and surface-focused evaluation.

To fully exploit these advantages and address its challenges, a rigorous understanding of the underlying electromagnetic interactions is essential. Therefore, the next chapter develops the mathematical model of ECT, providing the theoretical framework necessary to simulate, interpret, and optimize inspection results.

.

Chaptre II

Theoretical foundations and finite element modeling of eddy current testing

Chapitre II. Theoretical foundations and finite element modeling of eddy current testing

II.1. *Introduction*

This chapter presents a comprehensive exploration of the mathematical modeling of ECT, aiming to bridge theoretical principles with practical applications. It begins by establishing the fundamental principles based on Maxwell's equations,[65] highlighting key relationships among electric fields, magnetic fields, current density, and material properties like conductivity and permeability. These foundations lead to an analytical understanding of eddy current induction and its sensitivity to defects.

However, analytical models, while insightful, often fall short when addressing the complexities of real-world geometries, material inhomogeneities, and defect shapes. To overcome these limitations, the chapter introduces the finite element method (FEM),[66],[67]a numerical approach that discretizes the problem domain and solves Maxwell's equations with high accuracy. The A–V formulation, which employs magnetic vector and electric scalar potentials, is adopted for its effectiveness in modeling harmonic excitations—a mode particularly relevant for surface inspections,[68].

The generation of eddy currents by a single coil under harmonic excitation is explored in detail, providing insights into the formation and behavior of primary and secondary fields. Key magnetodynamic formulations are derived, and essential boundary and continuity conditions are discussed to ensure accurate simulations. Special attention is given to the concept of skin depth, explaining how eddy currents are confined near the material surface,[7]and how this phenomenon dictates frequency selection for targeting specific inspection depths[69].

Beyond the basic interactions, the chapter delves into how defects perturb the eddy current distribution, leading to measurable changes in coil impedance. Analytical expressions are developed to characterize the impedance shifts caused by defects, forming the basis for practical defect detection and sizing strategies. Additional complexities such as the lift-off effect,[70],[71] which introduces variability due to coil positioning, are also mathematically modeled to aid in distinguishing between defect signals and noise.

Recognizing the practical challenges of real-world inspections, the chapter examines the implications of frequency selection for defect detection, emphasizing the trade-off between sensitivity and penetration depth,[72]. The use of impedance plane analysis for interpreting ECT signals is introduced, illustrating how different flaw types manifest distinct trajectories in resistance-reactance plots, aiding in flaw identification.

Furthermore, the modeling of subsurface defects is addressed, highlighting the challenges posed by the exponential attenuation of eddy currents with depth. Advanced techniques, including finite element simulations and perturbation theory, are discussed to illustrate how deep flaws can still be detected and characterized, albeit with reduced sensitivity compared to surface inspections.

In the latter part of the chapter, particular focus is placed on the methods used to drive eddy current array (ECA) systems. Multiplexed excitation, the driving method adopted in this research, is presented as an optimal compromise between imaging resolution, system simplicity, and cost-effectiveness. The chapter compares multiplexed excitation with alternative driving methods such as phased and simultaneous excitation, outlining the advantages and limitations of each approach in various industrial contexts.

Finally, the integration of analytical modeling, finite element simulations, and practical considerations culminates in a robust framework for high-resolution defect imaging. Practical guidelines, such as multi-frequency sweeps, C-scan imaging, and calibration with reference standards, are provided to ensure that the theoretical foundations translate into reliable, actionable inspections.

In sum, this chapter serves not only as a theoretical guide but also as a practical manual for researchers and engineers working in ECT. By combining fundamental electromagnetic theory, advanced numerical modeling, and hands-on inspection strategies, it lays the groundwork for accurate, efficient, and high-resolution defect detection, supporting the critical need for safety and reliability in industrial applications.

II.2. *Mathematical model of eddy current testing*

Eddy Current Testing (ECT) is a non-destructive testing (NDT) method that relies on electromagnetic principles to detect defects and evaluate material properties in conductive materials. The mathematical model of ECT provides a theoretical framework to understand how eddy currents are induced, how they interact with defects, and how these interactions are measured to infer the presence of flaws or material variations. This model is rooted in Maxwell's equations, which govern electromagnetic phenomena, and involves concepts such as magnetic fields, induced currents, impedance changes, and skin depth. Figure II.1 illustrates the conceptual framework of the mathematical modeling of Eddy Current Testing (ECT). It highlights the key theoretical foundations based on Maxwell's equations, the main modeling approaches such as analytical and finite element methods, and the interaction between the eddy current field and material defects. The framework also outlines practical strategies for optimizing ECT performance, including frequency selection, impedance analysis, and array-based inspection methods. Below, the mathematical model of ECT is explored in detail, breaking it down into its fundamental components, deriving key equations, and discussing their implications for practical applications in industrial inspections.

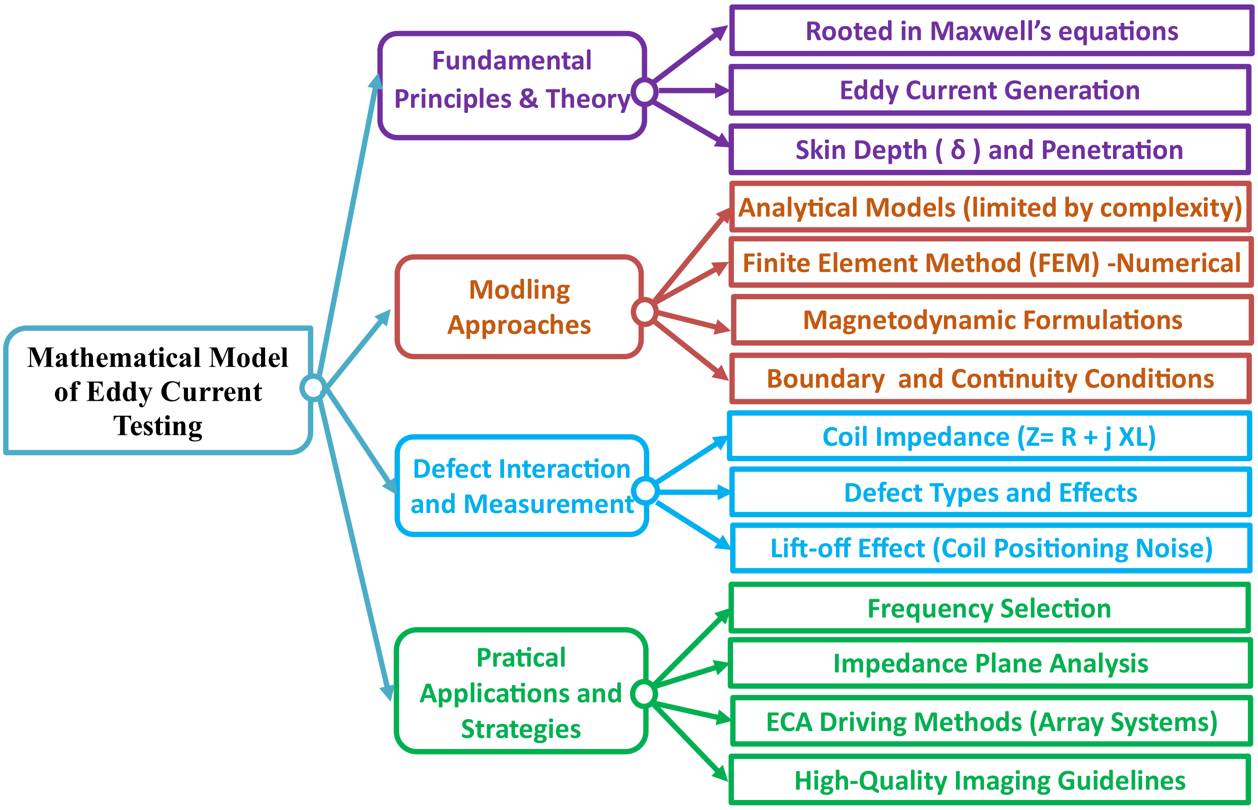

Figure II. 1 Conceptual Framework of the Mathematical Modeling of Eddy Current Testing (ECT)

II.2.1. *Fundamental principles: Maxwell's equations*

The foundation of ECT lies in Maxwell's equations, which describe the behavior of electric and magnetic fields. In the context of ECT, we are primarily concerned with time-varying magnetic fields and their interaction with conductive materials. Maxwell's equations in differential form are:

- Faraday's Law of Induction:

$$\nabla \times E = -\frac{\partial B}{\partial t} \qquad \text{(II.1)}$$

This equation states that a time-varying magnetic field (B) induces an electric field (E), which is the basis for generating eddy currents.

- Ampere-Maxwell Law

$$\nabla \times H = J + \frac{\partial D}{\partial t} \qquad \text{(II.2)}$$

Where:
H is the magnetic field intensity $[A/m]$.

J is the current density $[A/m^2]$.

D is the electric displacement field $[C/m^2]$.

B is the magnetic flux density $[Wb/m^2]$.

E is the electric field intensity $[V/m]$.

For ECT, the displacement current $\frac{\partial D}{\partial t}$ is often negligible at the frequencies used (typically kHz to MHz), so this simplifies to:

$$\nabla \times H = J \qquad \text{(II.3)}$$

- Gauss’s Law for Magnetism:

$$\nabla \cdot B = 0 \qquad \text{(II.4)}$$

- Gauss’s Law for Electricity:

$$\nabla \cdot D = \rho \qquad \text{(II.5)}$$

In ECT, we often assume no free charges $\rho = 0$ in the material.

Additionally, the constitutive relations are:

- $B = \mu H$ where μ is the magnetic permeability of the material $[H/m]$.
- $D = \varepsilon E$ where ε is the permittivity $[F/m]$.
- $J = \sigma E$ where σ is the electrical conductivity $[S/m]$.

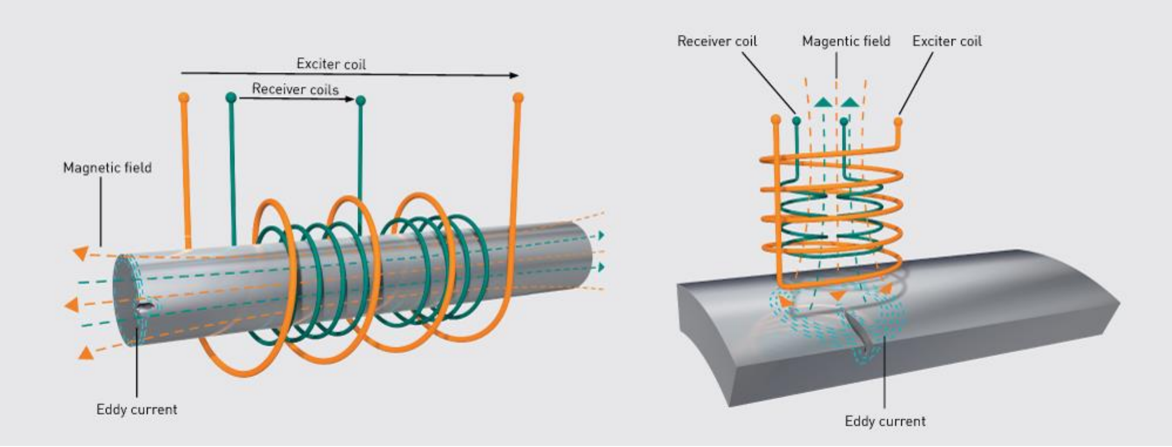

Figure II. 2 Principle of Eddy Current Generation and Detection Using Exciter and Receiver Coils

In ECT, a coil carrying an alternating current (AC) generates a time-varying magnetic field (Figure II.2), which induces eddy currents in the conductive material. These currents, in turn, produce a secondary magnetic field that interacts with the coil, altering its impedance. Defects or material variations disrupt the eddy currents, leading to measurable changes in the coil’s impedance.

II.2.1.a. *Finite element formulation of the magneto-dynamic equation*

The analytical model simplifies ECT but struggles with complex geometries and material variations. The finite element method (FEM) addresses this by solving the magneto dynamic equations numerically, using the $A - V$ formulation to model fields in the coil, conductive material, and air, enhancing the accuracy of defect imaging in harmonic mode inspections.

II.2.1.b. *Vector fields and potentials*

Fields are expressed using potentials

$$H = T - \nabla\phi \qquad \text{(II.6)}$$

$$B = \nabla \times A \qquad \text{(II.7)}$$

$$E = -\frac{\partial A}{\partial t} - \nabla v \qquad \text{(II.8)}$$

$$J = \nabla \times T \qquad \text{(II.9)}$$

Where:

- A: magnetic vector potential
- T : Magnetic vector potential–related function (sometimes referred to as an auxiliary vector function in certain formulations)
- $\emptyset$: magnetic scalar potential
- v : electric scalar potential

Potential-based formulations like $A - V$ are preferred in FEM for better convergence.

II.2.1.c. *Generation of eddy currents by harmonic excitation of a single coil*

In harmonic mode, the coil is excited with a sinusoidal current (Figure II.3)

$$I(t) = I_0 e^{i\omega t} \qquad \text{(II.10)}$$

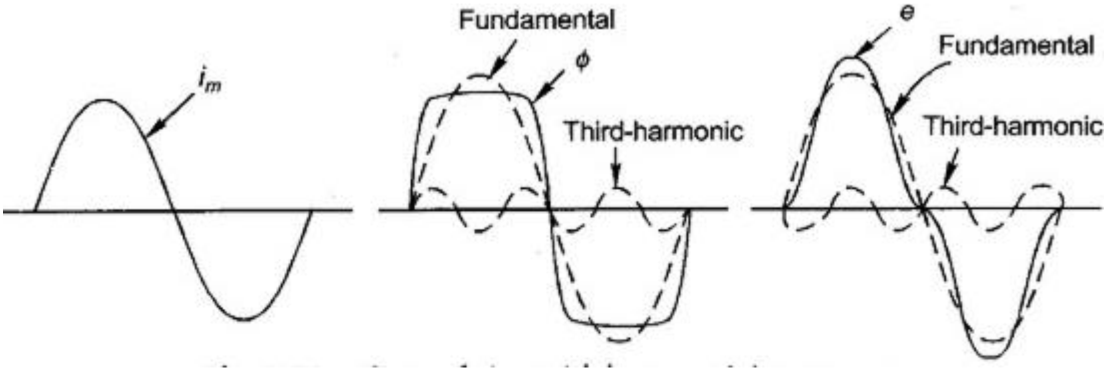

Figure II. 3 Fundamental and Harmonic Components of the Magnetizing Current in Eddy Current Testing

where:

- I_0 is the amplitude $[A]$.
- $\omega = 2\pi f$ is the angular frequency $[rad/s]$
- $j = \sqrt{(-1)}$.

The current in the coil generates a primary magnetic field B_p, which can be approximated as sinusoidal: $B_p = B_0 e^{i\omega t}$

This time-varying magnetic field induces an electric field in the material via Faraday's Law:

$$\nabla \times E = -\frac{\partial B_p}{\partial t} = -j\omega B_p \qquad \text{(II.11)}$$

The induced electric field E, drives eddy currents in the conductive material according to Ohm's law:

$$J = \sigma E \qquad \text{(II.12)}$$

Substituting E from Faraday's Law, the eddy current density J, proportional to the rate of change of the magnetic field and the material's conductivity. These eddy currents flow in closed loops perpendicular to the magnetic field, typically parallel to the surface of the material.

II.3. *Magnetodynamic formulations*

II.3.1. *Electric-Type (A–V in Harmonic Regime):*

$$rot(\frac{1}{\mu} rotA) - grad(\frac{1}{\mu} divA) + j\omega\sigma A + j\omega\sigma \nabla V = J_s \qquad \text{(II.13)}$$

$$div(j\omega\sigma(A + \nabla V)) = 0. \qquad \text{(II.14)}$$

Magnetic-Type $(T - \emptyset)$: Briefly the $T - \emptyset$ formulation uses $J = \nabla \times T$, solving for T (magnetic field)$[A/m]$ and $\emptyset$ is an electric scalar potential $[V]$, but is less common in harmonic mode inspections due to its complexity in handling sinusoidal excitation.

- **Boundary and Continuity Conditions**

For domain Ω with boundary Γ

- **Homogeneous Dirichlet:**

$$A.n = 0 \qquad \text{(II.15)}$$

- **Homogeneous Neumann:**

$$\frac{\partial A}{\partial n} = 0 \qquad \text{(II.16)}$$

At interfaces (Ω_1, Ω_2)

$$(B2 - B1) \cdot n = 0 \qquad \text{(II.17)}$$

$$(H2 - H1).n = J_s \qquad \text{(II.18)}$$

- **Gauge Conditions**

The Coulomb gauge $\nabla \times A = 0$ ensures uniqueness in the $A - V$ formulation, enforced via a penalty term.

- **Finite Element Discretization**

The discretized A–V equations are solved across the conductive material, coil, and air, forming a system solved with the BICGSTAB solver, [73] providing A and (V) for field computations.

II.3.1.a. *Skin depth and penetration of eddy currents*

Eddy currents are not uniformly distributed within the material; their intensity decreases exponentially with depth due to the skin effect. [74]. The skin depth δ is the depth at which the eddy current density drops to $1/e$ (approximately 37%) of its surface value like present in Figure II.4. The skin depth is derived from the diffusion equation for the magnetic field in a conductive medium.

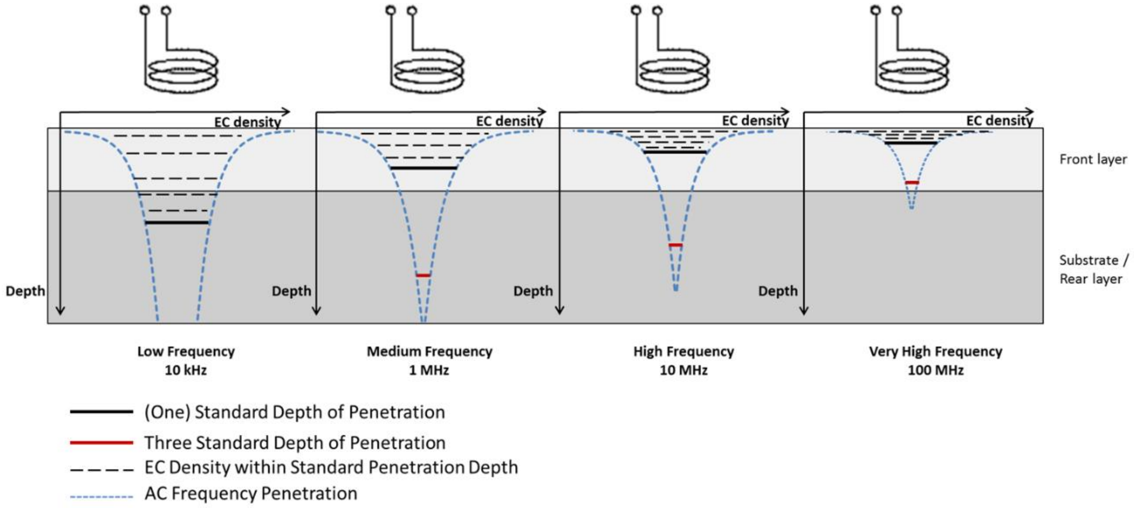

Figure II. 4 Effect of Excitation Frequency on Eddy Current Penetration

Starting with Maxwell's equations and assuming a sinusoidal field $e^{i\omega t}$, we can derive the diffusion equation for the magnetic field H:

$$\nabla^2 H = j\omega\mu\sigma H \qquad \text{(II.19)}$$

For a semi-infinite conductive slab with the magnetic field applied parallel to the surface (along the (y)-axis) and varying with depth (z), the equation simplifies to a one-dimensional form:

$$\frac{\partial^2 H_y}{\partial Z^2} = j\omega\mu\sigma H_y \qquad \text{(II.20)}$$

The solution to this differential equation is:

$$H_y(z) = H_0\, e^{-\alpha z} e^{i(\omega t - \beta z)} \qquad \text{(II.21)}$$

Where α and $\beta = \sqrt{\frac{\omega\mu\sigma}{2}}$ are the real and imaginary parts of the propagation constant $\gamma = \sqrt{j\omega\mu\sigma}$ Solving for : $(1 + j)\sqrt{\frac{\omega\mu\sigma}{2}}$

Thus, $\alpha = \beta$. The skin depth δ is defined as the inverse of the real part of the propagation constant:

$$\delta = \frac{1}{\alpha} = \sqrt{\frac{2}{\omega\mu\sigma}} \qquad \text{(II.22)}$$

This equation shows that the skin depth decreases with increasing frequency ω, magnetic permeability μ, and conductivity σ (For example, in aluminium σ =3.5 .10^7[S/m], μ =μ_0= 4 π .10^{-7}[H/m] at a frequency of 100 kHz , ω = 2π .100 .10^3, the skin depth is: $\delta \approx 0.2.1mm$)

This shallow penetration depth makes ECT highly sensitive to surface and near-surface defects but limits its ability to detect deep internal flaws, which is why it is often complemented by methods like UT or RT for subsurface inspections.

II.3.1.b. *Interaction with defects*

When a defect (a crack, void, or inclusion) is present in the material as showing in Figure II.2,4 it disrupts the flow of eddy currents. For a surface crack, the eddy currents must detour around the defect, increasing their path length and altering the secondary magnetic field they produce. This change in the secondary field affects the coil's impedance, which is the primary measurement in ECT

The impedance (Z) of the coil is a complex quantity, consisting of resistance (R) and inductive reactance X_L:

$$Z = R + jX_L \qquad \text{(II.23)}$$

The presence of a conductive material near the coil introduces a reflected impedance due to the eddy currents. The total impedance of the coil can be modelled using the Dodd and Deeds analytical solution for a coil above a conductive half-space. For a simple case, the change in impedance ΔZ ,due to the material and defects, can be expressed as:

$$\Delta Z = j\omega \int A_p J_e \, dV \qquad \text{(II.24)}$$

Where A_p is the magnetic vector potential of the primary field, J_e is the eddy current density, and the integral is taken over the volume (V) of the material. Defects alter J_e, leading to a measurable ΔZ For a more practical model, consider a surface crack in a flat plate. The crack can be approximated as a region of zero conductivity ($\sigma = 0$) within the conductive material. The eddy currents detour around the crack, increasing the effective resistance and decreasing the inductance of the coil. This results in a change in the impedance plane, often plotted as a Lissajous curve on an ECT instrument, where the real part (resistance) and imaginary part (reactance) of ΔZ Zare are displayed. The shape and magnitude of this curve depend on the crack's depth, length, and orientation relative to the coil.

II.3.1.c. *Lift-off effect*

The lift-off effect refers to the change in impedance caused by varying the distance between the coil and the material surface. As the coil is moved away from the surface, the strength of the induced eddy currents decreases, reducing the secondary magnetic field and altering the coil's impedance, [71]. Mathematically, the lift-off effect can be modelled by introducing a distance (h) (lift-off) in the boundary conditions of the Dodd and Deeds solution. The impedance change due to lift-off is typically a linear shift in the impedance plane, distinct from the signal caused by defects, allowing operators to distinguish between the two.

The lift-off effect is described by:

$$Z(h) = Z_0 + \Delta Z_{lift-off}(h) \qquad \text{(II.25)}$$

Where:

Z_0 is the impedance of the coil in air, and $\Delta Z_{\mathrm{lift-off}}(h)$ decreases exponentially with (h). In practice, lift-off is a source of noise in ECT, but it can also be used to measure the thickness of non-conductive coatings (paint on metal) by calibrating the impedance change to the lift-off distance.

II.3.1.d. *Frequency selection and defect detection*

The choice of frequency in ECT is critical, as it affects both the skin depth and the sensitivity to defects,[75]. The standard depth of penetration δ determines the depth at which defects can be detected. For surface defects, a higher frequency (smaller δ)is used to concentrate the eddy currents near the surface, increasing sensitivity to shallow flaws. For near-surface or subsurface defects, a lower frequency (larger δ)chosen to allow deeper penetration.

The relationship between defect size and frequency is often characterized by the phase lag of the eddy current signal. The phase lag ϕ at a depth z is given by:

$$\phi = \frac{z}{\delta} \qquad \text{(II.26)}$$

A defect at depth z causes a phase shift in the impedance signal, which can be used to estimate the defect's depth. For example, a defect at $z = \delta$ causes a phase lag of 1 radian=57°. This phase information, combined with amplitude changes, allows ECT to characterize the depth and size of the defect.

II.4. *Practical application: impedance plane analysis*

In practice, ECT instruments display the coil impedance on an **impedance plane**, where the x-axis corresponds to the **resistive component** R and the y-axis to the **reactive component** X_l. The presence of a defect produces a characteristic trajectory in this plane, often forming a loop or curve. For example:

- **Surface cracks** increase resistance (due to longer current paths) and decrease inductance (due to reduced coupling), shifting the signal to the **right and downward,** [76].
- **Lift-off** produces a straight-line shift, typically at an angle different from that of defect signals, [70].
- **Material variations** (changes in conductivity or permeability) cause signal shifts in distinct directions, [77].

By calibrating the instrument with known defects, operators can interpret these trajectories to identify and characterize flaws. Furthermore, advanced ECT systems apply **multi-frequency techniques** to distinguish defect signals from noise sources (such as lift-off or material property variations) by solving a system of equations for impedance at different frequencies, [78].

II.5. *Modelling subsurface defects*

For subsurface defects like internal cracks, laminations, or voids, the mathematical model becomes more complex. The eddy currents must penetrate to the defect's depth, which requires a lower frequency to increase the skin depth. The defect's effect on the eddy currents is weaker due to the exponential decay of the current density, making detection more challenging. Finite Element Method (FEM) simulations are often used to model these scenarios, solving Maxwell's equations numerically for a given geometry, defect size, and frequency,[79].

For a simple subsurface crack, the impedance change can be approximated using perturbation theory, where the defect is treated as a small perturbation to the eddy current distribution. The change in impedance ΔZ is proportional to the defect's volume and the square of the eddy current density at its location:

$$\Delta Z \propto \int \mid J_e \mid^2 \, dV \qquad \text{(II.27)}$$

This integral is smaller for deeper defects due to the exponential decay of J_e, explaining why ECT is less sensitive to deep subsurface flaws compared to methods like UT or RT.

II.6. *Driving methods for defect imaging*

The method by which array coils are activated—known as the driving method—significantly influences imaging performance in eddy current testing. This research adopts **multiplexed excitation** as the primary driving method, [80], prioritizing high-resolution defect imaging.

II.6.1. *Multiplexed excitation (sequential firing)*

At the core of this study, multiplexed excitation involves activating one coil at a time in a controlled sequence, with each signal captured independently. This approach simplifies data acquisition and signal interpretation, enabling precise surface defect mapping. As demonstrated in the C-scan results, multiplexed excitation delivers excellent spatial resolution. However, its sequential nature results in slower scanning speeds—an acceptable trade-off for the enhanced image clarity and reduced system complexity it offers.

For an ECA with N_c coils, the (k) coil is excited as:

$$\begin{cases} I(t) = I_0 e^{i\omega t}\,, (K-1)T_m \;\, x \le t < KT_m \\ \qquad\qquad\qquad\qquad \cdot \\ \qquad\qquad\qquad\qquad \cdot \\ \qquad\qquad\qquad\qquad\quad 0,\ otherwise \end{cases} \tag{II.28}$$

Where:

T_m is the multiplexing period,

$T_{cycle} = N_c T_m$ The impedance of the (k)-th coil is:

$$Z_k(t) = R_k + jX_{K,L} + \Delta Z_k(t) \tag{II.29}$$

Where, $Z_k(t) = \Delta Z_{k,amp}, e^{j(2\pi f t + \phi_k)}$, with $\Delta Z_{k,amp}$ and ϕ_k reflecting defect-induced changes.

II.6.1.a. *Alternative methods:*

- **a. Phased Excitation** activates groups of coils simultaneously to achieve greater penetration depth, beneficial for applications like weld inspection. While faster, it requires more complex control and signal processing, [81].
- **b. Simultaneous Excitation** energizes all coils at once, ideal for rapid, wide-area scans such as corrosion mapping. However, it demands high-end electronics, increasing cost, and system complexity,[82].

By contrast, the **multiplexing method** used in this research strikes a practical balance—achieving high-resolution imaging with relatively simple and cost-effective hardware.

II.6.1.b. Practical tips for high-quality defect imaging (harmonic mode with multiplexing)

a. **Multi-Frequency Excitation:** While the harmonic mode typically employs a single frequency, continuous frequency sweeps (ranging from 100 kHz to 1 MHz) have been among the most widely used techniques for defect imaging,[83] However, this approach was not adopted in our study.

b. **C-Scan Imaging Software:** Essential for this research, the C-scan imaging process was implemented using MATLAB, where the variations in ΔZ were mapped into 2D color images. This visualization enables clear identification of defects as distinct patterns, as demonstrated in the aluminum plate example.,[84].

c. **Calibration:** Using reference standards with known defects (EDM notches) ensures accurate defect sizing in harmonic mode inspections, enhancing the reliability of C-scans produced via multiplexing.

II.6.1.c. Integration of analytical, finite element, and practical approaches

The analytical model describes harmonic excitation and multiplexing, producing high-resolution C-scans, as validated by the aluminum plate example. The FEM enhances this by solving the $A - V$ equations, incorporating boundary and continuity conditions to model complex scenarios accurately. The focus on harmonic mode and multiplexing aligns with their strengths in surface defect imaging, offering simplicity and high resolution, while practical tips like C-scan software and calibration ensure actionable defect detection in real-world applications.

II.7. *Conclusion*

This chapter has established a comprehensive framework for ECT, emphasizing the harmonic mode with the multiplexed method for defect imaging, as adopted in this research. The analytical model, finite element formulation, and practical insights collectively demonstrated the capability for precise surface defect detection, exemplified by the high-resolution C-scan of an aluminum plate. Although alternative modes (pulsed) and methods (phased excitation) provide advantages such as deeper penetration or faster scanning, the harmonic multiplexed approach offers superior simplicity and resolution, making it particularly well suited for applications like aerospace surface inspections.

Building on this foundation, the following chapter presents the ***application and simulation results****, where the developed models are implemented and validated through numerical experiments. These simulations not only highlight the effectiveness of the proposed framework but also illustrate its potential for practical deployment in real inspection scenarios.*

.

Chaptre III

Simulation-based validation and application of eddy current testing for defect imag

Chaptre III Simulation-based validation and application of eddy current testing for defect imaging

III.1. *Introduction*

Building on the theoretical and numerical framework established in the previous chapters, this chapter focuses on the practical validation and advanced application of Eddy Current Testing (ECT) for defect characterization. The aim is twofold: first, to validate the developed analytical and finite element models through comparison with experimental measurements, and second, to extend the investigation toward high-resolution imaging using a multiplexed multi-element sensor approach.

In the first part, the finite element model implemented in COMSOL® Multiphysics with the AC/DC module,[85]it is validated against experimental data obtained using a Phasec 2D ECT device. An absolute coil sensor is employed to perform two-dimensional scans of test specimens, enabling a direct comparison between simulated and measured signals. This validation step is essential to ensure the accuracy and reliability of the modeling framework, thereby providing a solid basis for further developments.

The second part of the chapter addresses advanced defect imaging. Here, an absolute coil operating in harmonic mode is virtually arranged into a sensor array using the multiplexing method, where sequential coil activation avoids mutual interference and provides high-resolution mapping. This approach generates detailed two-dimensional C-scans of test plates,[86] and pipes, highlighting the location, shape, and size of both surface and subsurface defects. The harmonic excitation mode, characterized by a single-frequency sinusoidal current, is selected for its simplicity and its ability to precisely control penetration depth, making it particularly effective for near-surface defect detection.

Through this two-step methodology—first validating the numerical model with experimental measurements, and then applying a multiplexed array strategy for imaging—this chapter demonstrates (Figure III.1) the effectiveness of the proposed ECT framework. The results confirm the potential of harmonic mode operation combined with multiplexed sensing for accurate and reliable defect characterization, laying the groundwork for future experimental extensions.

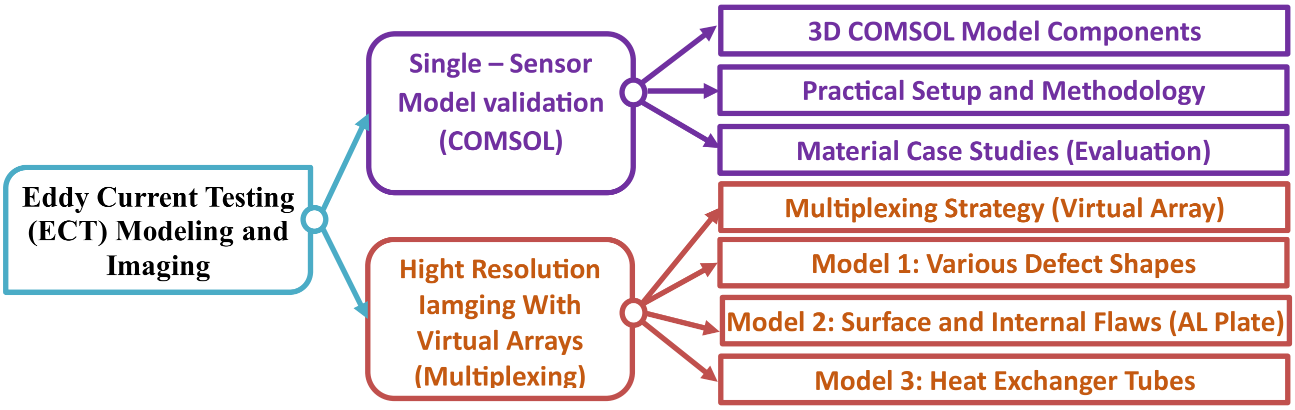

Figure III. 1 Structure of Eddy Current Testing (ECT) Modeling and Imaging defect

III.2. *Proposed 3D ECT model in COMSOL*

Initially, a 3D geometry was constructed in COMSOL Multiphysics to mirror the dimensions and conditions of the experimental model.

Metallic Plate: A rectangular conductive plate was modeled with dimensions representative of the actual specimen, as shown in Table III.2 and Figure III.2. This plate serves as the material under investigation.

Defects: Three surface defects were introduced into the plate model, represented as rectangular notches (or cracks) with varying dimensions. These defects were placed at different distances from each other to study the effect of defect proximity on the eddy current response. Their detailed dimensions are provided in Table III.3 and illustrated in Figure III.2.

Sensor: The virtual sensor dimensions, shown in Figure III.3, were measured with a caliper, and the obtained values closely matched those of the actual sensor. In the COMSOL model, the sensor was represented as a multi-turn coil, requiring parameters such as the number of turns (Table III.1), wire cross-section, and electrical conductivity. Furthermore, since the coil geometry can vary—circular, linear, or custom—it must be defined in advance according to the inspection requirements.

Sensor properties	
Nombre of coil	**1**
External radius [mm]	**4**
Internal radius [mm]	**2.5**
Height [mm]	**2**
Number of turns	**200**

Table III. 1 Sensor characteristics

The lift-off, defined as the distance between the sensor and the inspection target, is set to 1 mm. This configuration enables the sensor to move along the plate, covering all areas with defects. In this context, and to broaden the scope of this study, the inspection is carried out on three plates made of **Aluminum (Al)**, **Titanium (Ti)**, and Austenitic **Aus)**, whose properties are provided in the table and figure below.

Plate	**Length (mm)**	**Width (mm)**	**Thickness (mm)**	**Cconductivity (M Sm^{-1})**
Al	**101.8**	**25.6**	**9**	**37.7**
Au	**76.3**	**25.6**	**6.5**	**1.4**
Ti	**80.2**	**3.5**	**8**	**2.5**

Table III. 2 . Characteristics of the plates.

Depth of defect	Al Plate	Au Plate	Ti Plate
P1 (mm)	1	1	1.016
P 2 (mm)	0.5	0.5	0.508
P3 (mm)	0.2	0.2	0.203

Table III. 3 .Depth P1, P2 and P3 of artificial defects in each plate

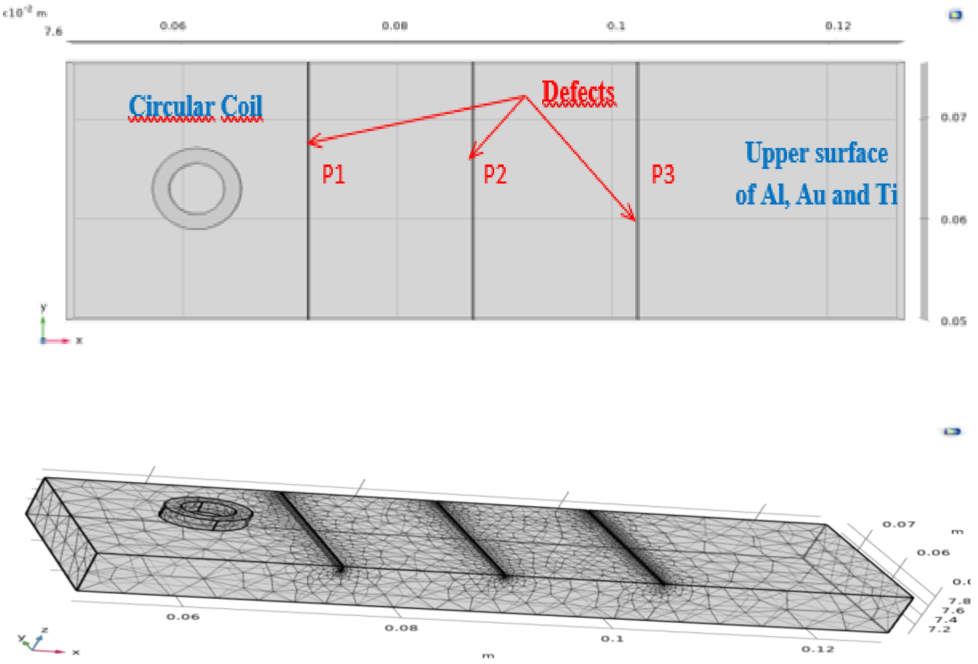

Figure III. 2 Three defects of different depths on Al, Au, and Ti plates

III.3. *Practical setup and methodology*

In the context of Eddy Current Testing (ECT) for Non-Destructive Testing (NDT), we employed a **SOFRANEL Phasec 2d** device, well known for its robustness and precision in electromagnetic inspections of conductive materials. The technique is based on electromagnetic induction: an alternating current passing through a coil generates a magnetic field, which induces eddy currents in the test piece. The interaction of these currents with possible defects alters the coil's electrical response, enabling defect detection (Figure III.3).

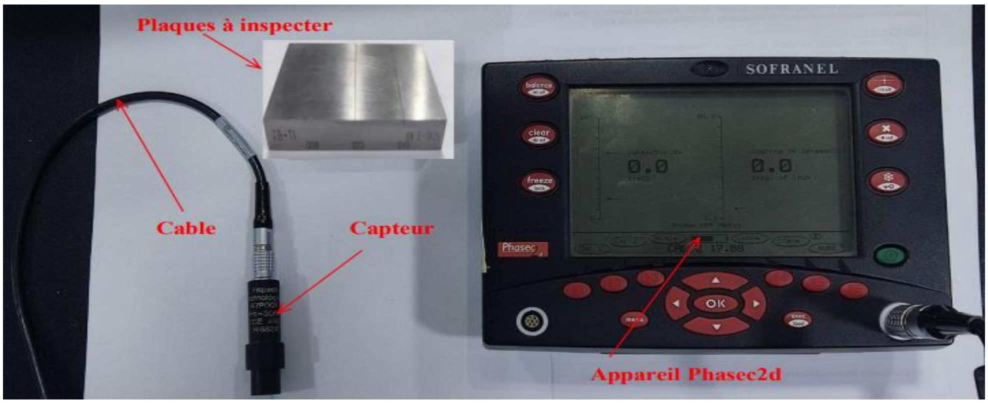

Figure III. 3 Experimental device with a plate inspected and a sensor

The experimental setup consisted of:

- **ECT Device:** SOFRANEL Phasec2d portable unit with an XY display for vector visualization of material responses (phase and amplitude). Integrated functions include phase and gain adjustment, freeze, balance, and sweep modes.
- **Sensor:** Single-element surface probe, used to induce eddy currents and collect return signals, manually scanned over the plate surface.

Figure III. 4 Pencil (probe) the probe

- **Test Samples:** Three metallic plates (Aluminium, Titanium, and Austenitic) containing artificial defects of identical dimensions.

- **Experimental procedure:** Each material was tested separately, with phase and gain parameters adjusted to optimize signal visibility. Standard parameters included a **phase setting of 206.0°**, variable gain (40.5 for titanium), and sweep mode activated. The display mode (XY, SPOT, or DISP) was selected according to the required measurement precision.

III.3.1. *Evaluation and interpretation of findings*

The following section presents the simulation results and defect signatures for each laminate, together with a comparison to the experimental measurements. The sensor was excited using a sinusoidal AC source operating in the tens to hundreds of kilohertz range, selected according to the electrical properties of the material under investigation. This frequency range was chosen to enhance the generation of surface eddy currents and improve detection sensitivity.

The figures illustrate the calculated variations in sensor impedance as it scans along the oxidation (OX) axis for aluminum (Al), austenitic stainless steel (AUS), and titanium (Ti) laminates. The combination of sensor movement across the laminates and optimized parameter settings produced highly representative defect signatures.

III.3.1.a. Case of Aluminum (Al)

Figure III.5 presents the simulated defect fingerprints along the aluminum plate, together with the corresponding Lissajous curve obtained by plotting the imaginary versus real components of the sensor impedance. Figure III.6 shows the experimental results obtained with the Phasic2d device, which records only the Lissajous representation. The experimental trace appears sharp and well-defined, oriented toward the upper left, with a pronounced phase separation—indicating a strong sensor response. The curve is smooth, continuous, and free of visible instabilities.

From a technical standpoint, aluminum's high electrical conductivity ($\sigma \approx$ 35–38 MS/m) promotes the generation of strong, uniformly distributed surface eddy currents. At higher excitation frequencies, the reduced penetration depth enhances sensitivity to surface and near-surface defects. As a result, the signal clearly reflects disturbances caused by cracks, pores, or similar discontinuities.

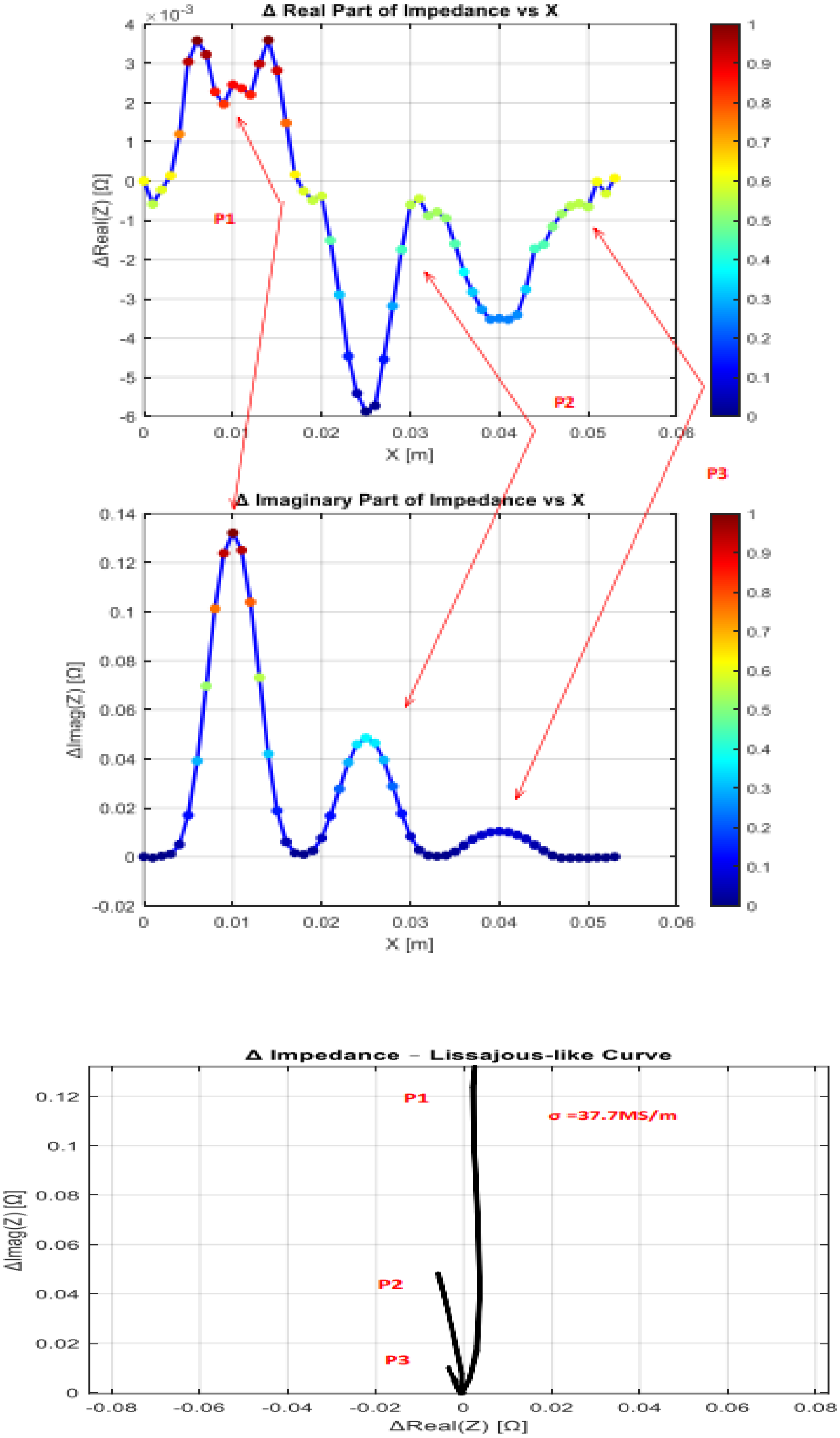

Figure III. 5 Impedance components and Lissajous curves for an AL plate

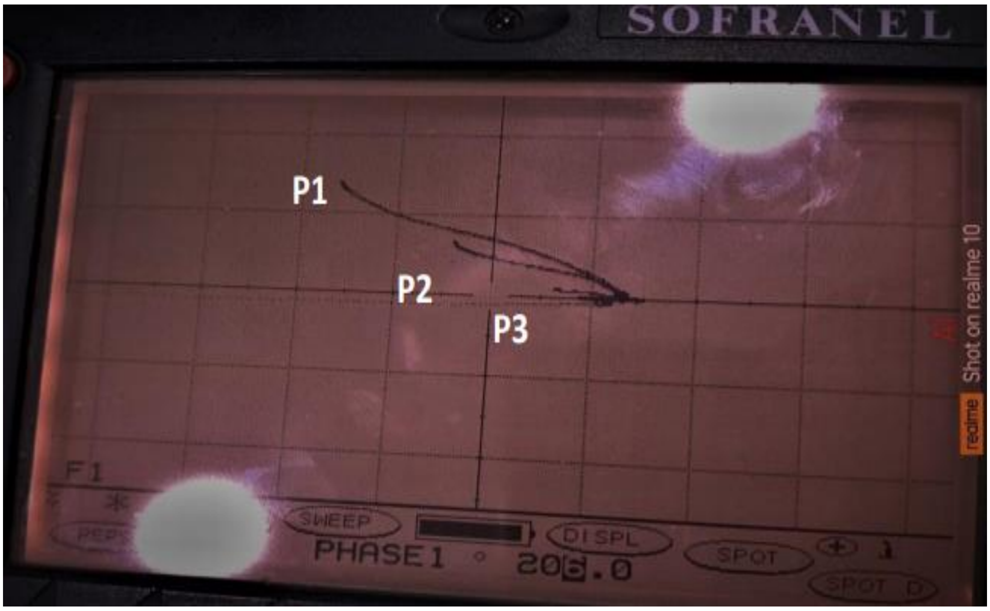

Figure III. 6 Signal obtained when scanning the aluminium plate

In a specific conclusion, the signal characteristics confirm that the sensor is highly effective for inspecting conductive materials such as aluminum, as any local perturbation in the magnetic field produces an immediate and pronounced deflection in the Lissajous trace. Furthermore, the defect signature shapes observed experimentally are consistent with those predicted by simulation.

III.3.1.b. *Case of austenite (AUS)*

Figure III.8 presents the simulated defect signatures along the austenitic stainless steel (AUS) plate, together with the corresponding Lissajous curve obtained by plotting the imaginary versus real components of the sensor impedance. Figure III.8 shows the experimental results obtained with the Phasic2d device, which provides only the Lissajous representation. Compared to aluminum, the trace is longer with less curvature, exhibiting moderate phase separation—typical of a material with slightly higher magnetic permeability. Although the response is weaker than in aluminum, the signal remains stable, clear, and interpretable.

From a technical perspective, austenitic stainless steel is a non-magnetic alloy with lower conductivity ($\sigma \approx 1.4$–$1.6\ MS/m$) than aluminum. Consequently, its electromagnetic response is intermediate: less sensitive than aluminum but more stable than titanium. Its relatively low magnetic permeability also influences the phase characteristics of the signal.

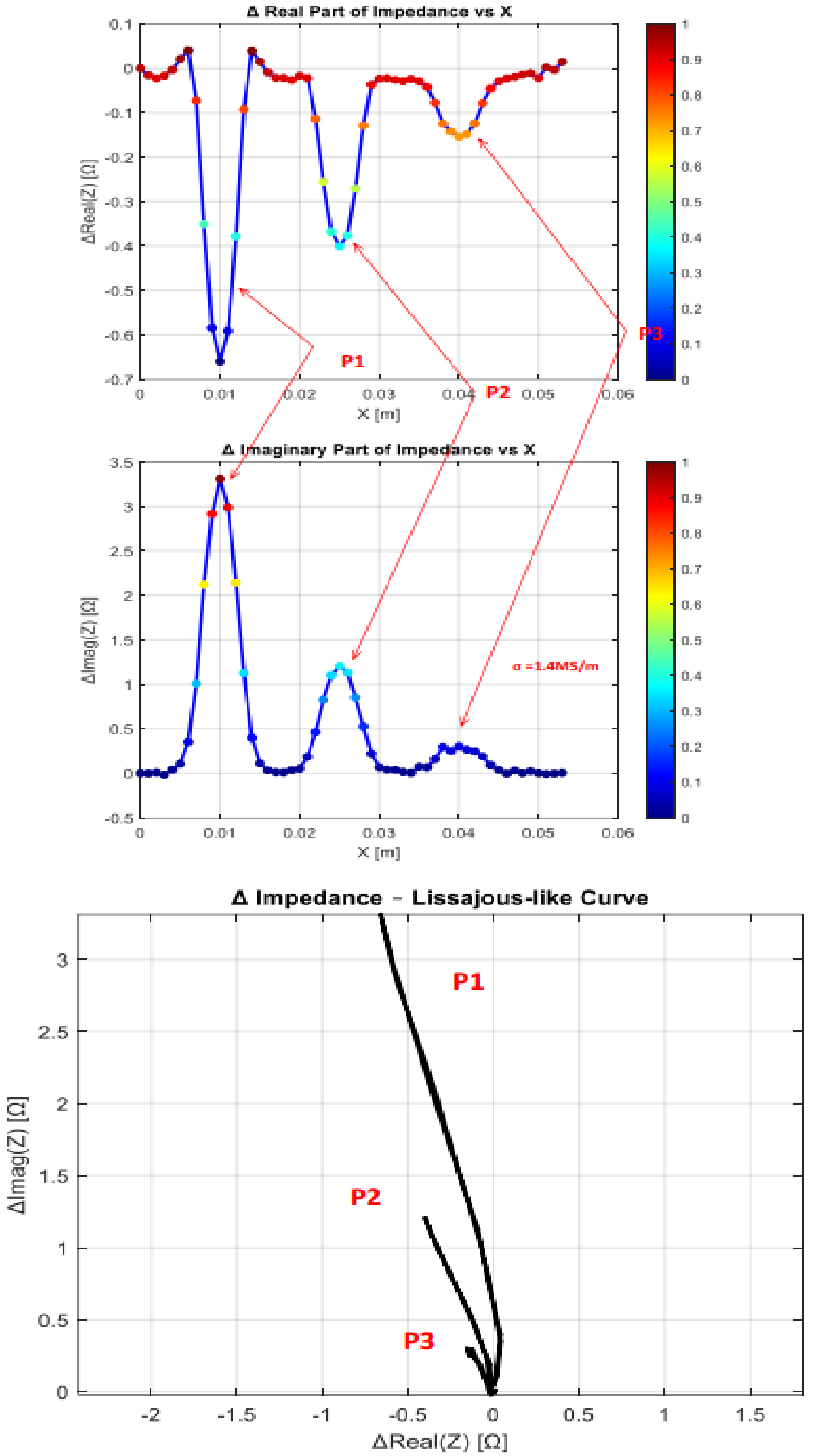

Figure III. 7 Impedance components and Lissajous curves for an Aus plate

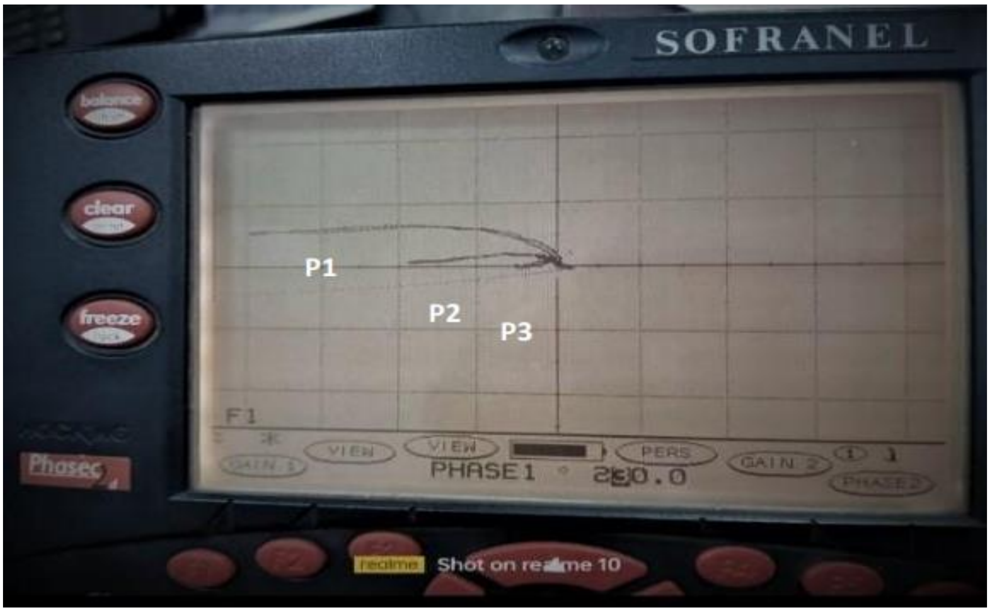

Figure III. 8 Signal obtained when scanning the austenite plate

In a specific conclusion, austenite provides a reliable basis for defect detection despite its reduced sensitivity. The system remains effective for identifying defects such as fatigue cracks or localized corrosion, provided the measurement parameters are carefully optimized. Moreover, the experimental signatures are consistent with the simulation results, reinforcing the accuracy of the modeled response.

III.3.1.c. Case of Titanium (TI)

Figures III.9 and III.10 present the Lissajous curves for titanium, obtained from simulation and experimental measurements, respectively.

Visual observations: The trace appears shorter, less pronounced, and exhibits lower amplitude compared to aluminum and austenite. Nonetheless, it remains stable, with a noticeable deflection at the defect location. A gain setting of 40.5 was required, reflecting the need for stronger amplification. Titanium's relatively low conductivity ($\sigma \approx 1.8\text{–}2.4\ MS/m$) generates weaker eddy currents, which in turn reduce the overall response amplitude. As a result, higher amplification is necessary, though this may also increase susceptibility to noise.

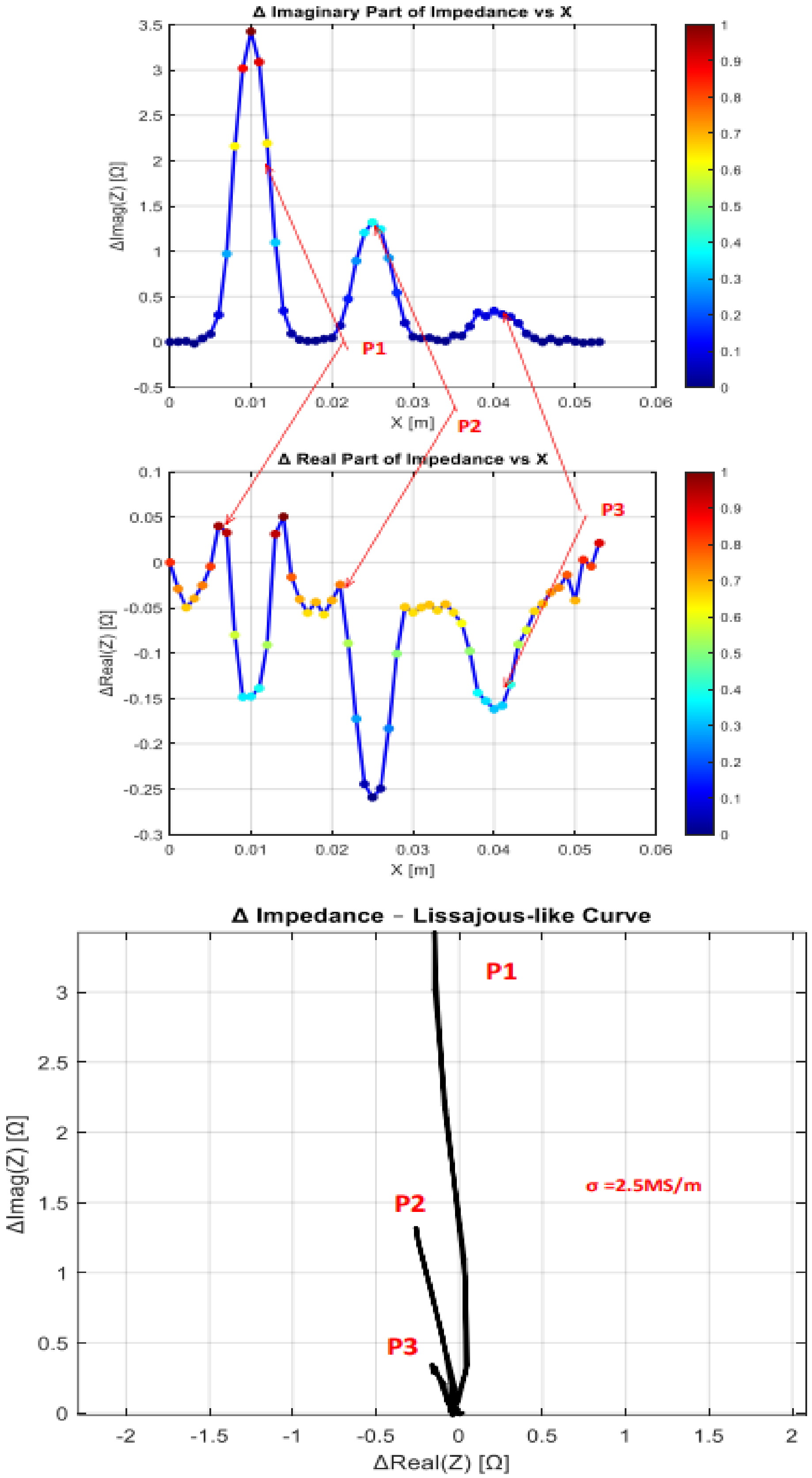

Figure III. 9 Impedance components and Lissajous curves for a Ti plate

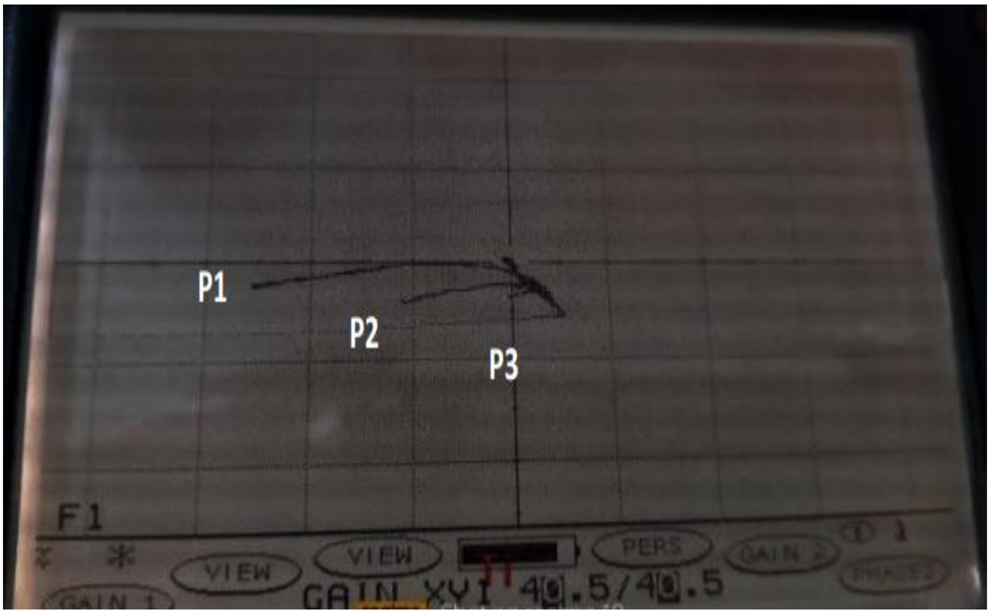

Figure III. 10 Signal obtained when scanning the Titan plate

Specific conclusion: Both simulation and experimental results confirm that defect detection in titanium is more challenging and demands precise parameter optimization. While the system is capable of identifying anomalies, detection reliability is strongly dependent on sensor sensitivity and effective signal processing.

III.4. *Development of high-resolution imaging with multiplexed virtual arrays*

After validating the single-sensor model, which confirmed the reliability of COMSOL® Multiphysics for simulating eddy current testing (ECT) systems, we extended the study using the AC/DC module in harmonic mode with a sinusoidal excitation current. This approach enables targeting specific penetration depths across the material surface. To achieve high-resolution imaging, a multiplexing strategy was employed, whereby measurement points are sequentially activated to reconstruct a physical image of the defects. This is implemented by translating a single absolute coil to form a virtual sensor array, thereby mitigating cross-inductance effects between adjacent positions (Figure III.11).

The absolute mode was selected for its simplicity and high sensitivity, making it particularly suitable for initial simulations aimed at understanding impedance variations prior to introducing advanced noise-rejection techniques such as differential or reflective configurations. The simulations were carried out on both plates and tubes, representative of industrial applications such as aircraft panels and heat exchanger tubing, incorporating a range of surface and internal defects (linear cracks and circular voids) of varying sizes and orientations.

This setup provides a robust framework for analyzing sensor positioning, configuration, and coil design, while optimizing harmonic-mode imaging. The resulting virtual sensor arrays yield comprehensive data matrices that enable accurate defect characterization and imaging.

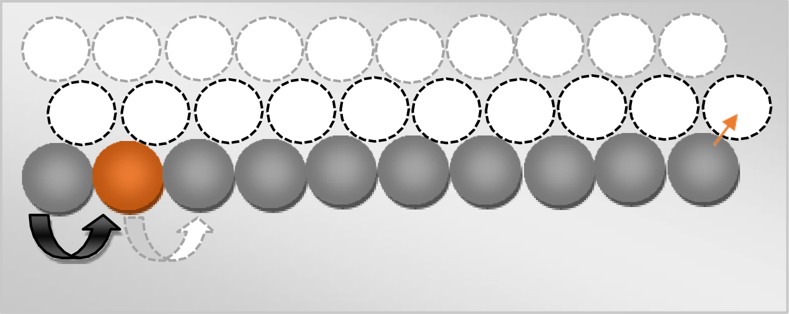

Figure III. 11 Illustration of the multiplexing method based on the eddy current array

The inspection process begins with the activation of the first sensor element, indicated in orange, followed sequentially by the activation of the remaining elements, colored in gray. Once all elements have been activated, the sensor array shifts forward in precise 1 mm increments, as shown by the transparent circles in the figure, progressively covering the entire area under inspection. This scanning cycle continues until the complete surface has been examined.

This method, known as multiplexing, involves sequentially activating each coil to prevent the simultaneous excitation of adjacent elements. This approach minimizes the adverse effects of mutual inductance—unintended magnetic coupling between neighbouring coils—which can compromise signal integrity. By using an internal multiplexing system, the excitation of each coil is precisely controlled, ensuring clean, interference-free measurements. The resulting impedance data collected by each sensor element during the scan generate high-resolution 3D images of the inspected area, allowing for accurate visualization and characterization of defects.

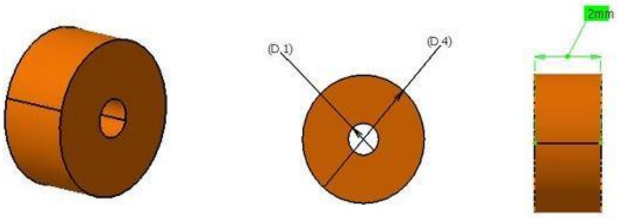

Figure III. 12 The dimensions of the sensor coil

Each sensor coil has 100 turns of wire with 0.03 × 10^{-6} m^2 cross-sectional area and 6 × 10^7 S/m conductivity.

The scanning procedure is performed with the probe positioned parallel to the y-axis. The lift-off, which is the distance between the coil and the plate, is set to 0.5 mm. During the scanning process, each sensor element is advanced step-by-step along the aluminum plate, which has a conductivity of 3.774.107 S/m.

III.5. *Executing and showcasing the proposed models*

III.5.1. *The first model*

The study examines three different defect shapes: C-shape, I-shape, and V-shape. There have been simulated different flaws: straight, inclined, and circular paths, corresponding to C-shape, I-shape, and V-shape defects as illustrated in Table III.4 below and Figure III.13,14.

- **I-Shaped Defect:** This defect consists of two straight segments oriented perpendicularly to each other. Each segment has a length of 20 mm, a width of 1.5 mm, and a depth of 1 mm.

- **V-Shaped Defect:** The V-shaped defect is composed of two equal sides, each measuring 15 mm in length, forming a symmetrical configuration. The vertex of the V-shape includes a convex arc with an outer radius of 2 mm and an inner radius of 1 mm. Both the width and depth of this defect measure 1 mm.
- **C-Shaped Defect:** The C-shaped defect is a semicircle with an outer radius of 17 mm and an inner radius of 15 mm. The width, calculated as the difference between the outer and inner radii, is 2 mm. The depth of the defect is also 2 mm.

Plate parameter value [mm]	**Plate width 100**	**Plate length 100**	**Plate thickness 8**
Defect_I-shape parameter value[mm]	Crack width 1	Crack length 20	**Crack depth 1**
Defect_V-shape parameter value[mm]	Crack width 1	Crack length 30	**Crack depth 1**
Defect_C-shape parameter value [mm]	Crack width 2	Crack length 47.1-53.4	**Crack depth 2**
Sensor parameter value [mm]	Coil inner 0.5	Coil outer 2	**Coil height 2**
Physical parameter value	**Relative Permeability 1**	**Frequency 10000 Hz**	**Lift-off 0.5 mm**

Table III. 4 . Parameter values

The type of element used significantly impacts the number of degrees of freedom required for the numerical resolution of the problem. In our study, we opted for tetrahedral elements in our mesh, as this choice facilitates automatic meshing of various geometries.

The selection of element size greatly influences the accuracy of the numerical solution obtained. To accurately capture the variations in the quantities of interest, it's crucial to tailor the mesh size to the specific problem at hand. Balancing mesh sizes across different domains is illustrated in Figure III.13.

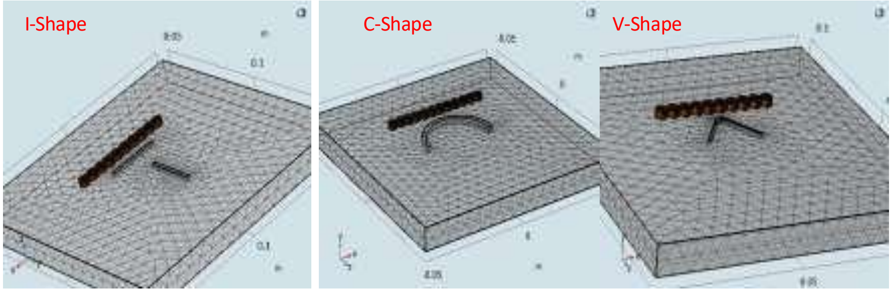

Figure III. 13 Geometry and meshing for different defect shapes

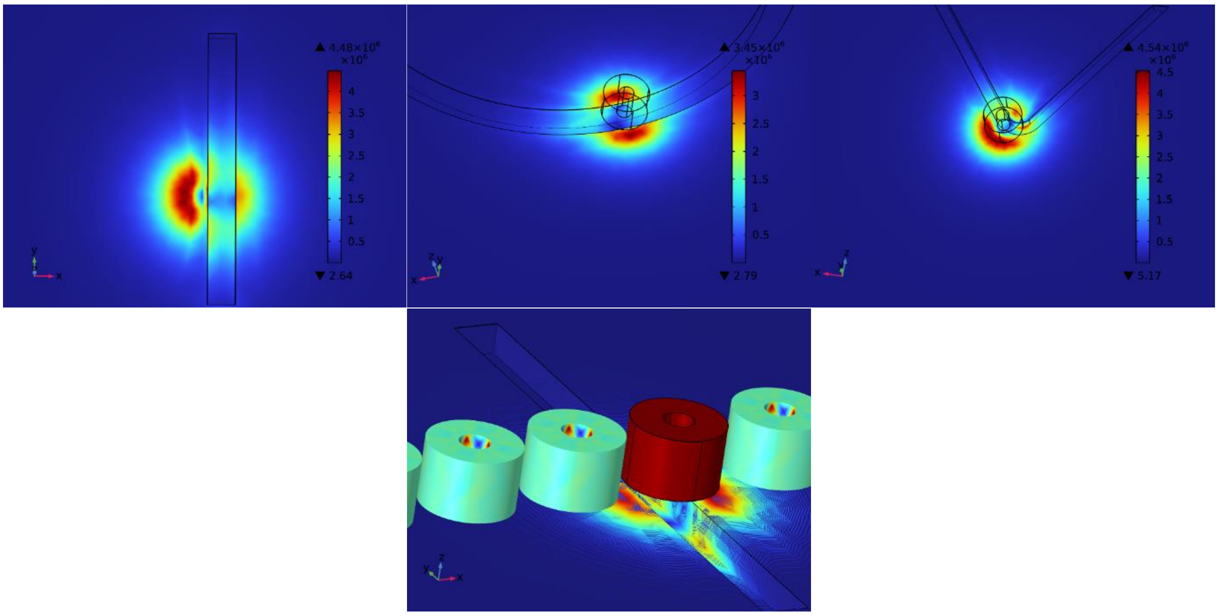

Figure III. 14 Eddy current distribution on different defects

In Figure III.14, we show a mapping of the induced eddy current density according to a linear defect in a straight path (defect 1), where we can observe the extent of the coil influence at the given frequency, allowing us to calculate the impedance as a function of the coil position. [87].

It can be noted that the maximum induced currents decrease when the fault is present, as the value of Jind = 5.20.107 A/m^2 without the defect, and at the first V-shaped defect, the value of Jind1 = 4.54.107 A/m^2, while with the C-shaped defect, which is wider and deeper. We get the value of Jind2=3.45.107 A/m^2, and on the straight defect, we find a value in the range of Jind3=4.48.107 A/m^2. This is what prompts us to interpret these results as the area of the defect varies, which inversely affects the value of the density of induced currents.

It can be concluded that the proposed defect models are very acceptable, allowing them to be used to obtain the required images for a multi-element multiplex system.

III.5.1.a. Reconstruction of defect shape from the impedance amplitude

Firstly, we move the eddy current array (ECA) sensor according to the appropriate axis, and we record the obtained impedance and position of each element. Then, we reconstruct the cartography of the impedance on the scanned surface for different defect shapes (I, C, and V shapes). In fact, the obtained results are shown in Figure III.15.

Upon analyzing the results obtained in all three cases, it is evident that the defect has been successfully reconstructed with its true shape and trajectory. As a result, the diagnosis of the defect has become not only faster but also more accurate and reliable. However, for a more comprehensive assessment of the defect, it is crucial to determine its unknown depth. This aspect can be addressed in future work by utilizing techniques such as neural networks or other probabilistic and deterministic methods to extract and track the defect depth through the impedance measurements in the affected area.

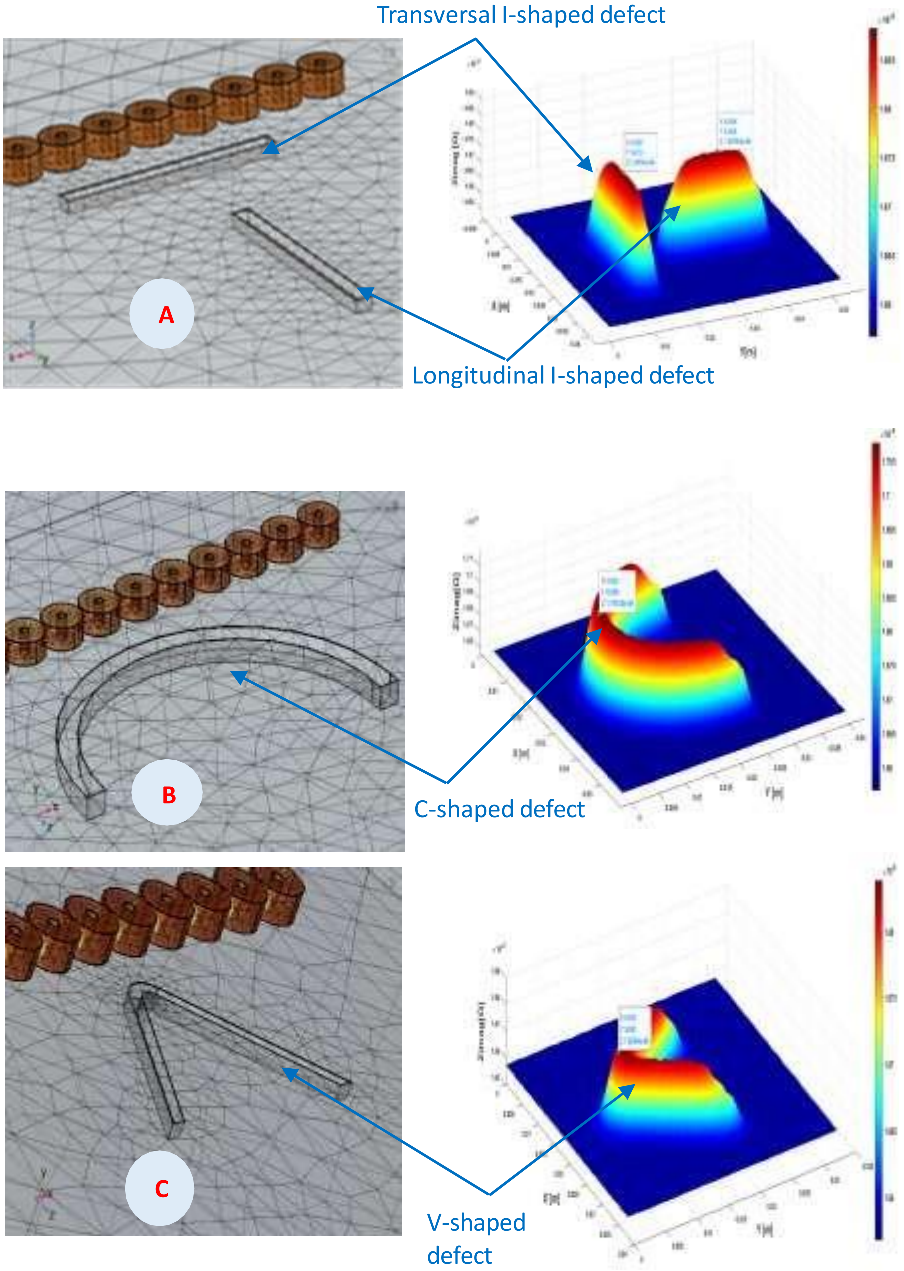

Figure III. 15 Defect shape reconstruction from impedance amplitude imaging for three cases. A, B and C represent I, C and V defect shapes, respectively

To validate the technique's effectiveness in detecting complex defect paths, a randomly generated zigzag defect was modeled with dimensions of 20 mm in length, 1.5 mm in width, and 1 mm in depth, as illustrated in Figure III.16. Each sensor element (Figure III.11) was configured with a coil wire cross-sectional area of 0.03×10^{-6} m^2, 100 turns, and a conductivity of 6×10^7 S/m. The scanning was conducted parallel to the y-axis with a lateral offset of 0.5 mm. During the process, the probe advanced incrementally across the aluminum plate—characterized by a conductivity of 3,774,107 S/m—moving each sensor element step by step. Using the previously described approach, the imaging results successfully reconstructed the defect's shape and path with high accuracy, as shown in Figure III.17.

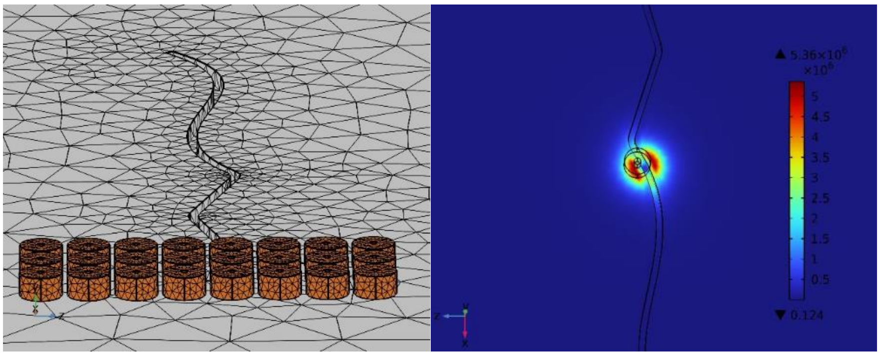

Figure III. 16 Random defect network following a zigzag path (left) with the corresponding eddy current distribution (right).

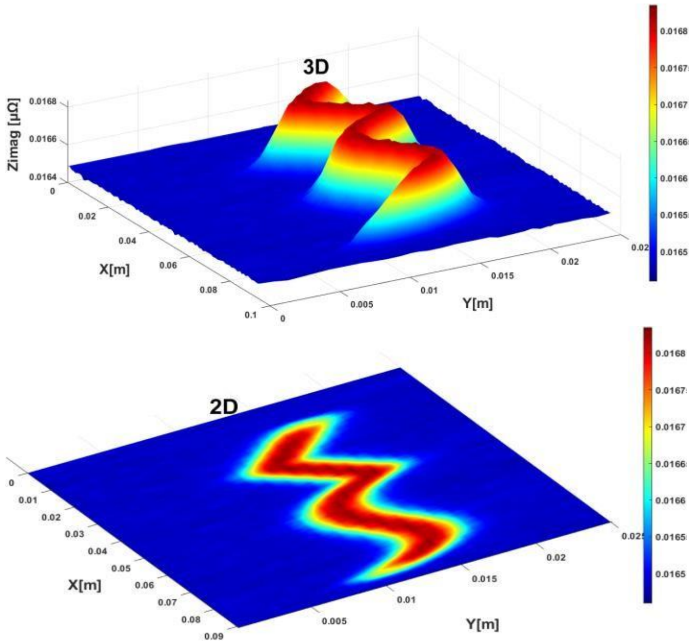

Figure III. 17 3D and 2D imaging of random defect 1 via impedance imaginary values

III.5.1.b. *Results interpretation*

In the initial section of this chapter, we present the simulation results focusing on the shape and path of surface defects, with the outcomes illustrated in Figure III16 and Figure III17. These figures showcase the impedance signals along the defect paths, where the colored regions correspond to variations in impedance values. To generate these visualizations, we perform a comprehensive summation of the impedance signals across the entire virtual sensor array, derived from scanning the impedance values along both the x- and y-axes. This process results in a detailed three-dimensional representation of the defect, viewed at an angle of (60°, 60°), which provides a spatial perspective of the defect's geometry. Additionally, a two-dimensional projection is created at a vertical angle of (0°, 90°), offering a top-down view that complements the 3D visualization. In these representations, the color intensity serves as an indicator of impedance magnitude: regions with increasing intensity toward dark red—whether in the form of points, lines, or surfaces—denote higher impedance values, signifying the presence and severity of defects. This dual visualization approach, combining 3D and 2D perspectives with a color-coded impedance map, enables a clear and precise depiction of the shape and path of randomly distributed surface defects, particularly highlighting their trajectories and spatial characteristics along the defect paths. Such detailed imaging enhances the interpretability of the results, facilitating a deeper understanding of defect morphology and aiding in the accurate assessment of material integrity.

III.5.2. *The second model*

This part investigates the imaging of defects through two distinct models, focusing on both surface and internal flaws in an aluminum plate. The first model features an aluminum plate hosting three straight surface defects, each with a consistent length of 15 mm and depth of 1 mm, but with varying widths of 2 mm, 1.5 mm, and 1 mm, respectively, to explore the impact of defect width on detection sensitivity. The second model introduces a square-shaped defect positioned at the center of the plate, with dimensions of 100 mm × 100 mm × 8 mm. This defect has a side length of 10 mm and an initial depth of 1 mm, starting as a superficial flaw. To study the detection of internal defects, the square defect is progressively lowered beneath the surface, creating internal defects at depths of 0.5 mm, 1 mm, and 2 mm, allowing us to assess the method's capability to detect flaws at varying depths.

For defect examination, we deployed six sensors positioned on the aluminum plate, each maintained at a lift-off distance of 0.5 mm from the surface, as specified in Table III.5. These sensors are alternately activated using the multiplexed method to prevent mutual induction, ensuring clean and interference-free signal acquisition. The sensors advance in precise 1 mm increments during each inspection step, facilitating detailed scanning across the plate's surface. The aluminum plate itself has a conductivity of $3.774 \times 10^{7}\ S/m$ and contains the three distinct defects described.

Sensor Parameter	**Value [mm]**
Coil Inner Diameter	1
Coil Outer Diameter	3
Coil Height	3
Physical Parameter	**Value**
Relative Permeability	1
Frequency	10,000 Hz / 1,600 Hz
Lift-off	0.5 mm

Table III. 5 Parameter Values of the sensor(coil)

The probe used in this study is a sensor array, with each element featuring a coil wire cross-sectional area of $0.04 \times 10^{-6}\ m^2$, 150 turns, and a conductivity of $6 \times 10^{7}\ S/m$. The scanning procedure is conducted parallel to the y-axis, maintaining a consistent lift-off of 0.5 mm. During the inspection, each sensor element advances step-by-step along the aluminum plate, systematically capturing impedance data to map the defects. This meticulous setup ensures comprehensive coverage of the plate, enabling the detection and imaging of both surface and internal defects with high precision.

The study domain was discretized into geometric elements to generate a computational mesh, which provides the framework for numerically evaluating the physical quantities at the nodes. In finite element analysis, the quality and type of mesh play a decisive role in the accuracy, stability, and efficiency of the solution. Using COMSOL Multiphysics, several discretization strategies were investigated, including tetrahedral, hexahedral, and prism elements, each associated with different levels of complexity and degrees of freedom required for the numerical solution. Hexahedral and prism elements generally offer good accuracy in structured domains but can be difficult to apply efficiently in irregular or curved geometries. By contrast, tetrahedral elements offer greater flexibility, allowing for automatic meshing of intricate geometrical domains without requiring manual refinement. For this reason, a mesh composed primarily of tetrahedral elements was selected, as it provides an effective compromise between accuracy and computational cost. This choice ensured that the discretization could adapt smoothly to the geometric intricacies of the plate and the defects being modeled, while still maintaining manageable simulation times. The resulting mesh configuration is presented in Figures III.18, III.19, and III.20, where the refinement near defect regions demonstrates the mesh's ability to capture localized variations in the electromagnetic field. Ultimately, this meshing strategy improves both the precision and the efficiency of the numerical simulation, laying a reliable foundation for the subsequent analysis.

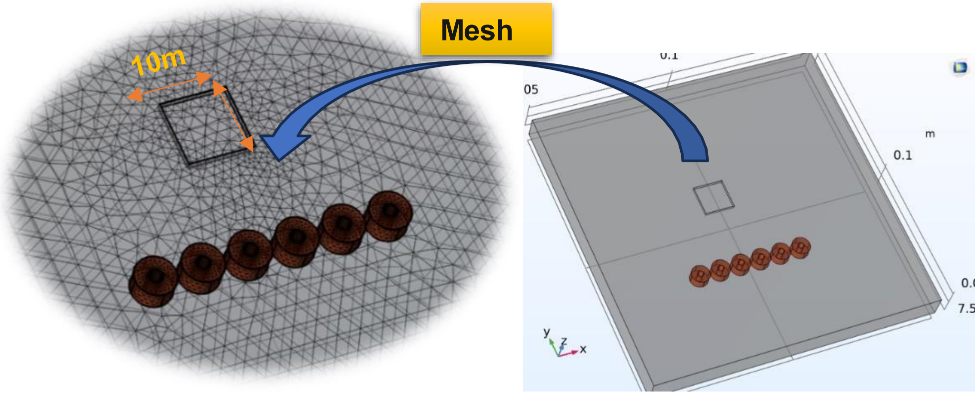

Figure III. 18 . 3D Finite Element Mesh for Three Straight Surface Defects

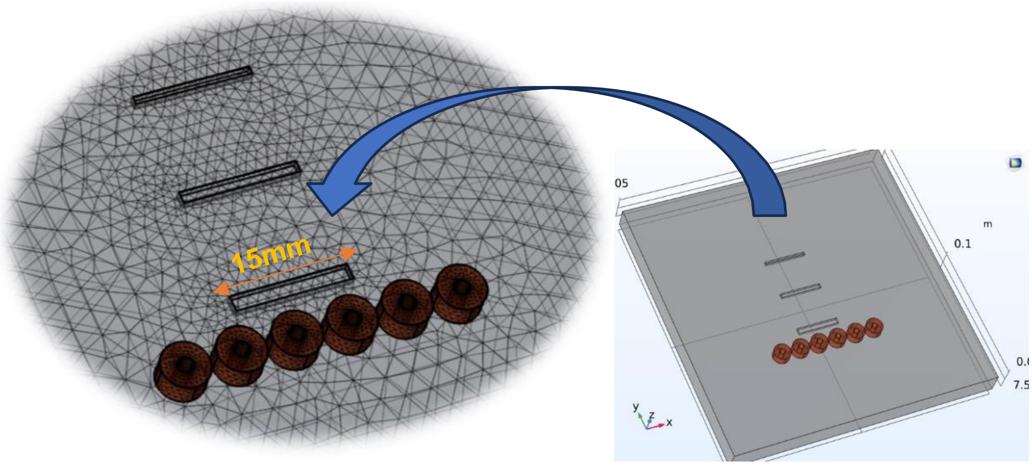

Figure III. 19 . 3D Finite Element Mesh of Square Surface Defect

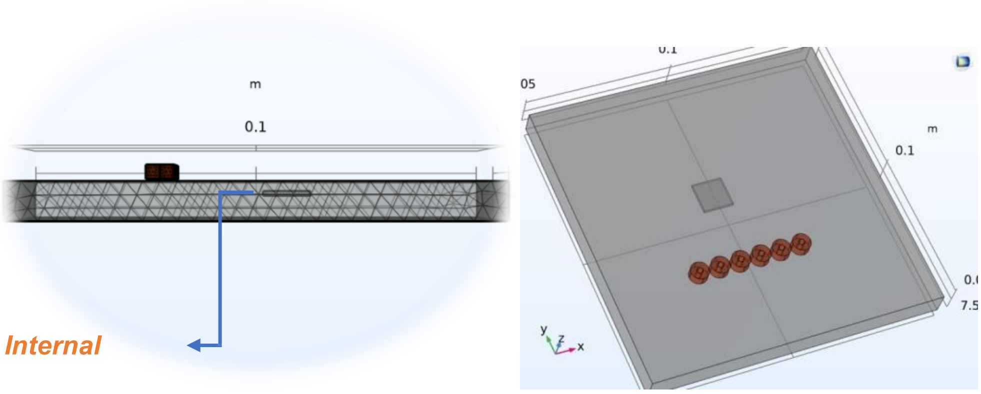

Figure III. 20 .3D Finite Element Mesh of Square Internal Defect

III.5.2.a. *Correlation between induced currents and defect size*

To validate the accuracy of our simulation model, we begin by analyzing the induced currents within the aluminum plate, focusing on the response of a single coil across various sensor positions. This comparative analysis, depicted in Figure III.21, enables us to assess the relationship between the induced currents and defect size, ensuring the reliability of the model in capturing the electromagnetic interactions critical for defect detection. By examining these induced currents at multiple positions, we can establish a foundational understanding of how defect dimensions influence the current distribution, providing a basis for further evaluation of the simulation results.

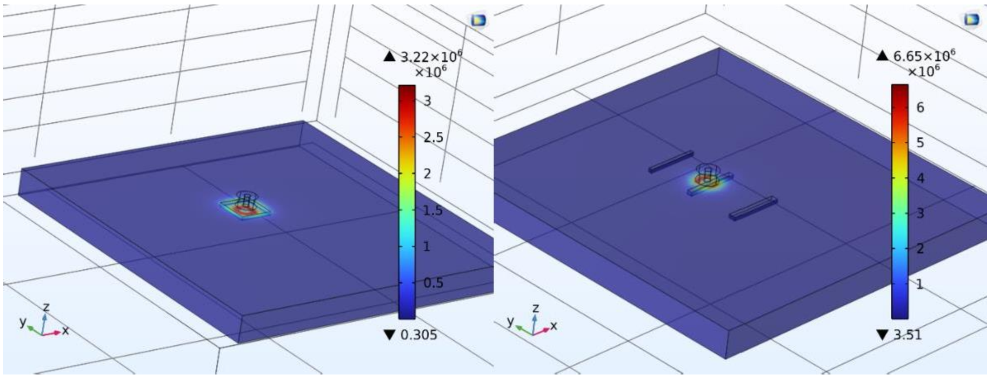

Figure III. 21 Variation of induced currents depending on coil position

Figure III.21 depicts the intensity of the currents induced by the sensor at two distinct defect locations on the aluminum plate, providing insight into the correlation between defect size and induced current density. At the first location, the defect is a linear flaw with a width of 1.5 mm and a length of 15 mm, where the induced current density reaches a peak value of 6.65 × 10^6 $A/.m^2$ In contrast, the second location features a square-shaped defect with a side length of 10 mm, where the induced current density notably decreases to 3.22 × 10^6 A/m^2. This significant reduction in current intensity can be primarily attributed to the variation in defect size and geometry. A larger defect, such as the square flaw, introduces a greater gap and increased distance between the plate's surface and the sensor, leading to a diminished interaction between the sensor's magnetic field and the material. Consequently, this results in a lower induced current density, as the larger defect disrupts the eddy current flow more substantially. These findings affirm the reliability and accuracy of the models developed in COMSOL Multiphysics, as they effectively capture the expected electromagnetic behavior influenced by defect dimensions. With this validation, we can confidently proceed to the next phase of the study, which involves extracting the impedance values at each sensor position to further analyze the defect characteristics and enhance the imaging process.

III.5.2.b. Imaging defects via impedance data collection

To achieve comprehensive defect imaging, we employ multiplexing technology using a sensor equipped with multiple elements, each advancing in precise 1 mm increments during the scanning process. This setup facilitates the development of a robust inspection system capable of examining various sites on the aluminum plate with high spatial resolution. In this approach, each operational mode collects impedance signal data from individual sensing elements, enabling detailed mapping of defect characteristics across the material surface. For surface defects, we utilize a standard frequency of 10,000 Hz, which provides a shallow skin depth suitable for detecting superficial flaws with high sensitivity. Conversely, to enhance the detection of internal defects by maximizing the penetration depth of eddy currents, we reduce the frequency to 1,600 Hz, allowing the magnetic field to probe deeper into the material. This strategic adjustment of frequencies ensures that our inspection system can effectively capture both surface and subsurface anomalies, providing a versatile and thorough analysis of defect distribution and characteristics through impedance data collection.

Figures III.22 and III.23 showcase the 3D and 2D representations derived from top-projection imaging of straight and square-shaped surface defects on the aluminum plate. These images were generated by collecting the imaginary components of impedance values at a frequency of 10 kHz, with impedance values ranging from a minimum of 2.02. 10^{-7} Ω to a maximum of 2.12. 10^{-7} Ω. The resulting visualizations are notably clear and precise, accurately reflecting the shape and path of the defects. The use of a 10 kHz frequency ensures a shallow skin depth, optimizing the sensitivity to surface anomalies and enabling high-fidelity imaging that distinctly captures the geometric characteristics of the defects.

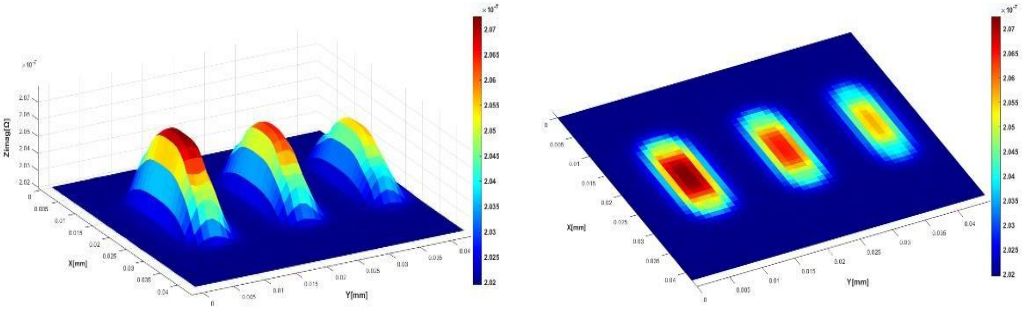

Figure III. 22 .3D illustration of Three Surface Defects Using an Imaginary Part of Impedance

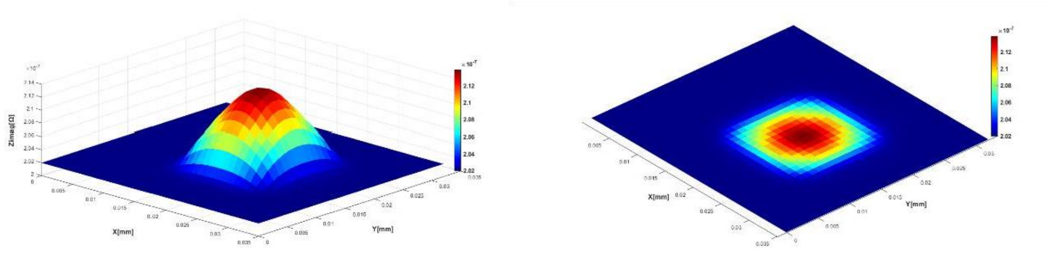

Figure III. 23 . 3D Illustration of Surface Square Defect Using Imaginary Impedance

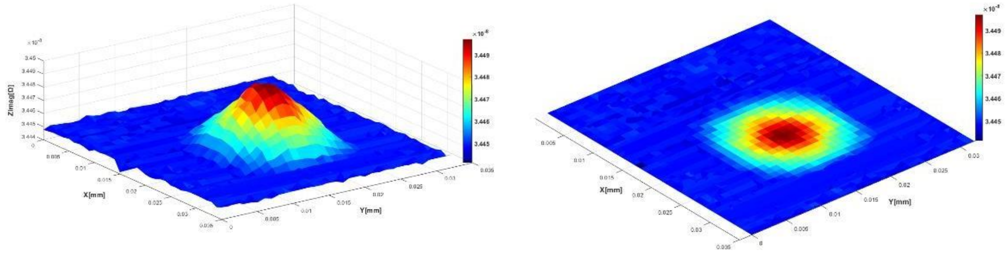

Figure III. 24 . 3D Illustration of Inner Square Defect 0.5mm from Surface Using Imaginary Impedance at Fr 1.6 KHz

In the second scenario, presented in Figures III.24, III.25, and III.26, we focus on internal defects located at depths of 0.5 mm, 1 mm, and 2 mm below the surface, respectively. To maximize the penetration depth of the eddy currents for these deeper flaws, we employed a reduced frequency of 1,600 Hz. At this frequency, the impedance values decrease significantly, with a recorded minimum of 3.45. 10-8 Ω, reflecting the challenges of detecting deeper defects. Furthermore, we observed a progressive decline in imaging quality as the defect depth increased. This degradation can be attributed to the diminishing intensity of eddy currents with increasing distance from the surface, which hampers the ability to fully capture the defect's features at greater depths. The reduced eddy current strength at 2 mm depth highlights a key limitation of eddy current inspection for deep internal defects, as the magnetic field struggles to penetrate sufficiently to provide comprehensive coverage of the defect's geometry. Nevertheless, the ability to image a defect at a depth of 2 mm, even with reduced clarity, underscores the potential of this method and emphasizes the importance of frequency optimization in balancing penetration depth and imaging quality for internal defect detection. These findings illuminate the challenges associated with deeper inspections and the critical need for tailored approaches to enhance detection capabilities in such scenarios.

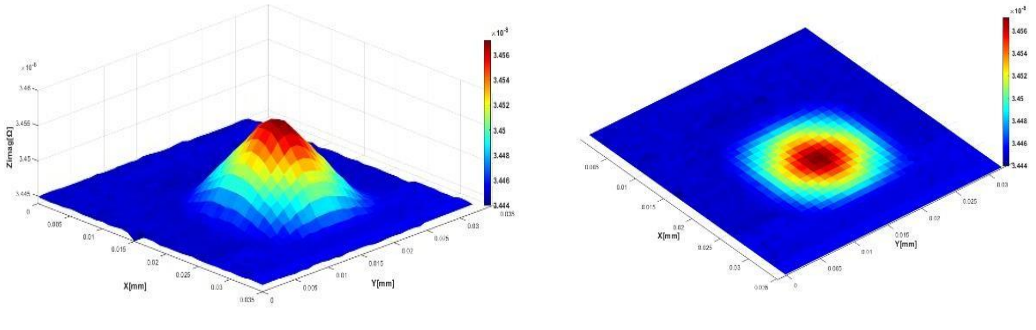

Figure III. 25. 3D Illustration of Inner Square Defect 1mm from Surface Using Imaginary Impedance at Fr 1.6 KHz

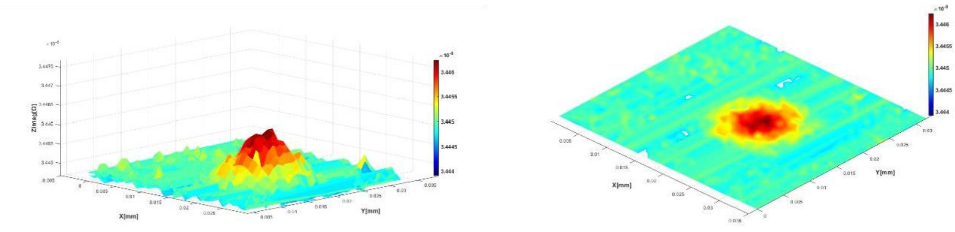

Figure III. 26 . 3D Illustration of Inner Square Defect 2mm from Surface Using Imaginary Impedance at Fr 1.6 KHz

III.5.3. *The third model: eddy current sensor ring for defect imaging in heat exchangers*

This section explores the application of eddy current testing to detect defects in heat exchanger tubes, emphasizing the critical role of tube geometry and material properties in the inspection process. We propose a novel approach using a ring of multiple eddy current sensors, arranged side by side, and operating in harmonic mode with an alternating feed technique to ensure data accuracy and optimize scanning efficiency. The methodology focuses on two models designed to detect both straight and circular defects under varying frequency conditions.

In the first model, illustrated in Figure III.27, a ring of eddy current sensors is positioned inside the heat exchanger tube in a retractable configuration. Operating at a high frequency of 10 kHz, selected to optimize the skin depth for surface sensitivity, the sensors move along the tube's length, aligning with the defects to detect superficial flaws.

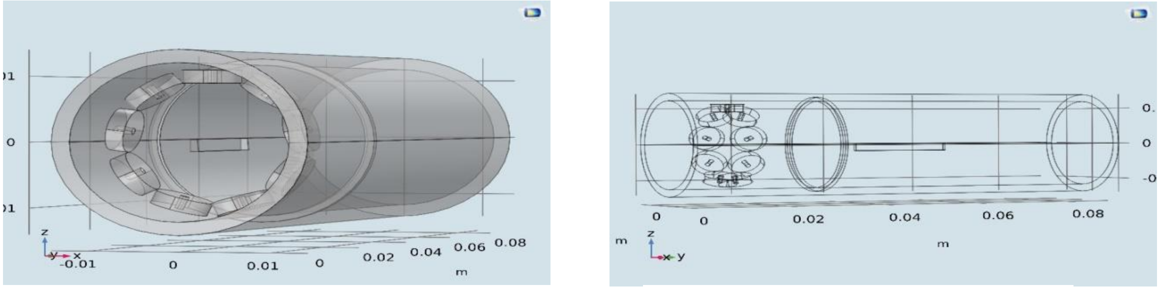

a. 3D profile view

b. 3D front view

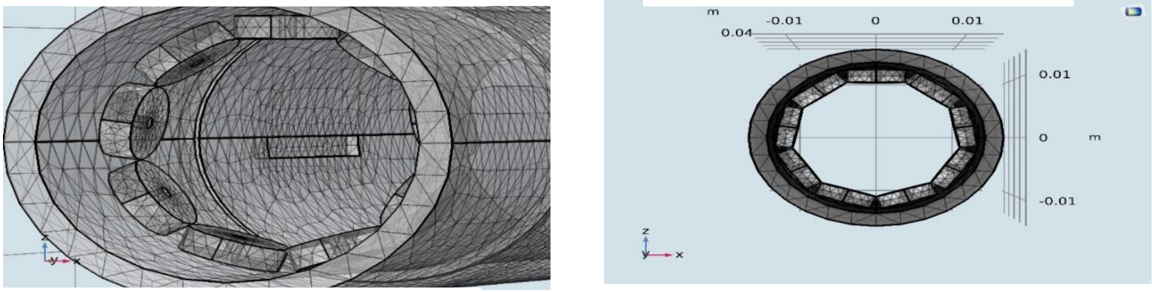

d. Profile mesh view

c. Front view of the mesh

Figure III. 27 Showing the presence of defects in the heat exchanger with the internal distribution of the sensors

The second model, shown in Figure III.28, places the sensor ring externally around the tube and operates at a lower frequency of 1 kHz, chosen to enhance penetration depth and target internal defects.

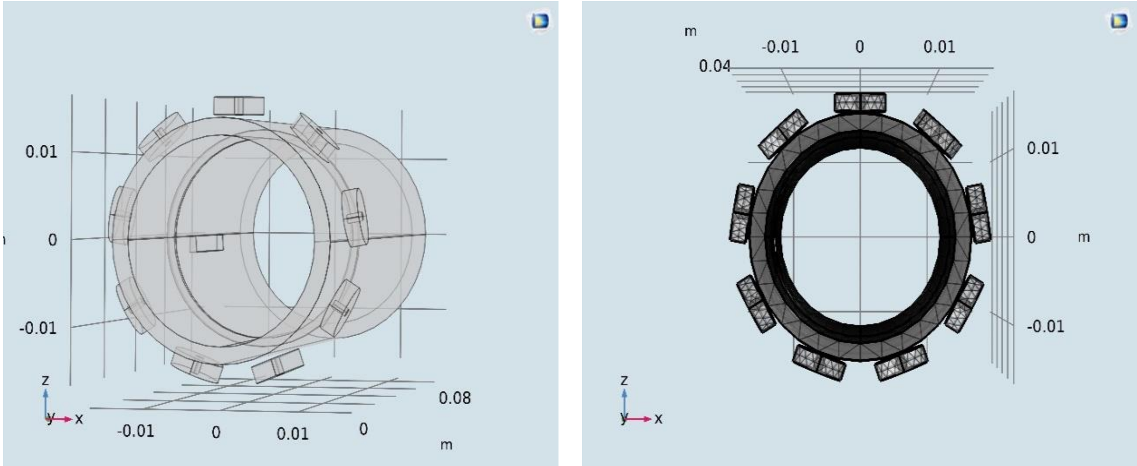

a. 3D profile view   b. Profile mesh view

Figure III. 28 Showing the presence of defects in the heat exchanger with the external distribution of the sensors

During the scanning process, impedance changes in the coils are measured as the sensor ring moves along the tube, and the harmonic components of these signals are analyzed to identify and characterize defects. To further improve the accuracy of defect detection and minimize noise, advanced signal processing techniques are applied, ensuring that the subtle variations in impedance caused by defects are clearly distinguished from background noise. These models provide a robust framework for capturing detailed signals from both surface and internal defects, leveraging the geometry and material properties of the heat exchanger tubes to enhance inspection outcomes, and laying the groundwork for further studies on defect characterization to advance the reliability of heat exchanger maintenance through precise fault detection.

III.5.3.a. Imaging results for surface and internal defects

The imaging results obtained from eddy current testing (ECT) provide valuable insight into the detection and characterization of both surface and internal defects in the heat exchanger tubes. Since the reliability of ECT largely depends on the ability to distinguish between different defect types and depths, analyzing the reconstructed images is essential for validating the effectiveness of the proposed approach. Surface defects are generally associated with stronger impedance variations, producing clearer and more localized imaging responses, while internal defects tend to generate weaker signals that are more challenging to interpret. This distinction highlights the importance of evaluating both cases to assess the robustness of the imaging method under practical conditions. In the following discussion, the results are examined in terms of defect visibility, accuracy of localization, and consistency with expected physical behavior. Particular attention is given to comparing the performance across different excitation frequencies and sensor configurations, as well as assessing the method’s potential for reliable application in industrial heat exchanger inspection.

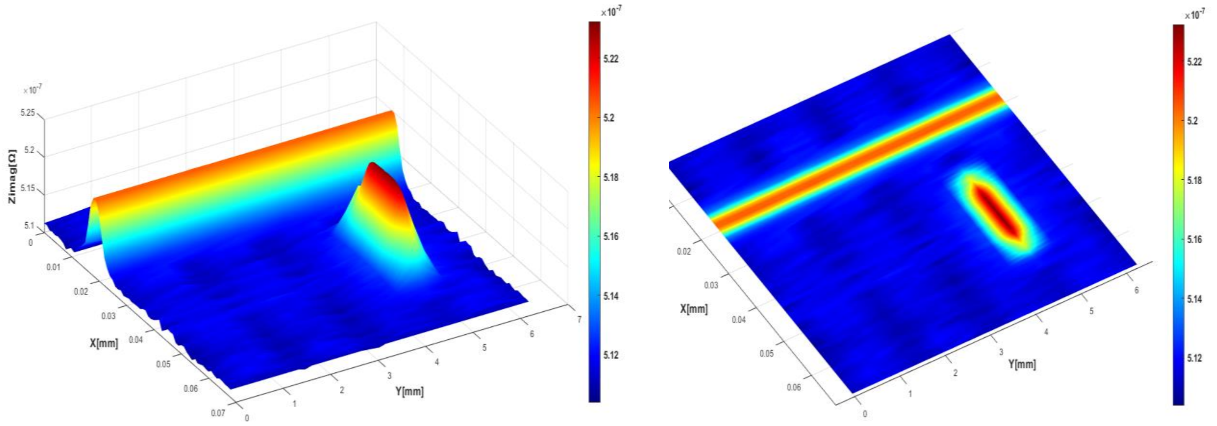

Figure III. 30 . 3D and 2D imaging of the defect in the internal distribution of the sensors

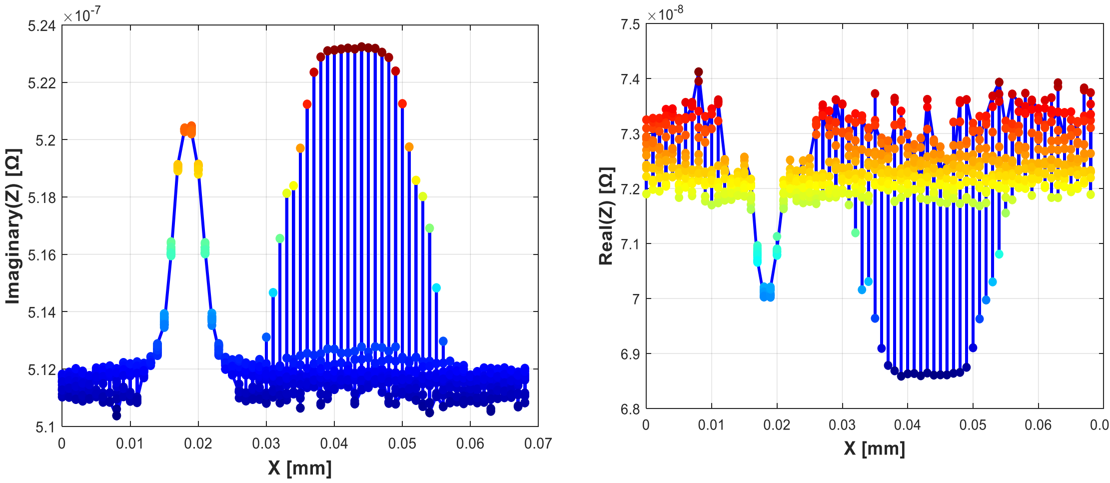

Figure III. 29 Signals of the real and imaginary part of the impedance along the x-axis at the internal distribution of the sensor

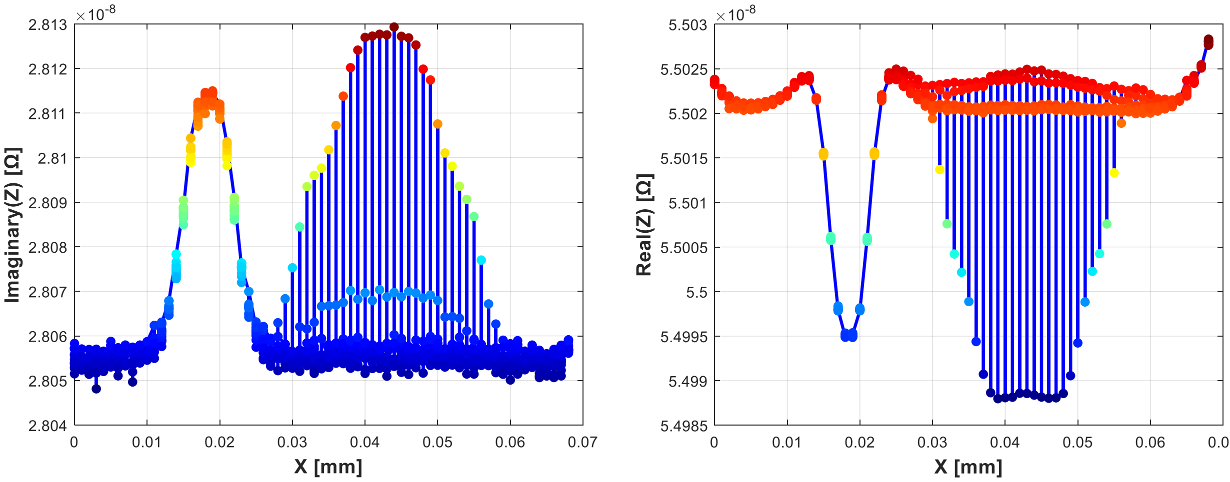

Figure III. 31 Signals of the real and imaginary part of the impedance along the x-axis at the external distribution of the sensors

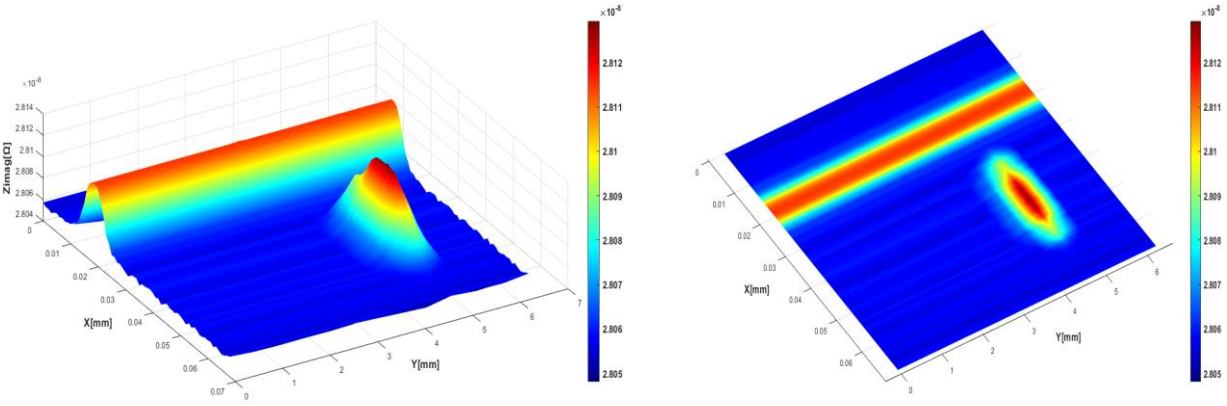

Figure III. 32 . 3D and 2D imaging of the defect at the external distribution of the sensors

III.5.3.b. Results interpretation

In this study, impedance signals were systematically measured at each scanned position along the X-axis of the heat exchanger tube, with the scanning path carefully aligned to the tube holder. Two distinct sensor configurations were employed: the **internal configuration**, where the probe was placed inside the tube, and the **external configuration**, where measurements were taken from outside the tube wall. Figures III.29 and III.30 present the real and imaginary components of the impedance signals obtained in the internal setup, while Figures III.31 and III.32 illustrate the corresponding responses for the external setup.

To transform these raw impedance measurements into meaningful visual representations, the acquired data were aggregated across the complete scanning matrix, which combined both **linear translations along the tube axis** and **rotational movements of the sensor around the circumference**. This approach allowed the reconstruction of detailed two-dimensional (2D) and three-dimensional (3D) images of the defects, thereby enabling a direct visual correlation between the sensor responses and the physical characteristics of the discontinuities. The reconstructed images are displayed in Figure III.30 for the internal configuration and Figure III.32 for the external configuration.

In these figures, each colored point corresponds to a specific impedance value measured along the scanning trajectory. The color scale provides an intuitive mapping of signal variations, where **darker red tones correspond to higher resistance levels**. Regions of increased color intensity are consistently aligned with defect locations, thereby enhancing the contrast between defective and sound areas of the material. This color-coded representation not only improves the clarity and visibility of defect signatures but also facilitates the interpretation of their geometry and extent. Consequently, the reconstructed images serve as a crucial tool for validating the efficiency of the proposed eddy current imaging method in distinguishing between surface and internal defects in heat exchanger tubes.

III.6. *Conclusion*

This chapter has demonstrated the validation of the eddy current testing (ECT) model by first comparing simulation results with experimental measurements obtained from aluminum, austenitic stainless steel, and titanium laminates. The experimental Lissajous curves confirmed the numerical predictions: aluminum exhibited strong, well-distributed eddy currents with highly pronounced defect signatures, austenite produced intermediate yet stable responses, and titanium presented weaker but still detectable signals with appropriate amplification. This agreement between simulation and experiment verified the accuracy of the single-sensor model and established a solid foundation for extending the study to multiplexed sensor arrays.

Building on this validation, the harmonic mode with a sinusoidal excitation was employed in COMSOL® Multiphysics (AC/DC module) to target specific penetration depths across the material surface. By sequentially activating measurement points through a multiplexed method, we minimized mutual inductance and reconstructed high-resolution defect images using a virtual array formed by translating a single absolute coil. This approach enabled precise 2D and 3D defect reconstructions while maintaining the simplicity and sensitivity of the absolute coil configuration.

The simulation results showcased accurate imaging of complex defect geometries, including I-, V-, C-, and zigzag-shaped flaws in plates, as well as straight and circular defects in heat exchanger tubes. The use of color-coded impedance maps enhanced the visibility and interpretability of defect trajectories, while variations in defect size and depth were reflected in induced current density, confirming the sensitivity of the proposed approach. Furthermore, the application of a multi-sensor ring configuration for heat exchanger tubes demonstrated the adaptability of ECT to complex industrial geometries, with both internal and external sensors effectively capturing surface and internal flaws.

While the results underscore the potential of the harmonic mode and multiplexed method for non-destructive testing, challenges remain in detecting deeper internal defects due to reduced eddy current penetration. Future work should expand experimental validation to a wider range of materials and defect types, incorporate advanced signal processing, and explore machine learning approaches such as neural networks to improve defect depth estimation and imaging quality. Overall, this research establishes a validated framework for advancing ECT applications, offering valuable insights into defect detection and characterization that can enhance the reliability and safety of critical industrial components.

Chaptre IV

Solving Inverse Problems in Eddy Current Testing Using Machine Learning and RBF Methods

Chapitre IV. Solving inverse problems in eddy current testing using machine learning and RBF methods

IV.1. *Introduction*

Eddy Current Testing (ECT) is one of the most widely used non-destructive evaluation (NDE) techniques for assessing the integrity of conductive materials. By exploiting electromagnetic induction, it enables the detection of flaws such as cracks, voids, and inclusions without damaging the component under inspection. A key challenge in ECT, however, lies in solving the inverse problem—reconstructing defect characteristics such as size, shape, depth, and orientation from the measured impedance response. This problem is inherently ill-posed and highly non-linear, making traditional approaches, including analytical inversion and iterative optimization, computationally expensive, noise-sensitive, and often limited when applied to complex or irregular defect geometries.

To overcome these challenges, machine learning (ML) methods have emerged as powerful tools, offering data-driven models capable of capturing the complex, non-linear mapping between impedance signals and defect parameters. This chapter provides a focused investigation of ML applications to the ECT inverse problem[88], with particular emphasis on Radial Basis Function (RBF) neural networks. While alternative methods such as Support Vector Machines (SVM)[89], Convolutional Neural Networks (CNN)[90], and other neural architectures have shown promise[91]. The RBF framework is highlighted here for its mathematical simplicity, fast training, and high accuracy[92]. The discussion also considers the role of supervised[93] and unsupervised learning in ECT[94], comparing their advantages and limitations for classification, prediction, and defect characterization.

Building on the methodological framework established in earlier chapters, this work advances the application of ML to NDE by simulating complex three-dimensional random defects in aluminum panels using COMSOL Multiphysics. The multiplexing strategy introduced previously was applied to acquire impedance data, enabling the reconstruction of high-resolution defect images[95]. To complement this imaging process, an RBF neural network was trained to predict defect dimensions directly from the impedance responses. This integrated approach—combining detailed imaging with predictive modeling—enhances detection accuracy and supports near real-time evaluation.

Through this exploration, Chapter 4 demonstrates (Figure IV.1) how machine learning, and in particular the RBF method, can significantly improve the solution of inverse problems in ECT. The results underline the potential of intelligent NDE approaches to provide more accurate, efficient, and reliable defect characterization, thereby contributing to safer operation and maintenance of critical infrastructures such as aerospace structures, nuclear reactors, and heat exchangers.

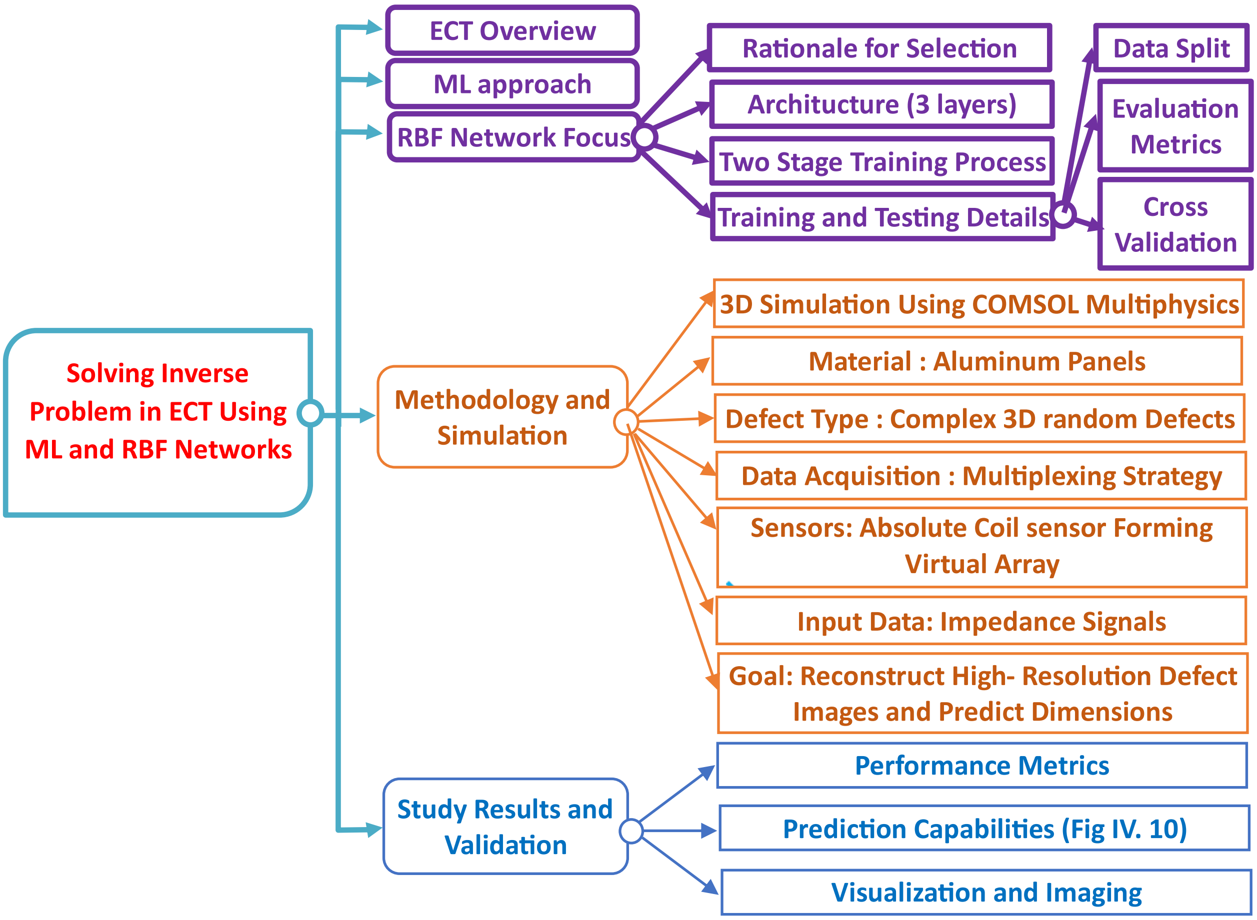

Figure IV. 1 Methodology for Solving Inverse Problems in ECT using Machine Learning and RBF Networks

IV.2. *Proposed model*

Building on the 3D simulation approach from the previous chapter, we first design the aluminum panels using COMSOL Multiphysics [85], and then create a random defect to be studied. The defect is characterized by a straight, discontinuous path that gradually narrows from 2 mm to 1.5 mm,0.75mm, and finally 0.5 mm. In addition, straight branches of 10 mm in length and 0.5 mm width extend from the main path (Figure IV.2)

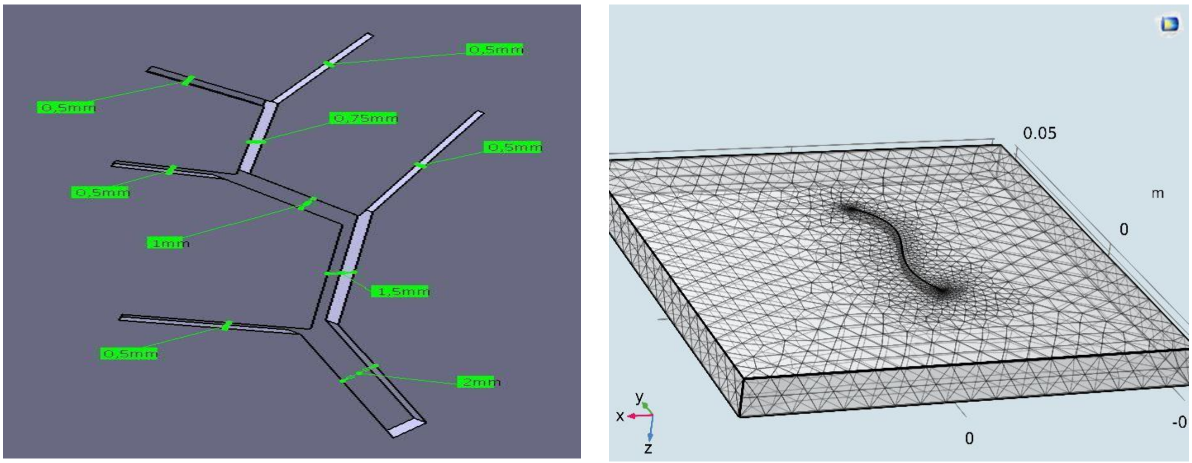

Figure IV. 2 Mesh model of a random defect with refracted straight branches and varying widths

IV.2.1. *Evaluating and discussing study results*

IV.2.1.a. Distribution of eddy currents

As illustrated in Figure IV.3, the eddy current density distribution generated by a random defect with straight branches is presented

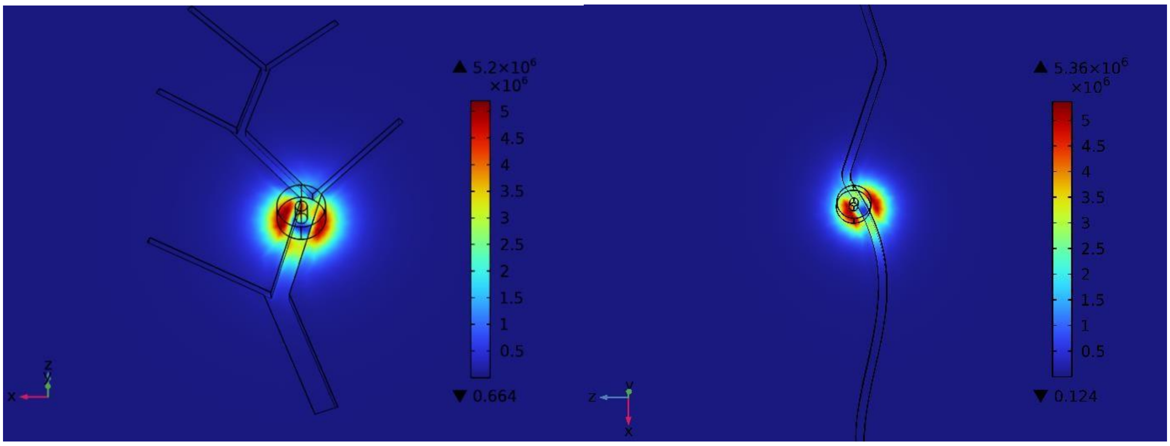

Figure IV. 3 Eddy Current distribution of a random defect

. The simulation was performed under the same initial conditions: a 10 kHz excitation frequency and a 0.5 mm lift-off distance between the sensor and the plate. The resulting images offer valuable insights into the coil's interaction with the material at this frequency, allowing for the calculation of impedance as a function of the coil's position.

IV.2.1.b. Collect impedance signals and display the shapes of defect paths

In this section, the focus is placed on presenting and analyzing the impedance signals obtained from the eddy current testing simulations, with particular attention given to their imaginary components. These signals are examined along both the X and Y axes, allowing for a detailed evaluation of how spatial variations in the scanning path influence the sensor response. By emphasizing the imaginary part, which is highly sensitive to variations in defect depth and geometry, the results provide meaningful insight into the behavior of the electromagnetic field and its interaction with both surface and subsurface discontinuities, Figure IV.4

In line with the methodology outlined in Chapter III for interpreting results, the Figure IV.4 presented above illustrate the outcomes for a random defect featuring straight branches. The colored segments depict the impedance signals along the defect paths, mapped across the x- and y-axes. This analysis yields a three-dimensional visualization at an orientation of (60°, 60°) and a two-dimensional projection viewed vertically at (0°, 90°). The color intensity, which transitions toward a darker red in points, lines, or surfaces, signifies higher impedance values. This visualization approach delivers clear and detailed representations of the shape and trajectory of random defects, particularly highlighting their paths with precision.

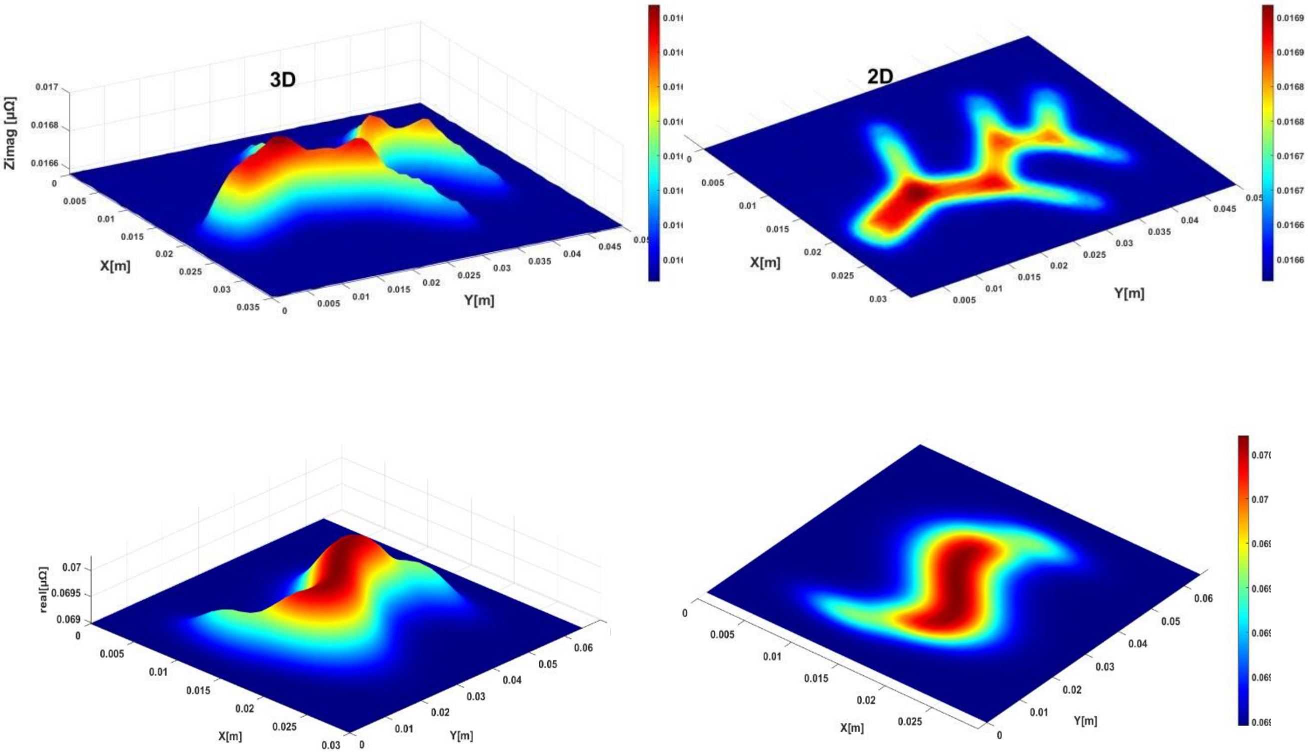

Figure IV. 4 .3D and 2D imaging of random defects via impedance imaginary values

IV.2.1.c. The inverse problem via machine learning techniques

The inverse problem in ECT involves determining defect properties from impedance signals, which are influenced by defect geometry, material properties (conductivity, permeability), sensor configuration, and excitation frequency. In this research, we apply harmonic mode ECT with the multiplexed method, using an absolute coil sensor to form a virtual array through movement, as detailed in previous chapters. The impedance data collected from aluminium plates and copper heat exchanger tubes serve as the input for solving the inverse problem, aiming to reconstruct defect profiles with high precision. Machine learning methods provide a powerful framework for this task, learning the complex mapping between impedance signals and defect parameters from training data. This chapter explores NN, SVM, CNN, and RBF methods, with a focus on the RBF method used in this study, incorporating findings from prior research to illustrate the practical application of RBF networks in ECT. The objective is to characterize surface and internal defects in terms of size, shape, and depth, enhancing the reliability of material inspection in industrial settings.

IV.3. *The inverse problem in eddy current testing: a brief overview*

The inverse problem in ECT seeks to infer defect characteristics from measured impedance signals. The forward problem can be expressed as:

$$Z = f(d, m, s) \qquad \text{(VI.1)}$$

Where:

Z represents the impedance signal (real and imaginary parts),

d includes defect parameters (length, width, depth),

m denotes material properties (conductivity σ, permeability μ, and s encompasses sensor and excitation parameters (frequency, coil dimensions).

The inverse problem aims to determine d:

$$d = f^{-1}(Z, m, s) \qquad \text{(VI.2)}$$

This inversion is inherently non-linear and ill-posed, as multiple defect configurations may produce similar impedance signals, and small measurement noise can lead to significant errors in reconstruction. Traditional methods, such as gradient-based optimization or least-squares fitting, often require iterative simulations of the forward problem, which are computationally expensive and sensitive to initial guesses and noise. Machine learning methods offer a data-driven alternative, learning the inverse mapping directly from training data, thereby providing a more efficient and robust solution for defect characterization in ECT.

IV.3.1. *Types of machine learning and utilization in ECT*

IV.3.1.a. Supervised learning in ECT: prediction and classification

Supervised learning in Eddy Current Testing (ECT) can be divided into two core tasks: **prediction (regression)** and **classification**.

- **Prediction (Regression):** The central objective of this research, prediction involves estimating continuous defect parameters—such as length, width, and depth—from impedance signals. Methods such as Neural Networks (NN), Support Vector Regression (SVR), Convolutional Neural Networks (CNN), Radial Basis Function (RBF) networks, and Gaussian Process Regression (GPR)[96] are all used to model these non-linear relationships. While NNs and CNNs can capture highly complex mappings, they require large datasets and computational resources. SVR[97] is robust to noise and effective with limited data[98],[99]while RBF networks stand out for their efficiency in function approximation with lower data requirements. GPR further complements these methods by providing both accurate predictions and uncertainty quantification, a critical advantage in safety-critical applications.

- **Classification:** Classification assigns impedance signals to discrete categories, such as differentiating between cracks, voids, inclusions, or identifying defective vs. non-defective regions. SVMs excel in this role due to their margin maximization principle, while CNNs are particularly powerful for spatial classification tasks using impedance maps (C-scans). NNs also perform well in multi-class problems, [100]. RBF networks can be adapted for classification, though they are more effective in regression tasks.

IV.3.1.b. Unsupervised learning as a complementary tool

Although the focus of this study is supervised prediction, unsupervised learning plays a supportive role in enhancing data preprocessing and model efficiency. For instance, in RBF networks, k-means clustering is applied to determine the centers before supervised training, [101].

Similarly, dimensionality reduction methods such as PCA can streamline impedance data, improving the performance of NNs, SVMs, and CNNs. Unsupervised clustering can also be applied directly for anomaly detection, grouping impedance responses to flag potential defects without prior labeling. These techniques serve as valuable complements to supervised methods, ensuring more robust and efficient defect characterization in ECT.

IV.3.1.c. Interplay between regression methods

A comparative overview of the different regression methods and their interactions is presented in Table IV-1, which summarizes their main characteristics, advantages, and limitations in the context of this study.

Criteria	CNN (Convolutional Neural Network)	SVR (Support Vector Regression)	GPR (Gaussian Process Regression)
Architecture	Deep with convolutional layers; very complex	Kernel-based regression	Probabilistic, kernel-based
Training Demand	Very high; backpropagation with heavy computation	Moderate; convex optimization	High; requires inversion of the covariance matrix
Non-linearity & Noise	Strong non-linear modelling; needs regularization	Robust to noise; effective with kernels	Handles non-linearity well; sensitive to kernel choice
Data Requirements	Very large datasets needed	Small to medium datasets	Small to medium datasets (scales poorly with large data)
Interpretability	Low ("black box")	Medium (support vectors visible)	Higher (provides uncertainty estimates)
ECT Application Focus	Imaging and regression of defect size/depth	Defect depth and size prediction	Defect depth prediction with uncertainty quantification

Table IV. 1 Comparison of Regression Methods in Eddy Current Testing

In Eddy Current Testing (ECT), regression methods are primarily used to predict defect characteristics such as depth, size, or shape from impedance data. Among them, Convolutional Neural Networks (CNNs) provide powerful feature extraction for complex data but require very large datasets and high computational resources. Support Vector Regression (SVR) is effective for smaller to medium datasets, offering good robustness against noise. Gaussian Process Regression (GPR) provides probabilistic predictions with confidence intervals, making it useful when quantifying prediction uncertainty is important, though it can be computationally expensive for large datasets. Each method has unique advantages, and the choice depends on data size, noise level, and prediction requirements.

IV.4. *Why the RBF NN method was chosen for this research in ECT*

The choice of the Radial Basis Function (RBF) method for this research in ECT testing was motivated by its balance of accuracy, efficiency, and suitability for solving inverse problems. Unlike multilayer perceptrons (MLPs) or convolutional neural networks (CNNs), which require large datasets, long training times, and extensive parameter tuning, RBF networks train quickly using clustering and least-squares optimization while still modeling the nonlinear relationship between impedance signals and defects with high accuracy. Compared to support vector machines (SVM/SVR), which rely on computationally intensive quadratic optimization and sensitive kernel choices, RBF offers faster training and easier tuning. Similarly, while Gaussian Process Regression (GPR) provides high accuracy and uncertainty estimation, its poor scalability with dataset size makes it impractical for real-time ECT, whereas RBF scales efficiently. The localized Gaussian functions of RBF make it robust to noise caused by lift-off, material inhomogeneity, or temperature variations, ensuring reliable predictions. RBF networks also require less data than deep models, making them effective when only moderate simulated or experimental datasets are available. Their simple and interpretable architecture allows easy implementation, with centers representing prototype impedance signals—valuable for understanding defect characteristics. Prior studies have validated their success in ECT defect prediction, and their efficiency aligns well with harmonic mode ECT requirements, where multiple frequencies are used to assess both surface and subsurface defects. Overall, RBF networks provide an effective, interpretable, and computationally efficient solution for ECT applications compared to SVM, SVR, GPR, CNN, and ML.

IV.4.1. *Radial basis function neural networks for defect detection in ECT*

The radial basis function (RBF) network is an artificial neural network primarily used for function approximation, classification, and regression tasks. It is particularly well-suited for problems involving complex and nonlinear relationships between inputs and outputs.

IV.4.1.a. General overview of RBF networks

The radial basis function (RBF) neural network [102], introduced by Broomhead and Lowe 1988, is built on the principles of conventional approximation theory. It is a highly adaptable architecture, well-suited for modeling complex relationships between input and output data. The network comprises three primary layers: the input layer, a hidden layer consisting of neurons that apply Gaussian non-linear activation functions, and the output layer, [103].

An RBF network typically consists of three layers:

Input layer: This layer directly transmits the input data to the hidden layer. It receives impedance values at each state, consisting of both real and imaginary components. These two inputs, derived from the sensor readings at different positions during the sheet inspection, provide essential information for analysis.

Hidden layer: it comprises nodes associated with a radial basis function (commonly a Gaussian function). These functions compute the distance between the input data and a predefined center. The output of each node is a nonlinear transformation of the input data, which allows the network to model complex relationships. The equation for a Gaussian radial basis function is given below:

$$y(x) = \sum_{i=1}^{N} w_i \emptyset_i(x) \quad \text{(VI.3)}$$

x is the input vector. The center of the radial basis function is denoted as c. The c parameter σ controls the spread of the function

$$\emptyset(\mathrm{x}) = \exp\left(-\frac{\|\mathrm{x}-\mathrm{c}\|^2}{2\sigma^2}\right) \quad \text{(VI.4)}$$

Output layer: This layer combines the outputs from the hidden layer to produce the final prediction. The output is typically a weighted sum of the hidden layer outputs for regression tasks. The relationship between the output Y and the hidden layer outputs can be expressed as:

N is the number of hidden neurons. The weights associated with each hidden node are denoted asw_i. The outputs of the hidden nodes are represented as $\emptyset(\mathrm{x})$.

In the RBF neural network, c_k and σ_k represent the center and spread of the radial basis function $h_k(x)$, respectively. A key feature of the RBF-NN is the distinction between the first and second layers, which results in a two-stage training process. In the first stage, the input data is used to determine the parameters that govern the basis function, specifically the centers c_k and spreads σ_k. This allows the network to define the location and width of each basis function, which are crucial for capturing the underlying patterns in the data.

Let y represent the real rate of penetration (real data), $\hat{y}$ denote the predicted data, and n the number of data points corresponding to either the training dataset for a specific formation.

Each dataset is randomly partitioned into two subsets: training and testing. The training dataset must be sufficiently large to capture the variability in the data, but not so large as to risk overfitting the model. The optimal split ratio varies based on several factors, but a typical guideline for the training-testing split is 60 to 80% for training data and 20 to 40% for test data. In this study, 70% for training and 30% for testing.

IV.4.1.b. Training process

The training process of the radial basis function (RBF) neural network for defect detection and prediction in conductive materials follows these key steps:

- Data collection: Eddy current testing (ECT) data is collected and randomly split into 70% for training and 30% for testing.
- Network architecture: An important step is determining the optimal number of neurons, since this parameter directly affects the generalization ability of the network and its computational time. A trial-and-error strategy was adopted in this work because it provides a good balance between exploration efficiency and computational cost, [104].
- Basis function parameters: This step, also known as unsupervised training, where the centers and spread of the basis function are selected based on the acquired data sets using k-means clustering and the k-nearest neighbors techniques, respectively.
- Cost function minimization: This step, also known as supervised training, where the network is trained by adjusting and updating weights based on the actual output of the network compared to the data. This step is crucial and requires a decent optimization algorithm; here, a genetic algorithm was implemented to minimize the error effectively, [105].

IV.4.1.c. *Testing process*

The developed model is tested on unseen data to evaluate its generalization capability as illustrated in Figure IV.5. Its performance is assessed using various evaluation metrics, including the root mean square error (RMSE) and the coefficient of determination. These metrics provide a quantitative measure of the model's accuracy and ability to predict new, unseen data.

$$R^2 = 1 - \frac{\sum_{i=1}^{N}(y_{testi}-\hat{y}_{testi})^2}{\sum_{i=1}^{N}(y_{testi}-\bar{\bar{y}}_{testi})^2} \qquad \text{(VI.5)}$$

Where:

- y_{testi} actual values
- $\hat{y}_{testi}$ predicted values
- $\bar{\bar{y}}_{testi}$ mean of actual values
- N number of data points

$$RMSE = \sqrt{\frac{1}{n}\sum_{i=1}^{N}(y_{testi}-\hat{y}_{testi})^2} \qquad \text{(VI.6)}$$

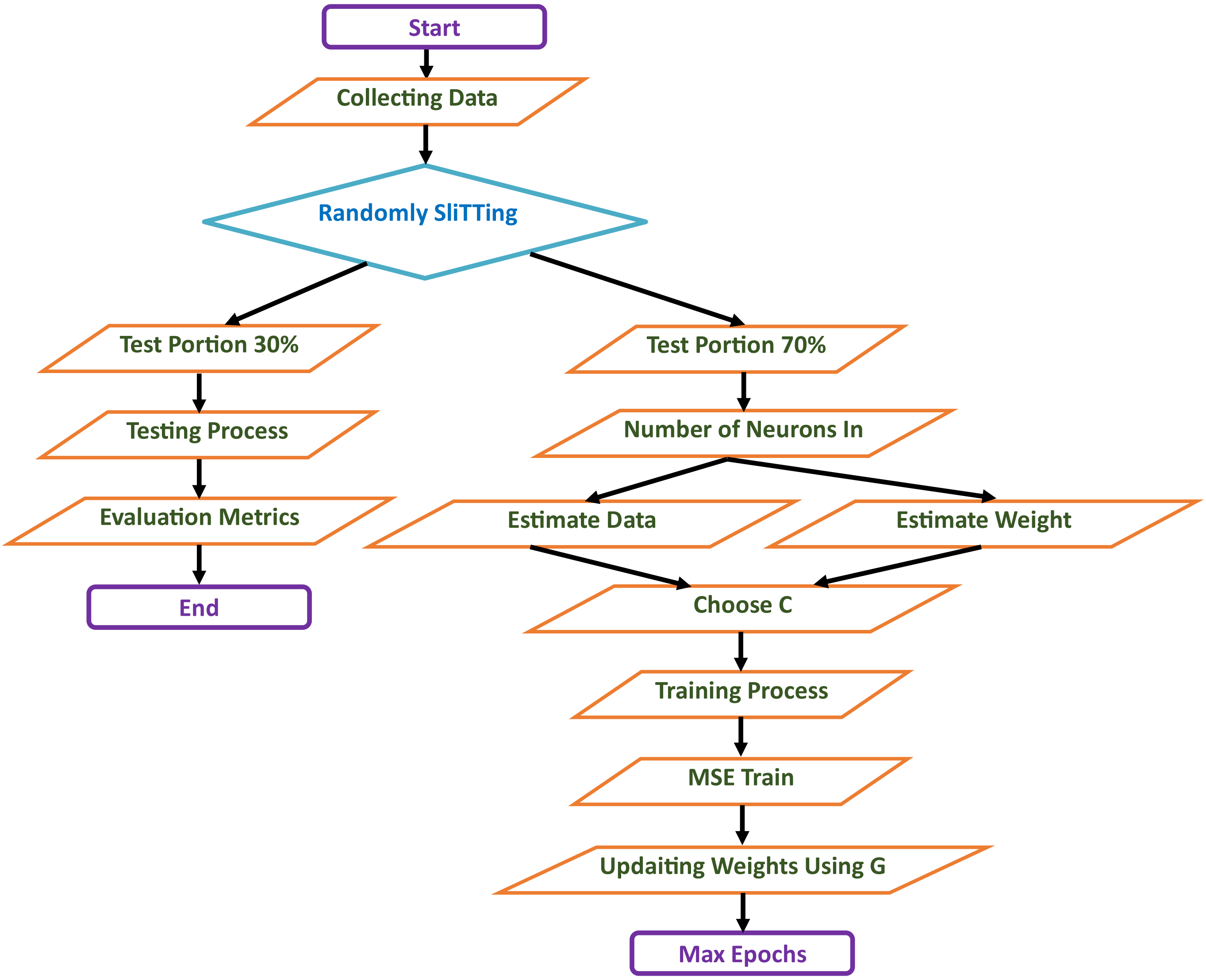

Figure IV. 5 Correlation between predicted and actual defect dimension using RBF network

Utility of RBF networks: The inherent non-linearity in the relationship between defect dimensions and their paths makes the RBF network a highly suitable tool for this application.

Its ability to generalize from a small dataset and model complex dependencies ensures reliable predictions, making it an effective choice for tasks involving defect path prediction in aluminum sheets.

This study's radial basis function (RBF) network predicts the path of defects in aluminum sheets by analyzing their detected dimensions (length and width). The revised process is outlined as follows:

Input data: The input to the RBF neural network consists of the geometric dimensions (width and depth) of detected defects, obtained from preliminary inspection data. These dimensions represent the basic shape characteristics identified during the initial analysis phase.

In the first training stage, the network is fed with data from eight separate inspections of a test panel. Each inspection involves a single defect with a fixed length of 15 mm but varying widths and depths between 0.5 mm and 2 mm. For each inspection, impedance measurements (real and imaginary components) are recorded at 682 different sensor positions distributed across areas far from the defect, near the defect, and directly over the defect. This results in a total of 5,456 impedance data points used to train the network.

In the second training stage, 45 additional inspections are carried out. Each inspection involves 24 impedance scans along a straight-line defect, with depth values ranging incrementally from 0 mm to 4.5 mm (0, 0.1, 0.2, ..., 4.5 mm). This produces a total of 1,080 additional input samples for depth-based training. Together, these two stages provide the RBF network with a rich dataset, allowing it to effectively learn complex nonlinear relationships and accurately model defect shapes and propagation paths.

Post-Training Prediction: After training, the RBF network is capable of predicting the overall trajectory of the defect based on the input width–depth dimensions. These predictions offer valuable insights into the defect’s location and potential progression, allowing for a more precise evaluation of its shape and extent.

IV.4.1.d. Cross-validated RBF networks

Cross-validation (Figure IV.6) is a vital method for assessing the reliability and generalization of radial basis function (RBF) neural networks in defect detection and prediction using eddy current testing (ECT) data[106]. Rather than depending on a single train-test split, the dataset is divided into k subsets, or folds. The model is trained on (k–1) folds and validated on the remaining fold, with this process repeated until each fold has been used for validation. The average performance across all iterations is then calculated. This approach maximizes the use of limited or costly ECT data by ensuring all samples contribute to both training and testing. In this study, a 5-fold cross-validation strategy was employed, striking a balance between computational efficiency and robust evaluation. This method provides a reliable estimate of the RBF network’s ability to predict defect depth and propagation across diverse operating conditions and material properties.

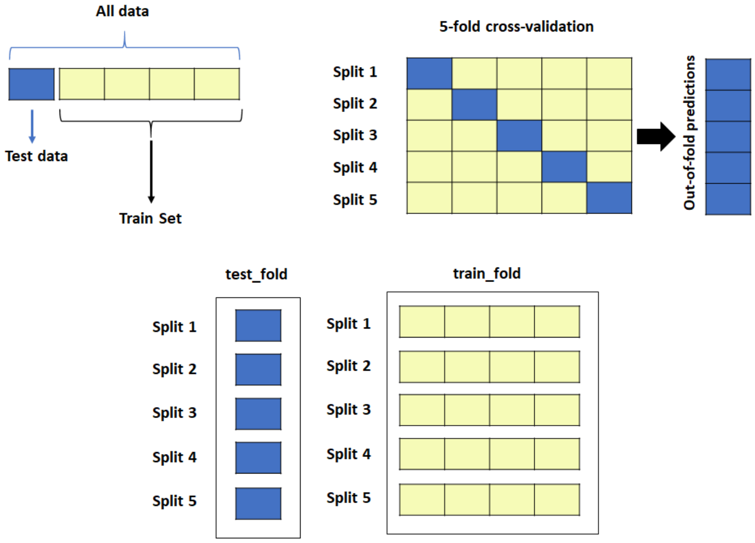

Figure IV. 6 Illustration of the cross-validation method

IV.4.1.e. Evaluation and Discussion – Part 2

This enhanced workflow demonstrated the effectiveness of the RBF algorithm in analyzing defect characteristics and predicting their behavior based on dimensional input data. The network's performance was assessed using both training and test datasets, yielding correlation coefficients of R_{train}=0.95518 and R_{test}=0.94849. In the first scenario, which focused on predicting the defect’s shape and trajectory using width data, the results were even more promising, with R_{train}=0.96808 and R_{test}=0.96392. These high and closely matched values indicate a strong correlation between the predicted and actual defect characteristics, confirming the model’s predictive accuracy, as illustrated in Figures IV.7 and IV.8.

Furthermore, the mean squared error (MSE) and normalized mean squared error (nMSE) were calculated to quantify the average squared deviation between predicted and true values. The low MSE values reinforce the model’s reliability and precision in accurately mapping defect trajectories based on impedance measurements.

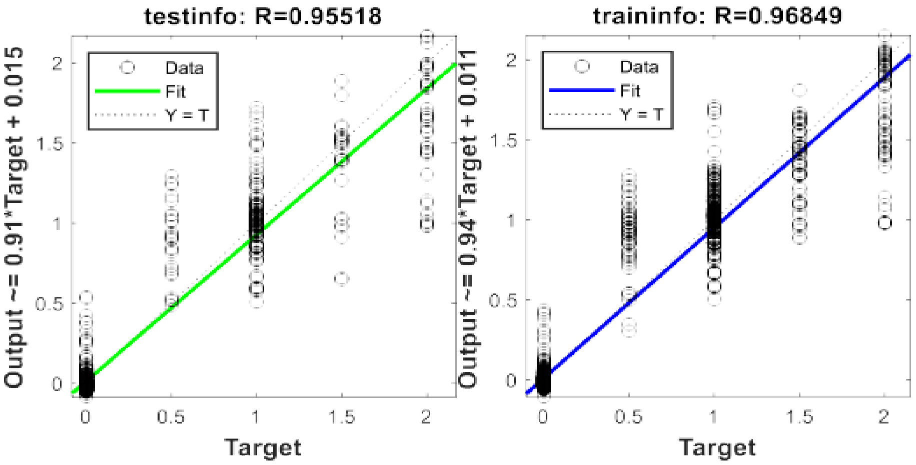

Figure IV. 7 RBF model workflow with a dataset containing different defect widths

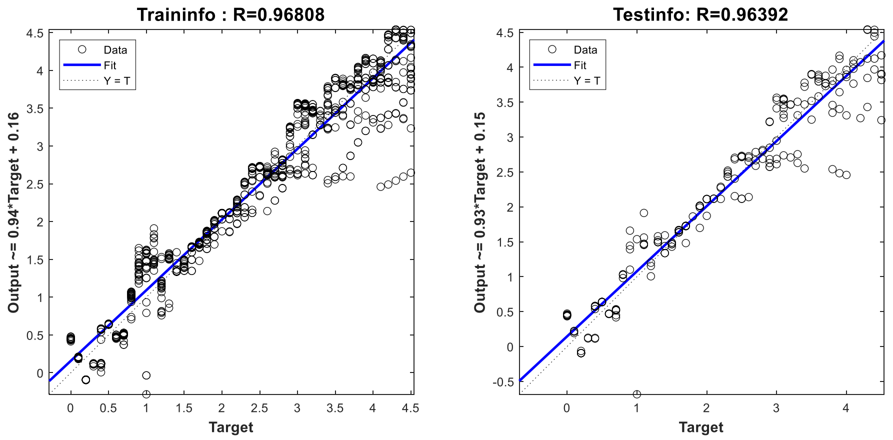

Figure IV. 8 RBF model workflow with a dataset containing different defect depths

As shown in Figure IV.9, a 5-fold cross-validation (CV) analysis was employed to ensure that the radial basis function (RBF) neural network framework generalizes beyond synthetic data and avoids overfitting

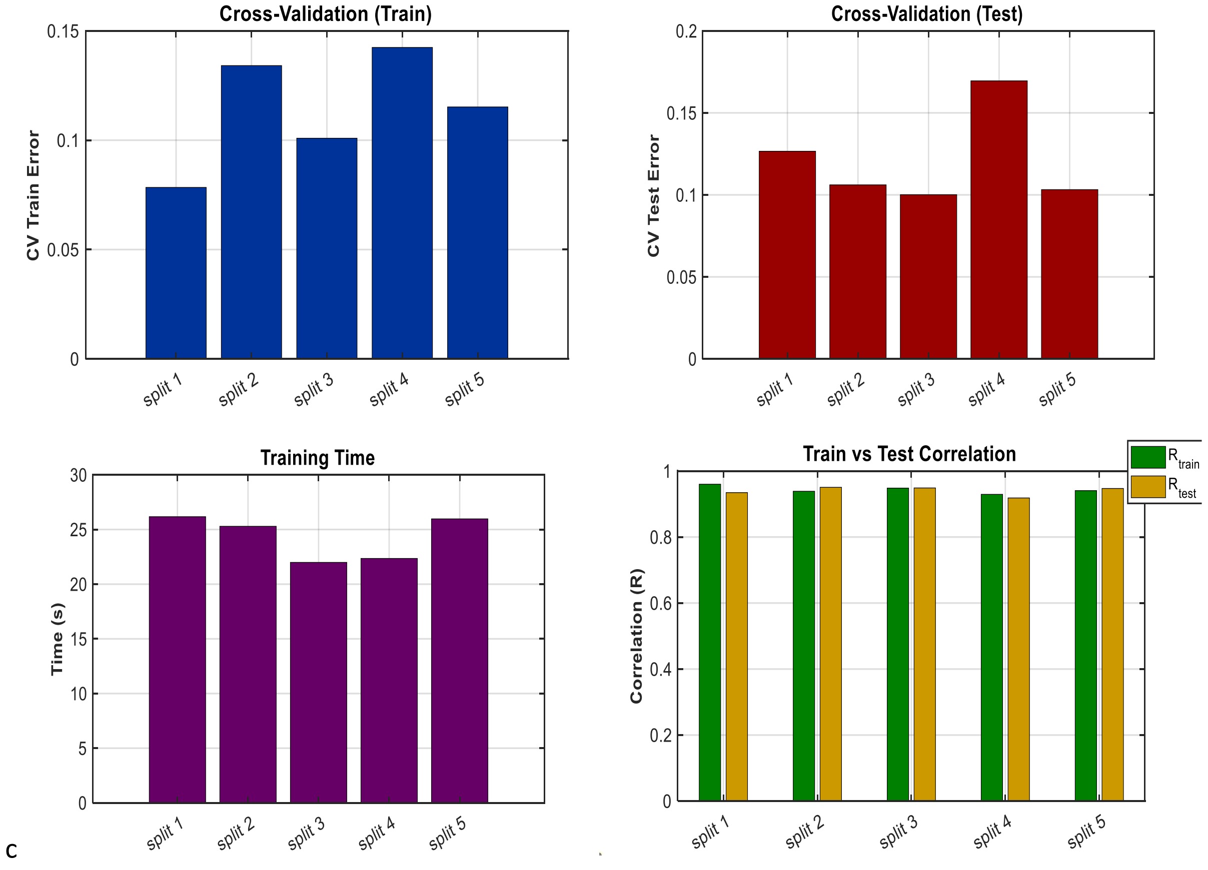

Figure IV. 9 Training Efficiency and Cross-Validation Performance

. The dataset was partitioned into training and testing subsets. Performance was evaluated using CV training (CV_tr) and testing (CV_ts) errors, correlation coefficients ($R_{train} \approx 0.93$–0.96, $R_{test} \approx 0.92$–0.95), and computational times. The consistently high correlations, low variance across folds, and small gap between CV_tr and CV_ts confirm robust generalization compared to single train–test splits. The choice of the RBF model is justified by its stability, accuracy with modest data, and faster training compared to more complex models such as convolutional neural networks (CNNs) or Gaussian process regression (GPR). Hyperparameters were empirically set to balance accuracy and speed, with future work directed toward systematic optimization. In terms of feasibility, training required approximately 22–26 seconds per fold, enabling near real-time defect detection and supporting potential industrial deployment. Finally, variability observed across folds reflects the diversity of defect scenarios, yet the narrow error range highlights the model's reliability and predictive strength.

. Figure 10 illustrates a process summary for characterizing defects in eddy current testing (ECT) using a radial basis function neural network (RBF-NN). Multiple sensor arrays, controlled by multiplexing, collect impedance data (both real and imaginary parts) from different locations on the tested material. These impedance values serve as input features for the RBF-NN, where neurons process the data to learn patterns associated with defects.

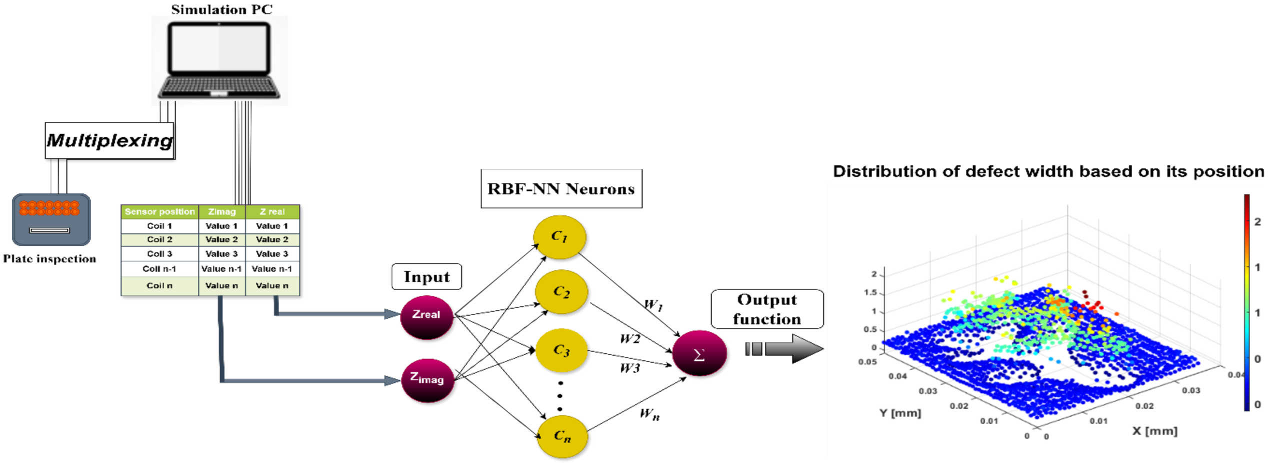

Sensor position	Zimag	Z real
Coil 1	Value 1	Value 1
Coil 2	Value 2	Value 2
Coil 3	Value 3	Value 3
Coil n-1	Value n-1	Value n-1
Coil n	Value n	Value n

Figure IV. 10 Defect Characterization in Eddy Current Testing Using Radial Basis Function Neural Networks

The network's output function aggregates the results, generating a three-dimensional spatial defect map, where a blue color distribution represents the absence of clear areas in the plate and distant from the defect, while a darker (red and orange) distribution represents the presence of the largest possible defect size. This approach promotes automated and accurate defect detection in non-destructive testing (NDT) applications.

The performance of the radial basis function (RBF) algorithm, pre-trained on two distinct datasets (Figure IV.8), was evaluated using impedance-based imaging of two types of randomly generated defects. The imaging results, presented in Figures IV.3 and IV.4, provide the first validation of the model's ability to differentiate and characterize variations in the impedance response caused by defect presence and geometry. This step establishes a foundation for assessing whether the network can effectively generalize across different defect morphologies.

In the second phase of the study, the predictive capability of the RBF network was tested by reconstructing the geometric dimensions of the defects, as shown in Figure IV.11. Figures IV.11a and IV.11b illustrate the predicted shapes of random defects 1 and 2 along their propagation paths. The reconstructed defect widths are encoded using a color gradient, where dark blue represents regions free of defects (0 mm), and dark red highlights the maximum defect width (2 mm). Intermediate values are represented by orange (≈1.5 mm), yellow (0.75–1 mm), and light blue (≈0.5 mm), enabling a fine-grained visualization of defect severity. The close correspondence between predicted and expected defect geometry confirms that the network successfully captures localized impedance variations and translates them into quantitative structural information.

Beyond width estimation, Figures IV.11c and IV.11d demonstrate the RBF algorithm's ability to predict defect depth trajectories with high accuracy. The reconstructed profiles reveal maximum depths of approximately 2 mm, consistently highlighted in dark red, while shallower defect regions are represented by intermediate colors. This depth mapping is especially significant for non-destructive evaluation, as subsurface propagation often determines the criticality of structural degradation. The ability of the RBF network to track both shallow and deeper regions of the defect underlines its robustness in handling heterogeneous defect patterns.

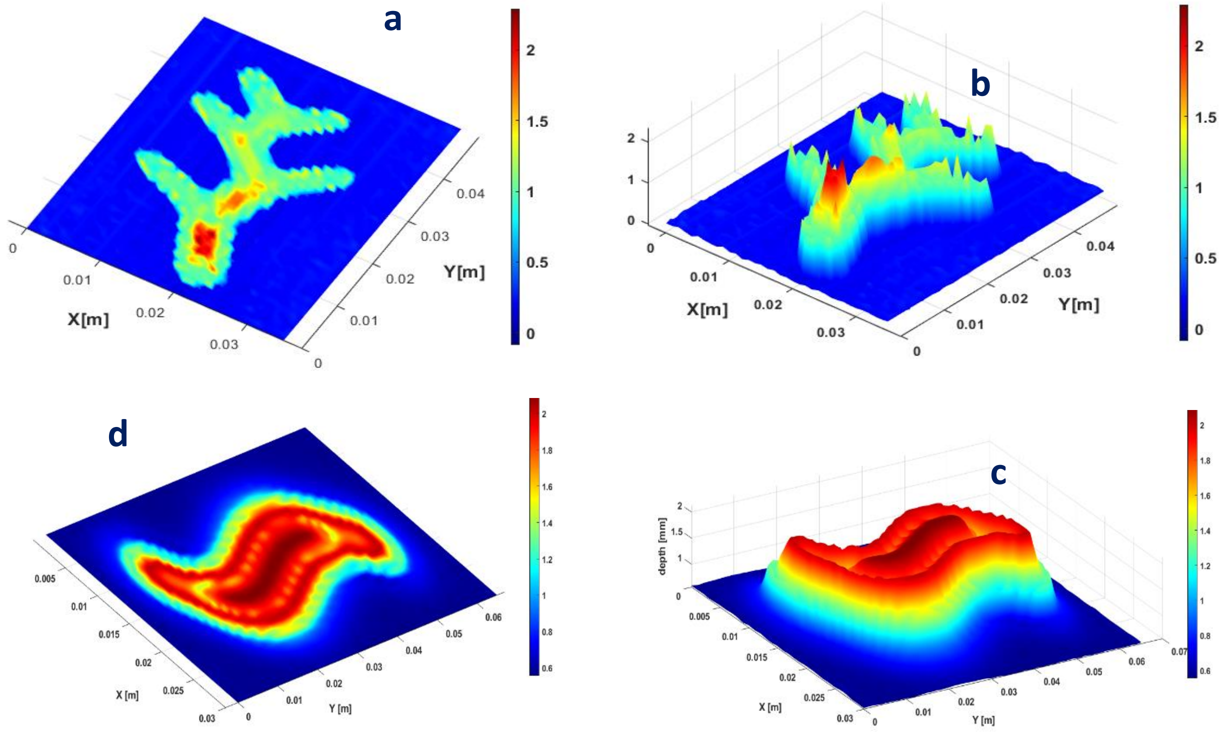

Figure IV. 11 Reconstructed path and width distribution of random defect 2 using the trained RBF algorithm

Taken together, these results confirm that the proposed framework is not only capable of detecting the presence of defects but also of reconstructing their geometry with sufficient resolution to distinguish variations in both width and depth. The multi-level visualization underscores the practical value of the approach for monitoring defect evolution over time, which is crucial in applications such as predictive maintenance. Furthermore, the stability of the predictions across both datasets reinforces the claim that the RBF algorithm generalizes effectively and can be applied to different defect types without extensive retraining. In summary, the extended set of results highlights the strong predictive power of the RBF network in terms of accuracy, robustness, and practical interpretability, strengthening its relevance for industrial non-destructive testing scenarios.

IV.5. *Conclusion*

In this chapter, a modeling framework was developed for the detection and characterization of random defects in aluminum sheets, with particular emphasis on irregular defect trajectories and variable geometric dimensions. A multiplexing strategy was implemented at a fixed frequency to minimize mutual inductance within the sensor array, enabling accurate detection and high-resolution reconstruction of defect geometries. The structured impedance responses, aligned with the scanning path, provided a reliable foundation for capturing intricate flaw patterns.

To enhance analysis and prediction, a Radial Basis Function (RBF) neural network was trained on the impedance data to estimate defect dimensions. The use of 5-fold cross-validation demonstrated strong generalization capability, with high correlation coefficients and low error variance across folds, confirming the robustness of the approach while avoiding overfitting. Compared with more computationally intensive techniques such as convolutional neural networks (CNNs) or Gaussian process regression (GPR), the RBF framework achieved a favorable balance between training speed and predictive accuracy. When applied to randomly shaped defects, the network successfully reconstructed both width and depth variations, as illustrated in Figure IV.10, thereby validating its potential for near real-time non-destructive evaluation.

The integration of multiplexed sensing with RBF-based modeling provides a practical, computationally efficient, and reliable solution for defect detection and imaging. This chapter should be regarded as a preparatory step toward more advanced applications. Future work will aim to further refine imaging precision, extend the framework to three-dimensional defect profiling, and incorporate the methodology into real-world inspection systems. By confirming the reliability and practicality of the proposed approach, this study establishes a solid foundation for future research in intelligent non-destructive testing and structural health monitoring.

General conclusion

General conclusion

1 Work done

This research has advanced the field of Eddy Current Testing (ECT) by integrating theoretical modeling, numerical simulation, experimental validation, and intelligent defect characterization into a unified and coherent framework. At its foundation, the work reaffirmed the reasons why ECT maintains a central role among non-destructive testing (NDT) techniques. Its high sensitivity to surface and near-surface defects, rapid inspection capability, non-contact nature, and adaptability to different industrial contexts—particularly aerospace, oil and gas, power generation, and automotive—make it an indispensable method for safeguarding critical infrastructure. Although its inherent limitations, such as restricted penetration depth and reliance on conductive materials, remain, this study has shown that these challenges can be mitigated through innovative sensor design, advanced modeling, and intelligent analysis.

From a methodological standpoint, the research combined analytical formulations with finite element modeling to construct a strong theoretical and numerical foundation. The use of harmonic excitation modes, coupled with multiplexed sensor configurations, enabled a detailed exploration of eddy current induction, defect perturbation, and impedance variation. The finite element method (FEM), based on the A–V formulation, proved to be highly effective in capturing realistic inspection conditions and predicting impedance signals with strong fidelity. In particular, the harmonic multiplexed strategy emerged as an optimal solution due to its simplicity, adaptability, and ability to provide high-resolution imaging of defects without excessive computational overhead.

2 Analysis of results and discussions

Validation against experimental measurements on aluminum, austenitic stainless steel, and titanium laminates demonstrated strong correlation, thereby confirming the robustness of the proposed models. This alignment between simulation and experiment not only validated the theoretical framework but also reinforced the practical applicability of multiplexed ECT systems for real-world inspection. Extending this foundation, advanced simulations revealed the capability of multiplexed sensor arrays to generate accurate 2D and 3D images of defects, including irregular geometries and complex tubular flaws, thereby demonstrating ECT's versatility for imaging randomly shaped and unpredictable defect structures.

A major contribution of this research lies in coupling ECT imaging with artificial intelligence, specifically the ***Radial Basis Function (RBF) neural network****. By training the RBF network on complex impedance responses, the system demonstrated the ability to predict defect dimensions and reconstruct defect geometries with notable efficiency. The strength of the RBF approach lies in its* ***simplicity, fast convergence, and ability to generalize well even with irregular and random defect patterns****. Unlike more computationally demanding deep learning architectures, the RBF neural network achieved a favorable balance between accuracy and computational* *cost, making it especially well-suited for near real-time defect detection in industrial contexts. This highlights its unique role as a lightweight yet powerful tool for intelligent ECT.*

More importantly, this study has shown that the ***combination of multiplexed ECT and RBF modeling significantly enhances the capacity to image random defects****, where defect geometries cannot be easily parameterized or predicted in advance. The synergy of these two techniques leverages the* ***high-resolution imaging capabilities of multiplexed ECT arrays*** *with the* ***robust predictive capability of RBF neural networks****, opening a promising pathway toward efficient, flexible, and intelligent inspection systems. This framework not only enables defect detection but also supports reliable imaging of irregular flaws, enhancing the overall interpretability of inspection results.*

3 Outlook

Looking forward, several perspectives for future research arise. First, further optimization of the ECT–RBF combination can be pursued by refining feature extraction from impedance signals and incorporating hybrid learning strategies to improve predictive accuracy for more complex defect geometries. Second, expanding the framework to deeper defect detection through advanced signal processing and enhanced excitation techniques will help overcome the traditional depth limitations of ECT. Finally, extending the integration of ECT with intelligent machine learning tools toward ***3D defect profiling and structural health monitoring systems*** *will pave the way for real-world deployment in safety-critical industries.*

In conclusion, this work not only strengthens the scientific understanding of eddy current phenomena but also introduces a validated, practical, and intelligent framework that combines ***multiplexed ECT imaging with RBF neural networks****. The results demonstrate a clear path forward: enhancing the synergy between non-destructive testing and machine learning to deliver efficient, accurate, and robust inspection methodologies capable of detecting and imaging even the most irregular and random defects.*

References:

[1] M. P. Georges, C. Thizy, F. Languy, and J.-F. Vandenrijt, "An overview of interferometric metrology and NDT techniques and applications for the aerospace industry," *https://doi.org/10.1117/12.2240676*, vol. 9960, pp. 40–51, Aug. 2016, doi: 10.1117/12.2240676.

[2] M. Gupta, M. A. Khan, R. Butola, and R. M. Singari, "Advances in applications of Non-Destructive Testing (NDT): A review," *Advances in Materials and Processing Technologies*, vol. 8, no. 2, pp. 2286–2307, Apr. 2022, doi: 10.1080/2374068X.2021.1909332.

[3] M. E. Bajgholi, G. Rousseau, M. Viens, D. Thibault, and M. Gagnon, "Reliability assessment of non-destructive testing (NDT) for the inspection of weld joints in the hydroelectric turbine industry," *International Journal of Advanced Manufacturing Technology*, vol. 128, no. 9–10, pp. 4223–4233, Oct. 2023, doi: 10.1007/S00170-023-12176-5/Metrics.

[4] V. Gagliardi *et al.*, "Satellite Remote Sensing and Non-Destructive Testing Methods for Transport Infrastructure Monitoring: Advances, Challenges and Perspectives," *Remote Sensing 2023, Vol. 15, Page 418*, vol. 15, no. 2, p. 418, Jan. 2023, doi: 10.3390/RS15020418.

[5] M. Shaloo, M. Schnall, T. Klein, N. Huber, and B. Reitinger, "A Review of Non-Destructive Testing (NDT) Techniques for Defect Detection: Application to Fusion Welding and Future Wire Arc Additive Manufacturing Processes," *Materials 2022, Vol. 15, Page 3697*, vol. 15, no. 10, p. 3697, May 2022, doi: 10.3390/MA15103697.

[6] M. A. Machado, "Eddy Currents Probe Design for NDT Applications: A Review," *Sensors (Basel)*, vol. 24, no. 17, p. 5819, Sep. 2024, doi: 10.3390/S24175819.

[7] M. H. Lutfallah, A. Y. Hammali, T. O. Felemban, and M. A. Alismail, "Digital Generation of Eddy Current Testing (ECT) for Inspection of Surface and Near-Surface Defects," pp. 1–9, Nov. 2023, doi: 10.5006/MECC2023-20114.

[8] P. Xu, Y. Chen, L. Liu, and B. Liu, "Study on high-speed rail defect detection methods based on ECT, MFL testing and ACFM," *Measurement*, vol. 206, p. 112213, Jan. 2023, doi: 10.1016/J. Measurement.2022.112213.

[9] L. U. Daura, "Investigation of wireless power transfer-based eddy current non-destructive testing and evaluation," 2022, Accessed: Sep. 16, 2025. doi:10443/5641

[10] D. Pasadas, T. Rocha, H. Ramos, and A. L. Ribeiro, "Portable eddy current NDT instrument using two different implementations," *EUROCON 2011 - International Conference on Computer as a Tool - Joint with Conftele 2011*, 2011, doi: 10.1109

[11] D. Rifai, A. N. Abdalla, R. Razali, K. Ali, and M. A. Faraj, "An Eddy Current Testing Platform System for Pipe Defect Inspection Based on an Optimized Eddy Current Technique Probe Design," *Sensors 2017, Vol. 17, Page 579*, vol. 17, no. 3, p. 579, Mar. 2017, doi: 10.3390/S17030579.

[12] A. N. AbdAlla, M. A. Faraj, F. Samsuri, D. Rifai, K. Ali, and Y. Al-Douri, "Challenges in improving the performance of eddy current testing: Review," *Measurement and Control*, vol. 52, no. 1–2, pp. 46–64, Jan. 2019, doi: 10.1177/0020294018801382.

[13] A. Sophian, G. Tian, and M. Fan, “Pulsed Eddy Current Non-destructive Testing and Evaluation: A Review,” *Chinese Journal of Mechanical Engineering (English Edition)*, vol. 30, no. 3, pp. 500–514, May 2017, doi: 10.1007/S10033-017-0122-4/FIGURES/9.

[14] N. Bowler, “Eddy-Current Nondestructive Evaluation,” *Springer Series in Measurement Science and Technology*, 2019, doi: 10.1007/978-1-4939-9629-2.

[15] Y. Yu, Y. Zou, M. Al Hosani, and G. Tian, “Conductivity invariance phenomenon of eddy current NDT: Investigation, verification, and application,” *IEEE Trans Magn*, vol. 53, no. 1, Jan. 2017, doi: 10.1109/TMAG.2016.2616328.

[16] Z. Jin *et al.*, “Methods of Controlling Lift-Off in Conductivity Invariance Phenomenon for Eddy Current Testing,” *IEEE Access*, vol. 8, pp. 122413–122421, 2020, doi: 10.1109/Access.2020.3007216.

[17] S. Liu, Y. Sun, M. Gu, C. Liu, L. He, and Y. Kang, “Review and analysis of three representative electromagnetic NDT methods,” *Insight: Non-Destructive Testing and Condition Monitoring*, vol. 59, no. 4, pp. 176–183, Apr. 2017, doi: 10.1784/INSI.2017.59.4.176.

[18] D. Lau and Q. Qiu, “A Review Of Nondestructive Testing Approaches Using Mechanical And Electromagnetic Waves,” *Nondestructive Characterization and Monitoring of Advanced Materials*, vol. 9804, pp. 404–415, Apr. 2016, doi: 10.1117/12.2218739.

[19] A. Katunin, A. Kroworz, and A. Katunin, “Non-Destructive Testing of Structures Using Optical and Other Methods: A Review,” *SDHM Structural Durability and Health Monitoring* , vol. 12, no. 1, pp. 1–17, 2018, doi: 10.3970/sdhm.2018.012.001.

[20] Q. Wu, K. Dong, X. Qin, Z. Hu, and X. Xiong, “Magnetic particle inspection: Status, advances, and challenges — Demands for automatic non-destructive testing,” *NDT and E International*, vol. 143, Apr. 2024, doi: 10.1016/J. Ndteint.2023.103030.

[21] J. Baumeyer, H. Chatoux, A. Pelletier, and P. Marquié, “Industrial Application of AI-Based Assistive Magnetic Particle Inspection,” *Applied Sciences 2024, Vol. 14, Page 1499*, vol. 14, no. 4, p. 1499, Feb. 2024, doi: 10.3390/APP14041499.

[22] H. Wang, W. Du, G. Xu, Y. Sun, and H. Shen, “Automated crack detection of train rivets using fluorescent magnetic particle inspection and instance segmentation,” *Scientific Reports* |, vol. 14, p. 10666, 123AD, doi: 10.1038/s41598-024-61396-6.

[23] L. Xiang, S. Dixon, C. B. Thring, Z. Li, and R. S. Edwards, “Lift-Off Performance of Electromagnetic Acoustic Transducers (Emats) for Surface Acoustic Wave Generation,” *NDT & E International,* Volume 126, *March* 2021, doi 161405 http://wrap.warwick.ac.uk/

[24] S. Wang, F. Gan, H. Gou, and Y. Du, “An Online Monitoring Method for High- Temperature Environments Combining Eddy Current Testing and Electromagnetic Acoustic Transducer Techniques,” *IEEE Sens J*, vol. 24, no. 6, pp. 8682–8693, Mar. 2024, doi: 10.1109/JSEN.2024.3355689.

[25] L. Yin, Y. X. Wu, and Y. T. Wu, “Enhancement of Rayleigh Wave Generated by Electromagnetic Acoustic Transducer Based on New Magnetic Configuration,” *Russian Journal of Nondestructive Testing*, vol. 59, no. 4, pp. 437–446, Apr. 2023, doi: 10.1134/S1061830923600028/Metrics.

[26] J. M. Ha, H. M. Seung, and W. Choi, “Autoencoder-based detection of near-surface defects in ultrasonic testing,” *Ultrasonics*, vol. 119, p. 106637, Feb. 2022, doi: 10.1016/ J. Ultras.2021.106637.

[27] A. Wronkowicz, K. Dragan, and K. Lis, “Assessment of Uncertainty in Damage Evaluation by Ultrasonic Testing of Composite Structures,” *Composite Structures*, Vol. 203, P 71-84, Nov 2018, doi.org/10.1016/j.compstruct.2018.06.109

[28] S. Lu *et al.*, “Finite Element Analysis and Experimental Investigation of Ultrasonic Testing of Internal Defects in Sicp/Al Composites,” *Ceram Int*, vol. 48, no. 5, pp. 5972–5982, Mar. 2022, doi: 10.1016/J. Ceramint.2021.11.133.

[29] S. C. Olisa, M. A. Khan, and A. Starr, “Review of Current Guided Wave Ultrasonic Testing (GWUT) Limitations and Future Directions,” *Sensors 2021, Vol. 21, Page 811*, vol. 21, no. 3, p. 811, Jan. 2021, doi: 10.3390/S21030811.

[30] I. Stüwe, L. Zacherl, and C. U. Grosse, “Ultrasonic and Impact-Echo Testing for the Detection of Scaling in Geothermal Pipelines,” *J Nondestr Eval*, vol. 42, no. 1, pp. 1–12, Mar. 2023, doi: 10.1007/S10921-023-00926-0/Figures/13.

[31] N. Eshetu Deresse, M. Sarem, H. Nasser, S. François, and E. Verstrynge, “Fatigue fracture quantification in brittle cementitious materials using acoustic emission testing and digital image correlation,” *Constr Build Mater*, vol. 400, p. 132635, Oct. 2023, doi: 10.1016/ J. Conbuildmat.2023.132635.

[32] G. Galanopoulos, D. Milanoski, A. Broer, D. Zarouchas, and T. Loutas, “Health Monitoring of Aerospace Structures Utilizing Novel Health Indicators Extracted from Complex Strain and Acoustic Emission Data,” *Sensors 2021, Vol. 21, Page 5701*, vol. 21, no. 17, p. 5701, Aug. 2021, doi: 10.3390/S21175701.

[33] T. Schumacher, B. Schechinger, and T. Vogel, “AE Monitoring of Real Structures: Applications, Strengths, and Limitations,” *Springer Tracts in Civil Engineering*, pp. 731–752, 2022, doi: 10.1007/978-3-030-67936-1_24.

[34] G. Ciaburro and G. Iannace, “Machine-Learning-Based Methods for Acoustic Emission Testing: A Review,” *Applied Sciences 2022, Vol. 12, Page 10476*, vol. 12, no. 20, p. 10476, Oct. 2022, doi: 10.3390/APP122010476.

[35] E. Verstrynge, C. Van Steen, E. Vandecruys, and M. Wevers, “Steel corrosion damage monitoring in reinforced concrete structures with the acoustic emission technique: A review,” *Constr Build Mater*, vol. 349, p. 128732, Sep. 2022, doi: 10.1016/J. Conbuildmat.2022.128732.

[36] W. G. Bley, “Methods of Leak Detection,” *Handbook of Vacuum Technology*, pp. 907–942, Jun. 2016, doi: 10.1002/9783527688265.CH19.

[37] S. R. Suffield, D. E. Carpenter-Graffy, and B. E. Wells, “Helium Leak Test Modeling of a Spent Nuclear Fuel Canister,” *American Society of Mechanical Engineers, Pressure Vessels and Piping Division (Publication) PVP*, vol. 5, Nov. 2024, doi: 10.1115/PVP2024-125017.

[38] H. Yu, X. Li, H. Xie, X. Li, and C. Hou, “Improving the industrial defect recognition in radiographic testing by pre-training on medical radiographs,” *NDT & E International*, vol. 149, p. 103260, Jan. 2025, doi: 10.1016/J. Ndteint.2024.103260.

[39] D. Dong, G. Yanhui, W. Yan, and Z. Yue, “Analysing suspected linear indications in narrow-gap welding of nuclear power plants via radiographic inspection,” *Nondestructive Testing and Evaluation*, Jan. 2024, doi: 10.1080/10589759.2024.2320748.

[40] H. Yu, X. Li, H. Xie, X. Li, and C. Hou, “Improving the industrial defect recognition in radiographic testing by pre-training on medical radiographs,” *NDT & E International*, vol. 149, p. 103260, Jan. 2025, doi: 10.1016/J.NDTEINT.2024.103260.

[41] R. Patel, D. Patel, and D. Meshram, "A Review on Non-Destructive Testing (NDT) Techniques: Advances, Research and Applicability," *International Journal of Current Science Research and Review*, Vol. 05, April 2022, doi: 10.47191/ijcsrr/V5-i4-59.

[42] K. R. Manikandan, P. Ashwin Sivagurunathan, S. S. Ananthan, A. Arul Marcel Moshi, and S. R. Sundara Bharathi, "Study on the influence of temperature and vibration on indications of liquid penetrant testing of A516 low carbon steel," *Mater Today Proc*, vol. 39, pp. 1559–1564, Jan. 2021, doi: 10.1016/J.MATPR.2020.05.572.

[43] A.Kumar, A.Kumar, and M.P Babu, "Experimental Study of Defects in Stainless Steel 316l Weldments Through Liquid Penetrant Test For Surface," *International Journal of Advanced Research in Engineering and Technology (IJARET)*, Vol. 12, April 2021, pp. 492-499 doi: 10.34218/IJARET.12.4.2021.047.

[44] N. P. Migoun and N. V. Delenkovskii, "Improvement of penetrant-testing methods," *Journal of Engineering Physics and Thermophysics*, vol. 82, no. 4, pp. 734–742, Jul. 2009, doi: 10.1007/S10891-009-0253-2/Metrics.

[45] M. Blankschän, D. Kanzler, and R. Liebich, "Visual testing: the influence of selected human factors on probability of detection," *Insight: Non-Destructive Testing and Condition Monitoring*, vol. 65, no. 1, pp. 13–18, Jan. 2023, doi: 10.1784/INSI.2023.65.1.13.

[46] F. W. Panella, A. Pirinu, and V. Dattoma, "A Brief Review and Advances of Thermographic Image - Processing Methods for IRT Inspection: a Case of Study on GFRP Plate," *Exp Tech*, vol. 45, no. 4, pp. 429–443, Aug. 2021, doi: 10.1007/S40799-020-00414-4/TABLES/4.

[47] M. ; Y. L. A. Chew *et al.*, "A Review of Infrared Thermography for Delamination Detection on Infrastructures and Buildings," *Sensors 2022, Vol. 22, Page 423*, vol. 22, no. 2, p. 423, Jan. 2022, doi: 10.3390/S22020423.

[48] S. Zhong and W. Nsengiyumva, "Infrared Thermography Testing and Evaluation of Fiber-Reinforced Composite Materials," *Nondestructive Testing and Evaluation of Fiber-Reinforced Composite Structures*, pp. 197–271, 2022, doi: 10.1007/978-981-19-0848-4_5.

[49] A. Bahrami, M. K. Khouzani, S. A. Mokhtari, S. Zareh, and M. Y. Mehr, "Root Cause Analysis of Surface Cracks in Heavy Steel Plates during the Hot Rolling Process," *Metals 2019, Vol. 9, Page 801*, vol. 9, no. 7, p. 801, Jul. 2019, doi: 10.3390/MET9070801.

[50] K. H. Jeong, D. H. Lee, S. H. Lee, S. J. Lim, and H. K. Moon, "Identifying Quality Factors for Surface Defects on Small Steel Bars Using a Two-step Method of Statistical Difference Testing and k-means Clustering," *International Journal of Precision Engineering and Manufacturing*, vol. 25, no. 3, pp. 597–609, Mar. 2024, doi: 10.1007/S12541-023-00941-1/Metrics.

[51] D. Siwiec, A. Pacana, and A. Pacana , "ANALYSIS OF THE CAUSES OF POROSITY IDENTIFIED BY NON-DESTRUCTIVE TESTING," *Zarządzanie Przedsiębiorstwem. Enterprise Management*, vol. 23, no. 2, pp. 25–28, 2020, doi: 10.25961/ent.manag.23.02.04.

[52] P. Amirafshari, N. Barltrop, M. Wright, and A. Kolios, "Weld defect frequency, size statistics and probabilistic models for ship structures," *Int J Fatigue*, vol. 145, p. 106069, Apr. 2021, doi: 10.1016/J.IJFATIGUE.2020.106069.

[53] A. Wilczek, P. Długosz, and M. Hebda, "Porosity Characterization of Aluminium Castings by Using Particular Non-destructive Techniques," *J Nondestr Eval*, vol. 34, no. 3, pp. 1–7, Aug. 2015, doi: 10.1007/S10921-015-0302-Z/FIGURES/5.

[54] X. ; Bai *et al.*, "Identification of Subsurface Mesoscale Crack in Full Ceramic Ball Bearings Based on Strain Energy Theory," *Applied Sciences 2023, Vol. 13, Page 7783*, vol. 13, no. 13, p. 7783, Jun. 2023, doi: 10.3390/APP13137783.

[55] J. F. Yin, Q. Bai, and B. Zhang, "Methods for detection of subsurface damage: A review," *Chinese Journal of Mechanical Engineering (English Edition)*, vol. 31, no. 3, pp. 1–14, Jun. 2018, doi: 10.1186/S10033-018-0229-2/TABLES/2.

[56] P. Jakubczak and J. Bienias, "Non-destructive Damage Detection in Fibre Metal Laminates," *J Nondestr Eval*, vol. 38, no. 2, Jun. 2019, doi: 10.1007/S10921-019-0588-3.

[57] D. Zhukov, S. Konovalov, A. Melnikov, and D. Chen, "Evaluation of strength and microstructure of welded pipes with wall lamination," *Eng Fail Anal*, vol. 122, p. 105235, Apr. 2021, doi: 10.1016/J.ENGFAILANAL.2021.105235.

[58] S. Garg and S. Misra, "Efficiency of NDT techniques to detect voids in grouted post-tensioned concrete ducts," *Nondestructive Testing and Evaluation*, vol. 36, no. 4, pp. 366–387, Jul. 2021, doi: 10.1080/10589759.2020.1758100.

[59] Y. Hou, T. Pojtanabuntoeng, M. Salasi, M. Iannuzzi, and J. McKechnie, "Assessing the efficacy of non-destructive testing methods to detect pitting corrosion," *Nondestructive Testing and Evaluation*, vol. 38, no. 3, pp. 373–393, May 2023, doi: 10.1080/10589759.2022.2137163.

[60] Y. Hou, T. Pojtanabuntoeng, M. Salasi, M. Iannuzzi, and J. McKechnie, "Assessing the efficacy of non-destructive testing methods to detect pitting corrosion," *Nondestructive Testing and Evaluation*, vol. 38, no. 3, pp. 373–393, May 2023, doi: 10.1080/10589759.2022.2137163.

[61] C. Dong, S. Qu, C. Ming Fu, and Z. Feng Zhang, "Failure analysis of crevice corrosion on 304 stainless steel tube heat exchanger," *Journal of Iron and Steel Research International*, vol. 30, no. 8, pp. 1490–1498, Aug. 2023, doi: 10.1007/S42243-023-01001-8/METRICS.

[62] S. Yonezawa, A. Yerokhin, M. Vakili, P. Koutník, J. Kohout, and Z. Gholami, "Analysis, Assessment, and Mitigation of Stress Corrosion Cracking in Austenitic Stainless Steels in the Oil and Gas Sector: A Review," *Surfaces 2024, Vol. 7, Pages 589-642*, vol. 7, no. 3, pp. 589–642, Aug. 2024, doi: 10.3390/SURFACES7030040.

[63] W. Kuang, M. Song, and G. S. Was, "Insights into the stress corrosion cracking of solution annealed alloy 690 in simulated pressurized water reactor primary water under dynamic straining," *Acta Mater*, vol. 151, pp. 321–333, Jun. 2018, doi: 10.1016/J.Actamat.2018.04.002.

[64] R. Beutel *et al.*, "Comparative performance tests and validation of NDT methods for concrete testing," *J Nondestr Eval*, vol. 27, no. 1–3, pp. 59–65, Jun. 2008, doi: 10.1007/S10921-008-0037-1/Metrics.

[65] A. Lopes Ribeiro, H. G. Ramos, and J. Couto Arez, "Liftoff insensitive thickness measurement of aluminum plates using harmonic eddy current excitation and a GMR sensor," in *Measurement: Journal of the International Measurement Confederation*, Nov. 2012, pp. 2246–2253. doi: 10.1016/j.measurement.2012.04.025.

[66] D. Hachi, N. Benhadda, B. Helifa, I. K. Lefkaier, and B. Abdelhadi, "Composite material characterization using Eddy current by 3D FEM associated with iterative technique," *Advanced Electromagnetics*, vol. 8, no. 1, pp. 8–15, 2019, doi: 10.7716/aem.v8i1.953.

[67] A. Bossavit and J.-C. Grit6, "A Mixed Fem-Biem Method To Solve 3-D Eddy-Current Problems," *IEEE Transactions on Magnetics*, Mach 1982, Vol. 18, pp. 431 – 435, doi: 10.1109/TMAG.1982.1061847.

[68] A. Lopes Ribeiro, H. G. Ramos, and J. Couto Arez, “Liftoff insensitive thickness measurement of aluminum plates using harmonic eddy current excitation and a GMR sensor,” in *Measurement: Journal of the International Measurement Confederation*, Nov. 2012, pp. 2246–2253. doi: 10.1016/j.measurement.2012.04.025.

[69] S. Xie *et al.*, “Features extraction and discussion in a novel frequency-band-selecting pulsed eddy current testing method for the detection of a certain depth range of defects,” *NDT and E International*, vol. 111, Apr. 2020, doi: 10.1016/j.ndteint.2019.102211.

[70] B. A. Abu-Nabah and P. B. Nagy, “Lift-off effect in high-frequency eddy current conductivity spectroscopy,” *NDT & E International*, vol. 40, no. 8, pp. 555–565, Dec. 2007, doi: 10.1016/J.NDTEINT.2007.06.001.

[71] J. Kral, R. Smid, H. M. G. Ramos, and A. L. Ribeiro, “The lift-off effect in Eddy currents on thickness modeling and measurement,” *IEEE Trans Instrum Meas*, vol. 62, no. 7, pp. 2043–2049, 2013, doi: 10.1109/TIM.2013.2247713.

[72] Z. Mottl, “The quantitative relations between true and standard depth of penetration for air-cored probe coils in eddy current testing,” *NDT International,* vol. 34, pp. 11-18, February 1990, doi.org/10.1016/0308-9126(90)91444-X.

[73] M. Passarotto, R. Specogna, and C. Geuzaine, “Fast Iterative Schemes for the Solution of Eddy-Current Problems Featuring Multiple Conductors by Integral Formulations,” *IEEE Trans Magn*, vol. 56, no. 3, Mar. 2020, doi: 10.1109/TMAG.2019.2954071.

[74] G. Mook, O. Hesse, and V. Uchanin, “Deep penetrating eddy currents and probes,” *Materialpruefung/ Materials Testing*, vol. 49, no. 5, pp. 258–264, May 2007, doi: 10.3139/120.100810/Machinereadablecitation/Ris.

[75] W. Du, Q. Bai, Y. Wang, and B. Zhang, “Eddy current detection of subsurface defects for additive/subtractive hybrid manufacturing,” *International Journal of Advanced Manufacturing Technology*, vol. 95, no. 9–12, pp. 3185–3195, Apr. 2018, doi: 10.1007/S00170-017-1354-2/Metrics.

[76] B. Helifa, A. Oulhadj, A. Benbelghit, I. K. Lefkaier, F. Boubenider, and D. Boutassouna, “Detection and measurement of surface cracks in ferromagnetic materials using eddy current testing,” *NDT & E International*, vol. 39, no. 5, pp. 384–390, Jul. 2006, doi: 10.1016/J.Ndteint.2005.11.004.

[77] M. Zergoug, S. Lebaili, H. Boudjellal, and A. Benchaala, “Relation between mechanical microhardness and impedance variations in eddy current testing,” *NDT & E International*, vol. 37, no. 1, pp. 65–72, Jan. 2004, doi: 10.1016/J.NDTEINT.2003.09.002.

[78] G. Betta, L. Ferrigno, M. Laracca, P. Burrascano, M. Ricci, and G. Silipigni, “An experimental comparison of multi-frequency and chirp excitations for eddy current testing on thin defects,” *Measurement*, vol. 63, pp. 207–220, Mar. 2015, doi: 10.1016/J.Measurement.2014.12.015.

[79] T. J. Rocha, H. G. Ramos, A. L. Ribeiro, and D. J. Pasadas, “Evaluation of Subsurface Defects Using Diffusion of Motion-Induced Eddy Currents,” *IEEE Trans Instrum Meas*, vol. 65, no. 5, pp. 1182–1187, May 2016, doi: 10.1109/TIM.2015.2507738.

[80] C. H. Smith, R. W. Schneider, T. Dogaru, and S. T. Smith, “Eddy-Current Testing with GMR Magnetic Sensor Arrays,” *AIP Conf Proc*, vol. 700, no. 1, pp. 406–413, Feb. 2004, doi: 10.1063/1.1711651.

[81] N. Zhang, C. Ye, L. Peng, and Y. Tao, "Novel Array Eddy Current Sensor with Three-Phase Excitation," *IEEE Sens J*, vol. 19, no. 18, pp. 7896–7905, Sep. 2019, doi: 10.1109/JSEN.2019.2919661.

[82] T. Chen *et al.*, "Design and Performance Research of a New Dual-Excitation Uniform Eddy Current Probe," *Sensors 2022, Vol. 22, Page 8850*, vol. 22, no. 22, p. 8850, Nov. 2022, doi: 10.3390/S22228850.

[83] G. Betta, L. Ferrigno, M. Laracca, P. Burrascano, M. Ricci, and G. Silipigni, "An experimental comparison of multi-frequency and chirp excitations for eddy current testing on thin defects," *Measurement*, vol. 63, pp. 207–220, Mar. 2015, doi: 10.1016/J.MEASUREMENT.2014.12.015.

[84] M. Bodruzzaman and S. Zein-Sabatto, "Estimation of micro-crack lengths using eddy current c-scan images and neural-wavelet transform," *Conference Proceedings - IEEE SOUTHEASTCON*, pp. 551–556, 2008, doi: 10.1109/SECON.2008.4494355.

[85] A. Kyrgiazoglou and T. Theodoulidis, "Simulation of Eddy Current Non Destructive Testing using COMSOL® Multiphysics," *Conference: Comsol Multiphysics Conference Rotterdam, Oct* 2017

[86] A. Abderrahmane, A. Abdelhak, B. Bouchaala, A. Abdeslam, and K. Merwane, "Scanning by multi-sensors to detect surface and internal defects," in *Proceedings of the 2022 International Conference of Advanced Technology in Electronic and Electrical Engineering, ICATEEE 2022*, Institute of Electrical and Electronics Engineers Inc., 2022. doi: 10.1109/ICATEEE57445.2022.10093732.

[87] S. Bakhtiari and D. S. Kupperman, "Modeling of Eddy Current Probe Response For Steam Generator Tubes," *Nuclear Engineering and Design,* Vol. 194, Pages 57-71, November 1999, doi.org/10.1016/S0029-5493(99)00169-7

[88] X. Chen, J. Li, and Z. Wang, "Inversion Method in Pulsed Eddy Current Testing for Wall Thickness of Ferromagnetic Pipes," *IEEE Trans Instrum Meas*, vol. 69, no. 12, pp. 9766–9773, Dec. 2020, doi: 10.1109/TIM.2020.3005114.

[89] M. P. Arenas *et al.*, "Novel austenitic steel ageing classification method using eddy current testing and a support vector machine," *Measurement*, vol. 127, pp. 98–103, Oct. 2018, doi: 10.1016/J.Measurement.2018.05.101.

[90] W. Deng, J. Bao, and B. Ye, "Defect Image Recognition and Classification for Eddy Current Testing of Titanium Plate Based on Convolutional Neural Network," *Complexity*, vol. 2020, no. 1, p. 8868190, Jan. 2020, doi: 10.1155/2020/8868190.

[91] P. Zhu, Y. Cheng, P. Banerjee, A. Tamburrino, and Y. Deng, "A novel machine learning model for eddy current testing with uncertainty," *NDT & E International*, vol. 101, pp. 104–112, Jan. 2019, doi: 10.1016/J.NDTEINT.2018.09.010.

[92] C. L. Lin, J. F. Wang, C. Y. Chen, C. W. Chen, and C. W. Yen, "Improving the generalization performance of RBF neural networks using a linear regression technique," *Expert Syst Appl*, vol. 36, no. 10, pp. 12049–12053, Dec. 2009, doi: 10.1016/J.ESWA.2009.03.012.

[93] L. Xie, P. Baskaran, A. L. Ribeiro, F. C. Alegria, and H. G. Ramos, "Classification of Corrosion Severity in SPCC Steels Using Eddy Current Testing and Supervised Machine Learning Models," *Sensors 2024, Vol. 24, Page 2259*, vol. 24, no. 7, p. 2259, Apr. 2024, doi: 10.3390/S24072259.

[94] M. Le *et al.*, "Enhancing corrosion detection in pulsed eddy current testing systems through autoencoder-based unsupervised learning," *NDT & E International*, vol. 146, p. 103175, Sep. 2024, doi: 10.1016/J.NDTEINT.2024.103175.

[95] A. Abbassi, T. Bouchala, A. Abdou, and B. Abdelhadi, “Eddy Current Characterization of 3D Crack by Analyzing Probe Signal and Using a Fast Algorithm Search,” *Russian Journal of Nondestructive Testing*, vol. 56, no. 5, pp. 426–434, 2020, doi: 10.1134/S1061830920050022.

[96] X.Huang, Z. Li, L. Peng, Y. Chu, Z. Miles, S. K. Chakrapani, M. Han, A. Poudel, and Y. Deng, “A Novel Multi-Fidelity Gaussian Process Regression Approach for Defect Characterization in Motion-Induced Eddy Current Testing.” *NDT & E International,* Vol. 150, March 2025, 103274, doi.org/10.1016/j.ndteint.2024.103274

[97] M. Awad and R. Khanna, “Support Vector Regression,” *Efficient Learning Machines*, pp. 67–80, 2015, doi: 10.1007/978-1-4302-5990-9_4.

[98] D. Ribeiro dos Santos, “Development of a robust inversion methodology in nondestructive eddy current testing,” *Doctoral thesis from the University of Paris-Saclay*, p. 255, Mar. 2018, doi: 10.34894/VQ1DJA.

[99] M. È. Davoust, L. Le Brusquet, and G. Fleury, “Robust estimation of hidden corrosion parameters using an eddy current technique,” *J Nondestr Eval*, vol. 29, no. 3, pp. 155–167, Sep. 2010, doi: 10.1007/S10921-010-0073-5/METRICS.

[100] B. Cao, Z. Zhang, W. Yin, D. Wang, and Z. Zhang, “A Metal Classification System Based on Eddy Current Testing and Deep Learning,” *IEEE Sens J*, vol. 24, no. 3, pp. 3266–3276, Feb. 2024, doi: 10.1109/JSEN.2023.3340717.

[101] J. K. Sing, D. K. Basu, M. Nasipuri, and M. Kundu, “Improved k-means algorithm in the design of RBF neural networks,” *IEEE Region 10 Annual International Conference, Proceedings/TENCON*, vol. 3, pp. 841–845, 2003, doi: 10.1109/TENCON.2003.1273297.

[102] Y. Wu, H. Wang, B. Zhang, and K.-L. Du, “Using Radial Basis Function Networks for Function Approximation and Classification,” *ISRN Applied Mathematics*, vol. 2012, pp. 1–34, Mar. 2012, doi: 10.5402/2012/324194.

[103] H. Yu, T. Xie, S. Paszczyñski, and B. M. Wilamowski, “Advantages of radial basis function networks for dynamic system design,” in *IEEE Transactions on Industrial Electronics*, Dec. 2011, pp. 5438–5450. doi: 10.1109/TIE.2011.2164773.

[104] K. G. Sheela and S. N. Deepa, “Review on Methods to Fix Number of Hidden Neurons in Neural Networks,” *Math Probl Eng*, vol. 2013, no. 1, p. 425740, Jan. 2013, doi: 10.1155/2013/425740.

[105] W. Jia, D. Zhao, T. Shen, C. Su, C. Hu, and Y. Zhao, “A New Optimized GA-RBF Neural Network Algorithm,” *Comput Intell Neurosci*, vol. 2014, no. 1, p. 982045, Jan. 2014, doi: 10.1155/2014/982045.

[106] K.Artur, and P.Jordan,“The adaptation of the cross-validation approach for RBF-based collocation methods,” *Czasopismo Techniczne*, vol. 7, 2017, doi: 10.4467/2353737XCT.17.115.6656.

Publication and communications:

International publication

Abderrahmane ABOURA, Abdelhak ABDOU, Tarik BOUCHALA, Mohamed CHEBOUT, Bachir ABDELHADI, Marwen KHABEL , " Reconstruction of Defect Paths Using Eddy Current Testing Array 3D Imaging ", Acta Universitatis Sapientiae, Electrical and Mechanical Engineering, 2024, no. 16 pp 38-47.
https://acta.sapientia.ro/en/series/electrical-and-mechanical-engineering/publications-acta-emeng/volume-16-2024_/reconstruction-of-defect-paths-using-eddy-current-testing-array-3d-imaging ,
DOI: 10.47745/auseme-2024-0004

International communications:

- **Abderrahmane ABOURA, Abdelhak ABDOU, Tarik BOUCHALA, Abdeslam AOUKILI, Merwane KHEBAL**.. " Eddy Current Systeme With Multi-elements Sensors and Harmonic Mode for Detection of Surface Flaws in Sheet Metal ", the 2nd International Seminar on Industrial Engineering and Applied Mathematics (ISIEAM'22), on October 23-24, 2022 at the university of Skikda, Algeria. in Skikda (Algeria)

- **Abderrahmane ABOURA, Abdelhak ABDOU, Tarik BOUCHALA, Abdeslam AOUKILI, Merwane KHEBAL**. " Scanning by multi-sensors to detect surface and internal defects ", The 2022 International Conference of Advanced Technology in Electronic and Electrical Engineering (ICATEEE) on November 26-27, 2022 at the university of Msila, Algeria.